Tampereen yliopisto

Mika Kiviluoma

NON-DESTRUCTIVE TESTING OF ADDITIVELY MANUFACTURED STEEL COMPONENTS

Engineering and Natural Sciences
Master of Science theses
9/2019

ABSTRACT

Mika Kiviluoma: Non-destructive testing of additively manufactured steel components
Master of Sciences theses
Tampere University
Materials Science
9/2019

Additive manufacturing (AM) is a relatively new manufacturing method, which is capable of producing complex geometries and parts on-demand from multiple different materials. Metal AM, with all its advantages, has some challenges as well, many of which are related to residual stresses (RS) generated in the component during manufacturing.

In this work a literature study into the current state of the art of metal AM and especially laser powder bed fusion (L-PBF) is performed. Additionally L-PBF manufactured simple 316L steel components with different post process treatments are characterized both non-destructively and destructively and the results are compared to previous studies. Similarly, more complex 316L rapid mixing nozzles are characterized. The stress corrosion cracking (SCC) properties of AM 316L are also studied.

It is shown that x-ray diffraction (XRD) is a suitable non-destructive testing (NDT) method for characterizing the stress states of AM 316L components. Visual observations and RS depth profiles from the simple AM samples show RS states, which correspond to previous results. Microstructures of AM samples after different post process treatments are also as expected. Martensite transformation due to plastic deformation in AM samples is studied, but cannot be confirmed. No SCC is detected during testing.

An expected compressive RS state is found at the surfaces of the mixing nozzles. Below the surface of one of the nozzles, the stress state changes to anisotropic tension. Possible reasons for this are discussed. The microstructure of the nozzle is as expected. The behavior of the materials of the two sample sets are compared and discussed.

Keywords: non-destructive testing, NDT, additive manufacturing, AM, stainless steel, 316L, x-ray diffraction, XRD, stress corrosion cracking, SCC

TIIVISTELMÄ

Mika Kiviluoma: Non-destructive testing of additively manufactured steel components
Diplomityö
Tampereen yliopisto
Materiaalitekniikka
9/2019

Ainetta lisäävä valmistus on melko uusi valmistusmenetelmä, joka kykenee tuottamaan monimutkaisia geometrioita sekä osia juuri silloin kun niitä tarvitaan useista eri materiaaleista. Metallin ainetta lisäävässä valmistuksessa on lukuisia hyviä puolia perinteisiin valmistusmenetelmiin nähden, mutta siinä on myös paljon haasteita, joista suuri osa liittyy kappaleessa valmistuksen aikana syntyviin jäännösjännityksiin.

Tässä työssä tehdään kirjallisuusselvitys metallin ainetta lisäävän valmistuksen ja erityisesti jauhepetitekniikan nykytilasta. Lisäksi tehdään käytännön kokeita, joissa karakterisoidaan sekä ainetta rikkomattomasti, että rikkovasti yksinkertaisia, jauhepetitekniikalla valmistettuja ja eri jälkikäsittelyille altistettuja 316L-teräskomponentteja. Tuloksia verrataan aiemmin tehtyihin tutkimuksiin. Lisäksi karakterisoidaan monimutkaisempia 316L-teräksisiä sekoitussuuttimia. Tässä työssä tutkitaan myös ainetta lisäävästi valmistetun 316L-teräksen jännityskorroosio-ominaisuuksia.

Röntgendiffraktio todetaan sopivaksi tutkimusmenetelmäksi 316L-teräksen jäännösjännitysten karakterisointiin. Visuaaliset havainnot ja jäännösjännitysprofiilit osoittavat näytteissä vallitsevan odotetun laisen jännitystilan. Näytteiden mikrorakenteet jälkikäsittelyjen jäljiltä ovat odotetun laiset. Martensiitin muodostumista ainetta lisäävästi valmistettuihin näytteisiin plastisen muodonmuutoksen seurauksena ei voida varmistaa. Jännityskorroosiota ei havaita.

Sekoitussuuttimien pinnoista löytyy odotetun lainen puristava jäännösjännitystila. Tutkittaessa jännitystilaa syvemmältä, yhdessä suuttimessa havaitaan anisotrooppinen vetojännitys. Mahdollisia syitä tällaiselle jännitystilalle pohditaan. Suuttimen mikrorakenne on odotetun lainen. Kahden näytesarjan, yksinkertaisten näytteiden sekä suuttimien materiaalien havaittuja ominaisuuksia verrataan toisiinsa.

Avainsanat: ainetta rikkomaton testaus, ainetta lisäävä valmistus, ruostumaton teräs, 316L, röntgen diffraktio, jännityskorroosio

PREFACE

Making a thesis for the university was both a blessing and a curse. On one hand, I had almost complete freedom on when and how to execute my research, which was a huge bonus and possibly quite a unique possibility, even within the university. On the other hand, as my research questions were academic in nature, i.e. there was not any actual problem to solve, I sometimes, especially when tackling challenges with the corrosion tests, had a hard time seeing the point of my work. Fortunately, I had all my studies completed before my thesis work, which allowed me to focus all my efforts on this single task. Overall, I am happy with how everything turned out.

I would like to thank some persons and parties that were instrumental and helpful in making of this thesis. First, I want to thank my supervisors, Professor Minnamari Vippola and especially research fellow Suvi Santa-aho, who was always quick to answer any questions I had. Second, I want to thank Outotec and 3D Formtech, for graciously providing me with samples to study. Third, I want to thank Mari Lindgren of Outotec for helpful discussions on all things related to my thesis, and Mikael Schönning of Outokumpu for valuable consultation on corrosion testing.

This work made use of Tampere Microscopy Centre facilities at Tampere University.

Tampere 17.9.2019

Mika Kiviluoma

CONTENTS

1. INTRODUCTION 1
2. ADDITIVE MANUFACTURING 3
2.1 Principles 3
2.1.1 Vat photopolymerization 4
2.1.2 Material jetting 4
2.1.3 Binder jetting 5
2.1.4 Powder bed fusion 6
2.1.5 Material extrusion 7
2.1.6 Directed energy deposition 8
2.1.7 Sheet lamination 9
2.1.8 Materials in additive manufacturing 10
2.2 Powder bed fusion 11
2.2.1 Process parameters in L-PBF 11
2.2.2 Microstructural and mechanical properties 16
2.3 State-of-the-art of powder bed fusion 19
2.3.1 Residual stress control 20
2.3.2 Residual stress measurement techniques 21
2.3.3 Tailored microstructures 23
2.3.4 Compositionally graded alloys 25
3. EXPERIMENTAL 27
3.1 Methods and materials of the strip sample studies 27
3.1.1 3D printing 27
3.1.2 Heat treatment 29
3.1.3 Shot peening 30
3.1.4 316L sheet 30
3.1.5 AM316L 31
3.1.6 Metallography 33
3.1.7 Corrosion testing 33
3.1.8 X-ray diffraction 40
3.1.9 Hardness measurements 42
3.2 Results 42
3.2.1 Surface XRD results 42
3.2.2 Residual stress depth profiles 49
3.2.3 Corrosion tests 52
3.2.4 Metallography 55
3.2.5 Hardness measurements 59
3.3 Rapid mixing nozzles 61
3.3.1 Methods and materials of the rapid mixing nozzle studies 61
3.3.2 Results 64
4. DISCUSSION 68
4.1 Surface XRD results 68
4.2 Residual stress depth profiles 71
4.3 Corrosion tests 74
4.4 Metallography and hardness measurements 78
4.5 Rapid mixing nozzles 81
5. CONCLUSION 85
REFERENCES 89

LIST OF FIGURES

Figure 1: Schematic representation of vat photopolymerization [23] 4
Figure 2: Schematic representation of material jetting [23] 5
Figure 3: Schematic representation of binder jetting [23] 5
Figure 4: Schematic representation of powder bed fusion [23] 7
Figure 5: Schematic representation of material extrusion [23] 8
Figure 6: Schematic representation of directed energy deposition [23] 8
Figure 7: Schematic representation of sheet lamination [23] 9
Figure 8: Schematic of different scan strategies, the arrows represent the scan vectors [35] 13
Figure 9: Illustration of the staircase effect 14
Figure 10: Fine cellular microstructure in AM 316L [51] 17
Figure 11: EBSD maps of AM 316L with build direction a: vertical and b: perpendicular to the image [7] 18
Figure 12: Schematic of the generation of residual stresses [30] 20
Figure 13: The principle of the contour method [66] 22
Figure 14: EBSD images of AM 316L processed with a beam power of a: 400W and b: 1000W [70] 24
Figure 15: EBSD map of in IN718 piece with tailored microstructure [68] 25
Figure 16: Examples of different interfaces in FGMs [73] 25
Figure 17: Co-ordinate system and nomenclature used to refer to the samples 27
Figure 18: Two images illustrating the tear at the ends of the samples 28
Figure 19: As built sample (below) against a reference (above) showing visible bending upwards after removal from build plate 29
Figure 20: Reference samples before (left) and after shot peening 31
Figure 21: Additively manufactured 316L samples with different post process treatments 33
Figure 22: 3D model and an image of the 4-point bending rigs 34
Figure 23: The geometry of the 4PB rig 36
Figure 24: AM heat treated sample after initial 4PB test showing significant yielding 37
Figure 25: 4PB test samples with 2 mm strain gages attached 38
Figure 26: Cross sections of the first corrosion test samples 39
Figure 27: XRD measurement points on the samples' top sufaces 41
Figure 28 a) & b): Residual stresses on the surfaces of the as built samples 43
Figure 29 a) & b): Residual stresses on the surfaces of the as built and heat treated samples 44
Figure 30 a) & b): Residual stresses on the surfaces of the as built, heat treated and shot peened samples 45
Figure 31 a) & b): Residual stresses on the surfaces of the as built and shot peened samples 46
Figure 32 a) & b): Residual stresses on the surfaces of the shot peened reference samples 47
Figure 33: Residual stresses on the surfaces of the reference samples 48
Figure 34: Diffraction peaks obtained from different samples 48
Figure 35: RS profile measured from the surface of Ref weld 1A 49
Figure 36 a) & b): Residual stress depth profiles of the B-sides of two as built samples and one heat treated sample in 0 and 90 degree directions respectively 50
Figure 37: Residual stress depth profiles of the top surface of an as built condition sample 51
Figure 38: Residual stress depth profiles of two shot peened reference samples and one shot peened AM sample 51

Figure 39: 10x magnified optical micrograph of the as built material after the first corrosion test; the inset is at 100x magnification 53
Figure 40: 10x magnified optical micrograph of the welded sample, showing the edge of the weldment after the first corrosion test 53
Figure 41: 10x magnified optical micrograph of the as built and heat treated material after the first corrosion test 54
Figure 42: 10x magnified optical micrograph of the reference material after the first corrosion test; the inset is at 100x magnification..... 54
Figure 43: Optical micrograph of the as built sample in y-direction at 10x magnification, build direction is toward the top of the image..... 55
Figure 44: Optical micrograph of the as built sample in y-direction at 100x magnification, build direction is toward the top of the image..... 56
Figure 45: Optical micrograph of the heat-treated sample in x-direction at 10x magnification..... 56
Figure 46: Secondary electron image of the as built sample 57
Figure 47: Optical micrographs of reference material after being shot peened three times 57
Figure 48: Edge of a heat treated AM sample after being shot peened three times 58
Figure 49: Edge of an AM sample after being shot peened two times..... 58
Figure 50: SE images of the edge of reference material after being shot peened once..... 59
Figure 51: An example of the hardness measurement points on Ref SP 3 sample 59
Figure 52: Hardness depth profiles of the shot peened samples..... 60
Figure 53: Hardness depth profiles of two AM samples 60
Figure 54: One of the rapid mixing nozzles with the print direction annotated 62
Figure 55: One of the rapid mixing nozzles showing the two XRD-measurement points at the bottom and at the largest flange..... 63
Figure 56: Residual stress depth profile measurement points on nozzle 2 64
Figure 57: Examples of the diffraction peaks from different nozzles..... 65
Figure 58: Residual stress depth profiles from a flange of nozzle 2..... 65
Figure 59: Residual stress depth profiles from inside surfaces of nozzle 2..... 66
Figure 60: Micrograph of the cross section of the tube wall, showing the outside surface; main image at 10x, inset at 100x 66
Figure 61: Micrograph of the cross section of the tube wall, showing the inside surface; main image at 10x, inset at 100x 67
Figure 62: AsB HT and AsB samples showing the different cutting directions on their B-sides..... 69
Figure 63: Two different diffraction patterns presented as pixel values; top from Ref SP 1, bottom from Ref SP 3..... 70
Figure 64: Deformation twins in (a): L-PBF processed and strained 316L (b): annealed and strained 316L [51]..... 78
Figure 65: FWMH value depth profiles of selected shot peened samples 81
Figure 66: Examples of diffraction patterns from the surface of nozzle 2..... 83

ABBREVIATIONS AND MARKINGS

AM	Additive manufacturing
BCC	Body-centered cubic
CMM	Coordinate measuring machine
DED	Directed energy deposition
EBM	electron beam melting
EB-PBF	Electron beam powder bed fusion
FCC	Face-centered cubic
FWHM	Full width at half maximum
HIP	Hot isostatic pressing
LAGB	Low-angle grain boundary
L-PBF	Laser powder bed fusion
LSP	Laser shock peening
NDT	Non-destructive testing
PBF	Powder bed fusion
RS	Residual stress
SCC	Stress corrosion cracking
SE	Secondary electron
SEM	Scanning electron microscope
XRD	X-ray diffraction
4PB	4-point bending

1. INTRODUCTION

In the last 15 years additive manufacturing has matured from rapid prototyping [1] to an actual industrial manufacturing method capable of producing high-performance components from otherwise difficult to process materials [2].

Of the four additive manufacturing methods capable of processing metal, powder bed fusion (PBF) is the most accurate, capable of producing sub-millimeter features [3] into a multitude of polymer and metal materials [4]. PBF can produce components and geometries that other manufacturing methods, like casting or forging cannot. Another often-quoted reason for using additive manufacturing is the possibility to reduce the part count of components and reduce or completely eliminate the need for assembly. [5,6]

The layer-wise building and fast cooling rate of the material during PBF gives rise to some distinct properties, like oriented microstructure [7] and strong residual stresses, sometimes up to the yield strength of the material [8].

One of the metal materials available to PBF processing is 316L austenitic stainless steel [9]. In general, 316L is used where good corrosion resistance, especially after welding is required. 316L's low carbon content prevents carbide precipitation during heat input, giving it excellent welding characteristics. [10] However, 316L has been shown to be susceptible to chloride induced stress corrosion cracking (SCC) in the presence of tensile residual stresses [11,12].

Shot peening is known to induce compressive residual stresses (RS) on the surface of components, and it has also been shown to reduce or entirely inhibit SCC [13]. Another method of reducing the dangerous tensile residual stresses is stress relief annealing heat treatment [14].

In this work a literature study into additive manufacturing and especially laser powder bed fusion (L-PBF) will be performed. The current state-of-the-art of L-PBF will be discussed. On the practical side, a set of 316L samples, manufactured by 3D Formtech using L-PBF, and subjected to different post processing treatments will be studied using a variety of methods. The residual stresses from the surfaces of the samples and residual

stress depth profiles of selected samples will be measured using x-ray diffraction (XRD) and the microstructures of the samples will be studied. In addition, rapid mixing nozzles manufactured of the same material, using a similar technique, provided by Outotec will be studied and compared to the sample set.

The main purpose of this study is to open a new branch of studies within the materials characterization group at Tampere University, and to gain experience in the study of austenitic stainless steels and additively manufactured components.

2. ADDITIVE MANUFACTURING

2.1 Principles

Additive manufacturing (AM), or more colloquially, 3D printing, is a group of manufacturing methods where by prototypes, tools or ready-to-use components are manufactured by adding material to the work piece. The basis of an additively manufactured component is a 3D model, which is then printed layer by layer [1]. This contrasts most other manufacturing methods, for instance cutting, turning and drilling, where the components are created by removing material. AM is also fundamentally different from casting and molding, both of which can produce fully or nearly ready-to-use components, as no molds are needed for AM. Even though AM can in principle produce components to their final shape, in practice the components are typically post-processed to improve their density, surface quality or microstructure for instance [4].

Though AM is a versatile manufacturing method, it has its limitations as well. The design process of parts is quite free, as traditional design for manufacturing-aspects do not need to be considered. This freedom also makes it possible to perform topology optimization. However, as the challenges of conventional manufacturing disappear, a new set of challenges emerges. First of these is the need to design the parts for the specific AM process. For instance in powder bed fusion, overhanging features, like the upper surfaces of cavities tend to have poor surface quality [15], and often require a support structure that needs to be printed and subsequently removed [16]. Another example is the tendency of small isolated details to overheat during manufacturing, due to the lack of cooling from consolidated material [17].

It is also important to mention, it does not always make sense to redesign a component from conventional to additive manufacturing. Additive manufacturing is at its best, when production runs are relatively small, lead times cannot be long [18] or the component has complex [19] and especially internal geometries [20], which cannot be otherwise manufactured.

A practical limitation with AM is the size of the available manufacturing machines. For instance, with PBF, commercial solutions are currently limited to less than one meter in the longest dimension. For example the EOS M 400 is capable of building components

with maximum dimensions of 400 x 400 x 400 mm [21] and SLM Solutions' SLM 800 with maximum dimensions of 500 x 280 x 850 mm [22].

AM is currently divided into seven categories [23]: vat photopolymerization, material jetting, binder jetting, powder bed fusion, material extrusion, directed energy deposition and sheet lamination. A short overview of each process is given next.

2.1.1 Vat photopolymerization

In vat photopolymerization, a photoreactive liquid or paste feedstock is selectively cured by UV radiation from lasers or lamps. The feedstock can also contain different fillers. A schematic of the process is presented in figure 1.

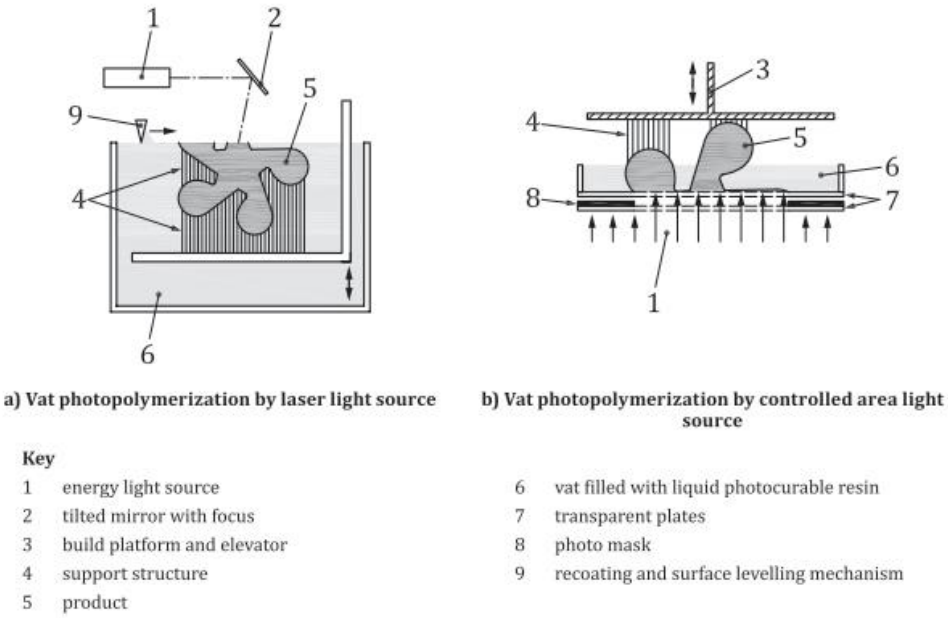

Figure 1: *Schematic representation of vat photopolymerization* [23]

Post-processing treatments of vat photopolymerized components include cleaning and further curing of the component by UV light. [23]

2.1.2 Material jetting

In material jetting, a photoreactive polymer or a molten wax is selectively deposited with support structures. The binding of the feedstock takes place by adhesion during solidification or through photopolymerization. The feedstock can also contain fillers. The process schematic is presented in figure 2.

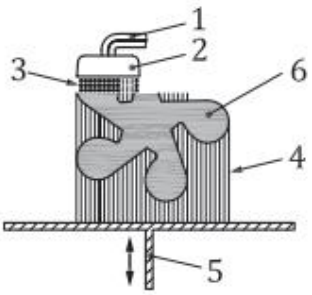

Key

1	feedstock delivery system for build and support material (optional dependent on the specific process)	4	support structure
2	dispensing apparatus (radiation light or thermal source)	5	build platform and elevator
3	droplets of build material	6	product

Figure 2: *Schematic representation of material jetting* [23]

Post processing treatments include cleaning and, in the case of photopolymers, further curing by UV light. [23]

2.1.3 Binder jetting

In binder jetting, a liquid binding agent is selectively deposited onto a layer of powder. After each binder deposition cycle a new layer of powder is spread across the old one and the binder depositing cycle is repeated. The process schematic is presented in figure 3.

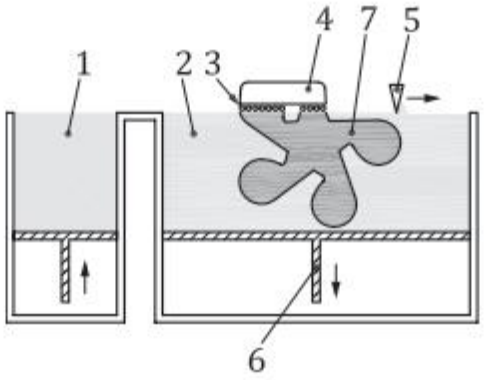

Key

1	powder feeding system	5	powder spreading device
2	powder material distributed in a powder bed	6	build platform and elevator
3	liquid bonding agent	7	product
4	dispensing apparatus including connection to bonding agent feed system		

Figure 3: *Schematic representation of binder jetting* [23]

Post processing includes removal of excess powder and impregnation of the component with liquid. [23]

2.1.4 Powder bed fusion

In powder bed fusion (PBF), a thin layer of powder is spread across a platform and is then selectively melted or sintered using laser (L-PBF) or electron beam (EB-PBF) as the heat source [23]. During L-PBF, the process chamber is filled with an inert gas, flowing across the powder bed, to increase cooling and eliminate spatter. EB-PBF requires a vacuum, so that the electron beam can reach the powder bed. However, the chamber can be back filled slightly with helium to increase cooling. [24]

L-PBF is currently more popular of the two PBF methods, with several companies manufacturing L-PBF systems (EOS, SLM Solutions, 3D Systems, Xact Metal), while only Arcam currently offers commercial EB-PBF systems. From the current commercial solutions, the EBM systems produced by Arcam are more directed at manufacturing special materials like TiAl intermetallic compound, that requires high preheat temperature. The EBM systems offered by Arcam are ostensibly also more expensive, as they make use of electron guns and vacuum systems, as well as being designed to withstand preheat temperatures of up to 1100 ºC. [25] More conventional materials, like 316L stainless steel currently offered by all of the previously mentioned L-PBF system manufacturers, do not necessarily require the high preheat temperatures, nor does the laser system require a vacuum to operate, making the systems simpler and cheaper. These factors make L-PBF systems currently more popular between the two options.

Suitable materials include thermoplastics, ceramics and metals and alloys. The use of fillers is also possible. A schematic of the process is presented in figure 4.

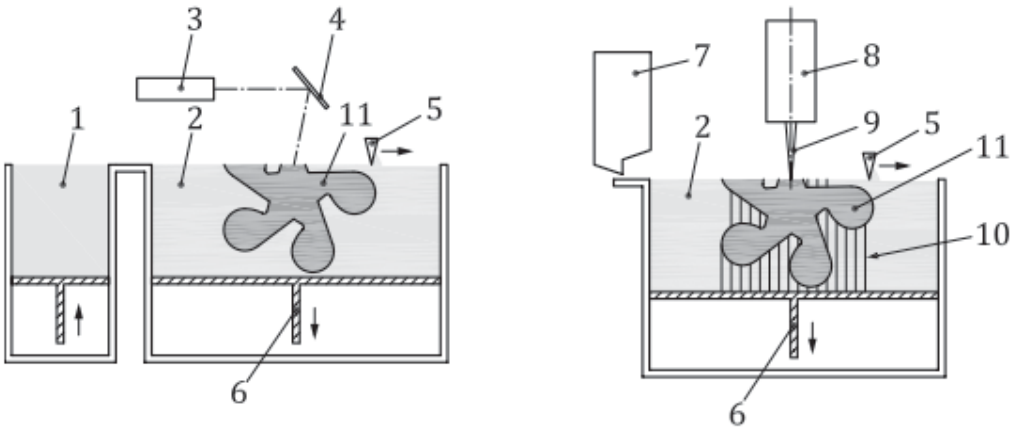

a) Laser based powder bed fusion **b) Electron beam powder bed fusion**

Key

1	powder feeding system (in some cases powder container like 7)	7	feedstock container
2	powder material distributed in a powder bed	8	electron beam gun
3	laser	9	focused electron beam
4	tilted mirror with focus	10	support structure
5	powder spreading device	11	product
6	build platform		

Figure 4: *Schematic representation of powder bed fusion* [23]

Post processing includes removal of excess powder and, especially with metal components, heat treatments, machining and sand blasting or shot peening. [23]

2.1.5 Material extrusion

In material extrusion, a molten of liquid feedstock is selectively deposited on previous layers of the component. Feedstock is typically a filament of thermoplastic, which can also contain fillers, like carbon or glass fiber reinforcements [26]. Process schematic is presented in figure 5.

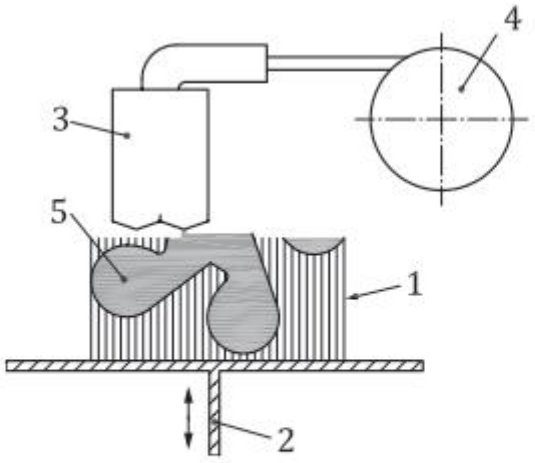

Key

1	support structure	4	feedstock supply
2	build platform and elevator	5	product
3	heated nozzle		

Figure 5: *Schematic representation of material extrusion* [23]

Post processing can be quite simple, as it typically includes only removal of support structures. [23]

2.1.6 Directed energy deposition

In directed energy deposition, a metallic powder or wire feedstock is deposited directly onto previous layers of the component, and molten using a laser or electron beam or a plasma transferred arc. The process schematic is presented in figure 6.

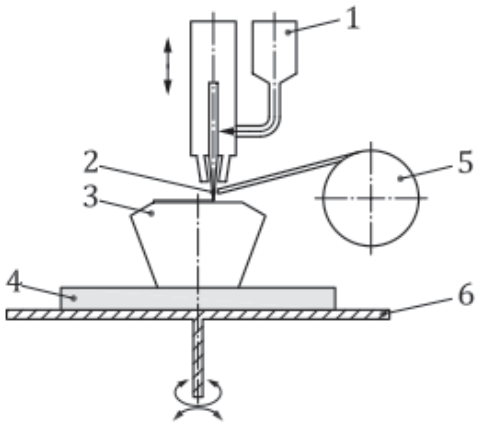

Key

1	powder hopper	4	substrate
2	directed energy beam, for example: laser, electron beam or plasma arc	5	wire (filament) coil
3	product	6	build table

Figure 6: *Schematic representation of directed energy deposition* [23]

Post processing is similar as with powder bed fusion, including operations to improve mechanical properties, surface finish and tolerances of the component, like heat treatments and machining. [23]

2.1.7 Sheet lamination

In sheet lamination, sheets of material are selectively bound together using selective heating, chemical reactions of binders or ultrasound. Used materials include paper, metal foils, polymers and composites. Process schematic is presented in figure 7.

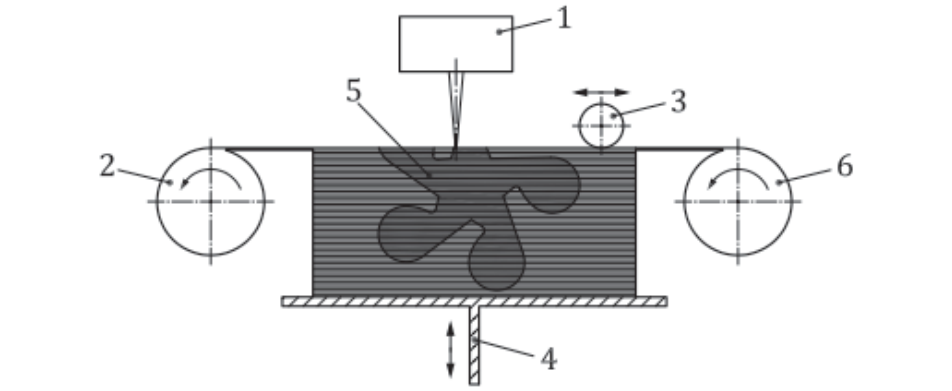

a) Sheet lamination of continuous roll

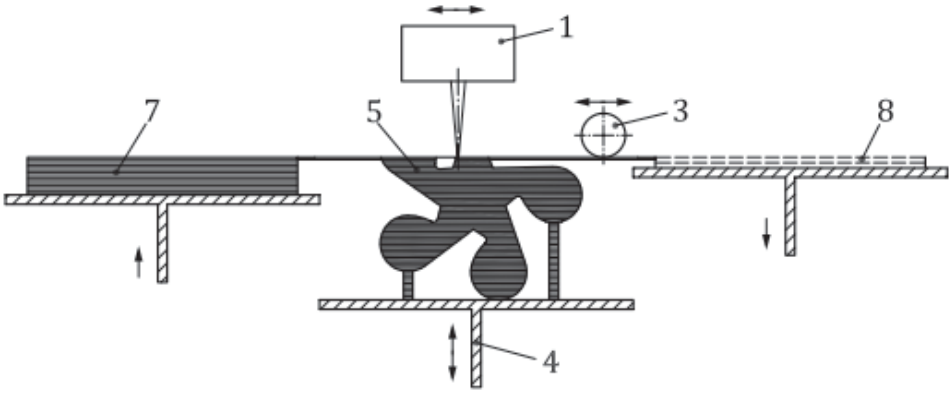

b) Sheet lamination of discontinuous sheets

Key

1	cutting device	5	product
2	excess material roll	6	raw material roll
3	laminator roll	7	excess material stack
4	build platform and elevator	8	raw material stack

Figure 7: *Schematic representation of sheet lamination* [23]

Post processing includes removal of excess material and possibly sintering, heat treatments and machining and sanding of the components. [23]

2.1.8 Materials in additive manufacturing

The unique nature of additive manufacturing sets special requirements for the feedstock materials. Not only does the material need to be in a form suitable for the process in question, like in powder form for PBF, but it also needs to have suitable properties, like good flow behaviour, homogeneity or suitable thermal properties.

Materials used for commercial AM applications are presented in table 1 [4].

Table 1: *Feedstock materials for different AM processes* [4]

	Amorphous	Semi-crystalline	Thermoset	Material extrusion	Vat polymerization	Material jetting	Powder bed fusion	Binder jetting	Sheet lamination	Directed energy deposition
ABS [Acryonitrile Butadiene Styrene]	X			X						
Polycarbonate	X			X						
PC/ABS Blend	X			X						
PLA [Polylactic Acid]	X			X						
Polyetherimide (PEI)]	X			X						
Acrylics			X		X	X				
Acrylates			X		X	X				
Epoxies			X		X	X				
Polyamide (Nylon) 11 and 12		X					X			
Neat		X					X			
Glass filled		X					X			
Carbon filled		X					X			
Metal (Al) filled		X					X			
Polymer bound	X	X		X						
Polystyrene	X						X			
Polypropylene		X					X			
Polyester ("Flex")							X			
Polyetheretherkeytone (PEEK)		X		X			X			
Thermoplastic polyurethane (Elastomer)				X			X			
Chocolate		X		X						
Paper									X	
Aluminum alloys							X	X	X	X
Co–Cr alloys							X	X		X
Gold							X			
Nickel alloys							X	X		X
Silver							X			
Stainless steel							X	X	X	X
Titanium, commercial purity							X	X	X	X
Ti–6Al–4V							X	X	X	X
Tool steel							X	X		X

The materials listed in Table 1 consist mostly of metal alloys, polymers and polymer composites, with two exceptions of paper and chocolate. In addition to these material classes, additive manufacturing of technical ceramics, like alumina and zirconia [27], metal matrix composites, like tungsten carbide/cobalt [4] and compositionally graded alloys [28] are also possible.

2.2 Powder bed fusion

Powder bed fusion, as presented previously, is an AM technique in which layers of powder are selectively sintered or fused to the previous layers using either a laser (L-PBF) or an electron beam (EB-PBF) as the heat source [23]. When compared to other AM methods capable of processing metal, sheet lamination, DED and binder jetting, PBF can achieve much higher accuracy, and does not require the additional sintering procedure that binder jetting does [3]. These features make it the go-to method for manufacturing complex metal components, and the subject of the current study.

The materials typically used for PBF consist of polymers, like polyamide, polypropylene and polyester, and metals, like steel, Ti64 and nickel alloys [4]. One prominent steel studied and used extensively is 316L austenitic stainless steel. It is weldable, corrosion resistant and can be shot peened and machined, making it ideal for additive manufacturing as well [9].

In this chapter the process parameters of L-PBF are introduced and microstructural and mechanical properties in laser powder bed fusion (L-PBF) manufacturing of metals are presented.

2.2.1 Process parameters in L-PBF

L-PBF process parameters consist of beam parameters [29], scan strategy [30], layer thickness [31], support structure parameters [8] and parameters concerning the printing environment, like atmosphere [3] and substrate and powder pre-heat [32]. These parameters are compiled into table 2

Table 2: *L-PBF process parameters, modified from* [3]

L-PBF
Beam power, W
Energy Density, J/mm^2
Beam focal offset, spot size
Hatch spacing (line offset), μm
Scan speed, m/s
Scan strategy
Powder, PSD, morphology
Powder layer thickness, μm
Powder moisture level
Deposit layer, Z step, μm
Build plate preheat, °C
Powder bed preheat, °C
Chamber gas, ppm O_2, H_2O

The beam energy density E in J/m-3 can be calculated from equation (1).

$$\boldsymbol{E = \frac{P}{v*h*t}}, \quad (1)$$

where P is the laser power in W, v is the scanning speed in m/s, h is the hatch spacing, or the distance between scan lines in m and t is the layer thickness in meters [33]. Thijs et al [33] found, that by decreasing the scanning velocity or hatch spacing, and thus increasing the energy density, the percentage of hard Ti_3Al precipitates in AM Ti64 was greater, resulting in harder overall material. The increased energy density meant that the material being processed was heated to higher temperatures and was kept in the Ti_3Al precipitation temperature for longer. Roehling et al [29] on the other hand found that by varying the energy density of the beam, the morphology of 316L stainless steel could be controlled, with lower densities producing equiaxed grains and higher densities columnar grains. Similar findings were also reported by Staroselsky et al [34], who found, that changing the scanning velocity changed the morphology of Inconel IN718. Besides the energy density, also the beam shape has an effect on morphology [29]. Roehling et al suggest in their study, that elliptical beam patterns could be used to rescan already deposited layers to improve the surface quality of the components [29].

The term scan strategy covers the movement of the laser beam on the powder bed. It determines the scan speed, how the beam moves on the layer being scanned (unidirectional, zigzag, chequerboard etc.) and the angle at which the current scan is oriented in relation to the previous layer, called the hatch angle. An example of different scan strategies is presented in Figure 8.

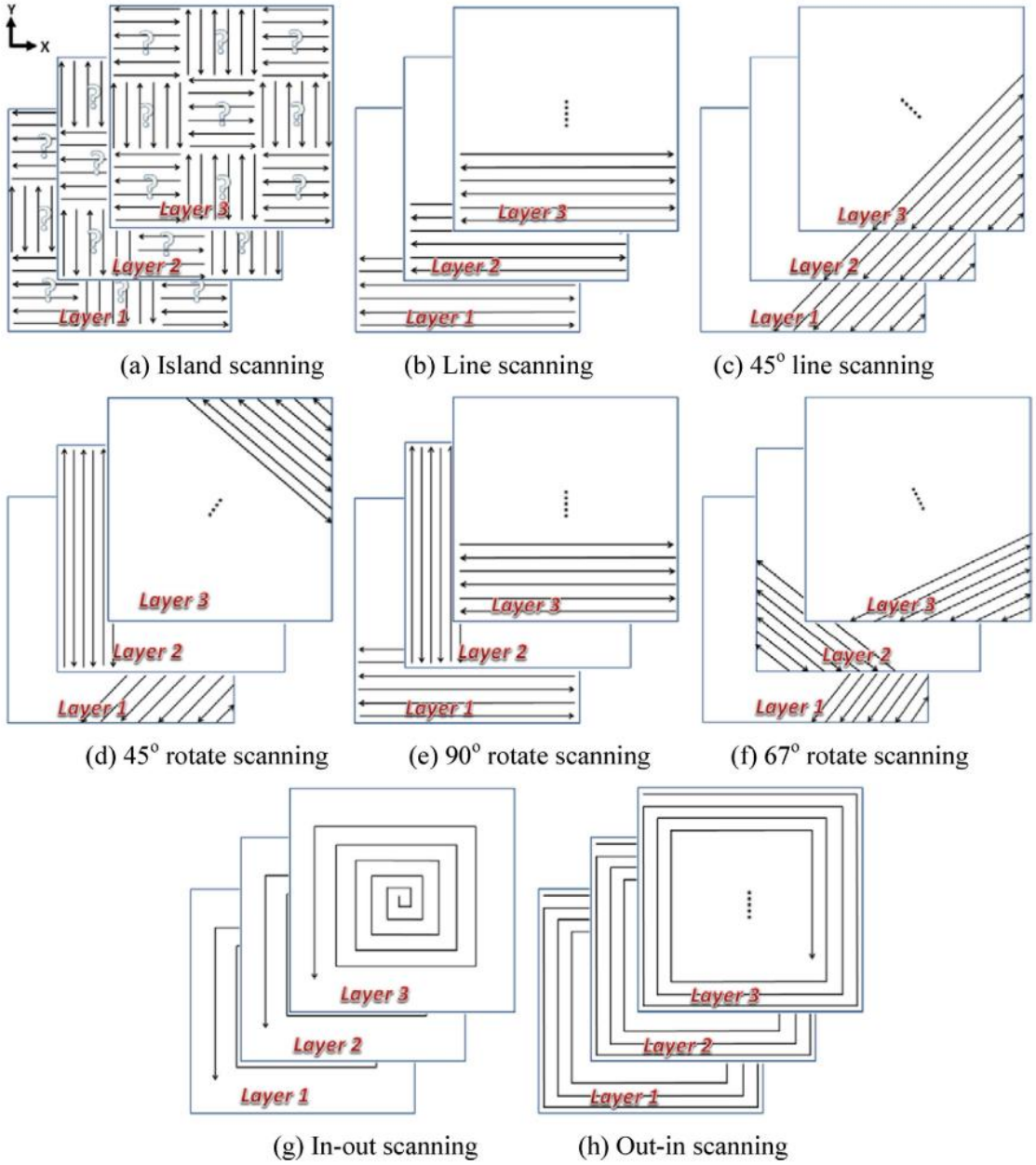

Figure 8: *Schematic of different scan strategies, the arrows represent the scan vectors* [35]

Scan strategy is an important parameter in controlling the residual stresses introduced into the component being built [30,35,36], but it also has an effect on the porosity of the components [37]. Robinson et al [30,36] studied the effects of different scan strategies on the residual stress generated in additively manufactured components, and concluded, that the greatest magnitude of residual stress is parallel to the scan vector. It was also

concluded, that the scan vector direction is the factor determining the direction of primary residual stress, rather than the vectors length. This finding was further used to determine, that by choosing the scan vector directions carefully, scan strategy could be used to direct the residual stresses into directions where it has the least effect on the component. Hatch angle rotation between scan layers on the other hand was found to be useful in creating a more uniformly distributed residual stress field. [30,36] Besides their findings regarding the effect of hatch angle rotation on residual stresses, Robinson et al [30] found, that angle rotation has no effect on part tensile strength nor its density. Another scan strategy factor, scanning speed on the other hand was found by Aboulkhair et al [37] to have an effect on part porosity. Too slow scanning speeds would create so called metallurgical pores, or trapped gas within the component, while too fast scanning speeds would lead to non-molten powder being trapped in between layers.

Typically deposited layer thicknesses vary between 0.08 and 0.15 millimeters [38]. The deposited layer thickness has an obvious effect on the resolution and surface quality of the components through the so called staircase effect [39], in which on a sloped surface being deposited layer by layer, each layer creates a step or a stair. This effect is illustrated in Figure 9

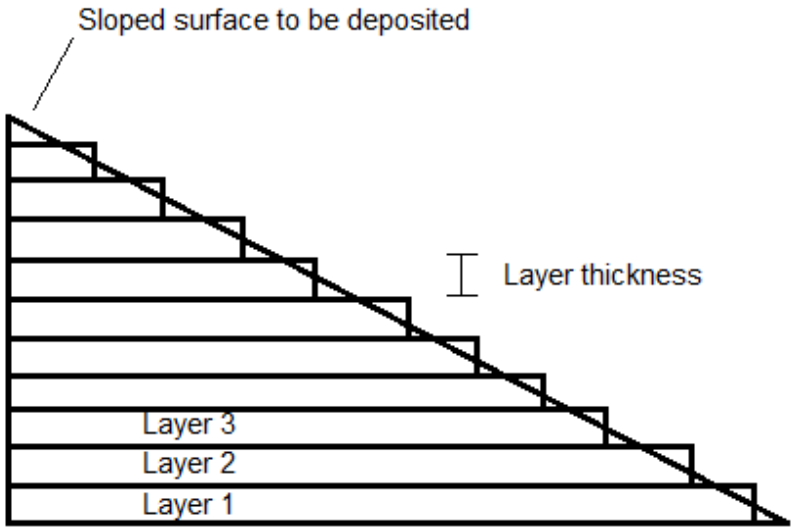

Figure 9: *Illustration of the staircase effect*

In addition to the effect on surface quality and resolution, Mukherjee et al [31] found in their simulations, that layer thickness has an effect on the magnitude of the residual stresses of the component. They concluded, that by decreasing the layer thickness, the

energy density, and therefore the heat input increases. This leads to the deposited material heating up to higher temperatures, allowing it to deform more easily, thus reducing the residual stress in the component.

The support structure incorporated to the additively manufactured parts in PBF has two main functions: to conduct heat away from the component and to hold the component in place during manufacturing, though the effect of these properties on the component being built is so far unclear. Brown et al [8] studied the effects of hatching and fragmentation of support structures on the residual stresses generated in Charpy test specimens built by PBF. They found the residual stress to be nearly invariant of the support structures. Similarly Hussein et al [16] reported using successfully support structures with as little as 8% volume fraction. It is worth noting, that neither of these studies details the scan strategy of the structure being supported, which is a significant factor when considering residual stresses, as discussed previously.

During PBF the process chamber, in the case of electron beam melting, is under vacuum, as the electron beam is easily attenuated by an atmosphere [24]. A very low pressure (less than 10^{-4} Torr) backfill of helium can be used to avoid electrical charging of the powder and to improve cooling [24]. In the case of L-PBF the chamber is purged of oxygen using and inert gas like argon [40] in order to avoid oxidation during processing. The shielding gas is also used to control and remove the gases and spatter generated by the laser recoil vapour pressure [41–43]. Ferrar et al [42] studied the effects of the gas flow over the powder bed and found, that the gas flow uniformity has an effect on part density, as a uniform flow is more efficient at protecting the powder bed from spatter.

Preheating the baseplate or the powder bed during the printing process has been found to reduce residual stresses [32,40] and to decrease the porosity of components [44]. Preheating reduces the cooling rate of the melt and decreases temperature gradients in the component. Typical preheating temperatures in L-PBF are between 200 ºC and 500 ºC [40].

Some process parameters and their effects on the component have been compiled to Table 3.

Table 3: *Process parameters and their effects on PBF*

Parameter	**Effect**	**Source**
Beam intensity	Microstructure morphology Precipitation in certain materials	[29,33,34]
Beam shape	Microstructure morphology Surface quality	[29]
Scan strategy (direction)	Residual stress direction	[30,35,36]
Scan strategy (speed)	Porosity	[37]
Layer thickness	Residual stress magnitude Resolution Surface quality	[31,39]
Support structure	Heat conduction Part deflection during manufacturing	[8,16]
Atmosphere and gas flow	Cooling Oxidation protection Porosity (through spatter removal)	[24,40–43]
Substrate and powder preheat	Residual stress magnitude Porosity	[24,40,44]

2.2.2 Microstructural and mechanical properties

The microstructure of components manufactured using L-PBF is the result of fast cooling rates, directional heat transfer and multiple re-melting and re-heating cycles [4,31,40,45]. The created microstructure, besides being process parameter dependent, as discussed previously, is also material dependent. Regarding the microstructure, the metals used in L-PBF can be divided into two categories: columnar solidifying and cellular/dendritic solidifying [4]. Typically with pure metals [46], and alloys with a narrow solidification range, like Ti64 [4], the solidus-liquidus-interface is stable, leading columnar growth

along preferred crystal orientations aligned with temperature gradients [33,46]. With alloys with a wider solidification range on the other hand, constitutional undercooling may occur. In constitutional undercooling, alloying elements redistribute within the alloy, creating areas with different solidifying temperatures. Areas with higher solidifying temperature grow first, followed by other regions, leading to a cellular or dendritic microstructure [46]. The segregation of alloy elements to cellular walls has also been confirmed experimentally [7,47]

The thermal conditions of the melt pool during L-PBF is characterized by high cooling rates, due to the small size of the melt pool, anisotropic cooling, due to the build-plate and the previously built material conducting heat away more efficiently than the surrounding powder and partial re-melting of the previously deposited layers [7]. The high cooling rate of the melt pool leads to a very fine microstructure, effectively strengthening the material according to the Hall-Petch effect [7]. In addition to grain boundary strengthening, in 316L stainless steel, a high dislocation density in the as built material [7], a high amount of low angle grain boundaries [47] and a fine cellular structure with cell sizes between 1 and 0.5 µm [47–51], an example of which is presented in figure 10, all strengthen the material by hampering the movement of dislocations. Greater hardness [49] and higher yield strength and ultimate tensile strength have been reported for 316L [7,40,47] For instance, up to three times stronger material was reported by Wang et al [47].

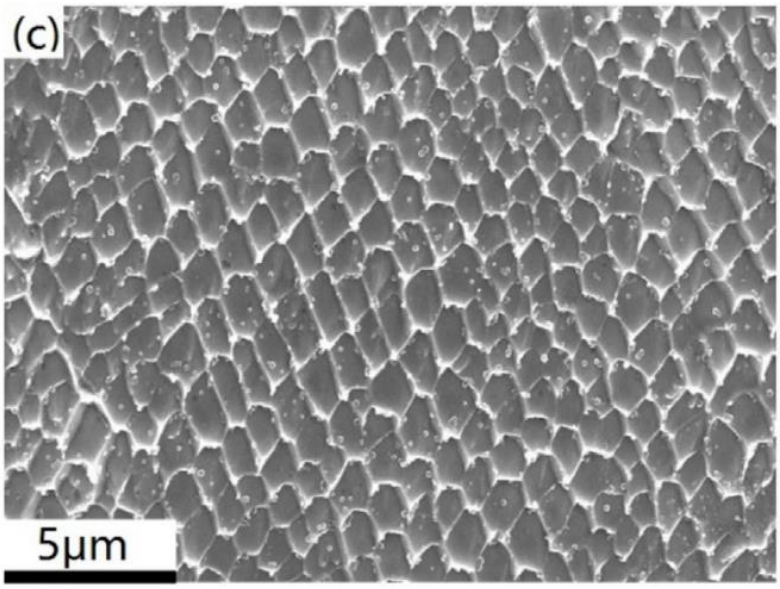

Figure 10: *Fine cellular microstructure in AM 316L* [51]

The anisotropic heat removal and re-melting of previous layers on the other hand promote epitaxial grain growth and produce a texture to the microstructure, with both columnar [33,52] and cellular [7,47] microstructures being oriented parallel to the thermal gradients i.e. the build direction. An example of microstructure anisotropy in AM 316L is presented in figure 11. Concerning individual grain orientation, the material is quite isotropic, as can be seen from the different colours of the grains in the EBSD maps. However, the shape of the grains is highly isotropic, with the grain boundaries oriented towards the build direction. The anisotropic microstructure leads to anisotropic mechanical properties, as has been experimentally reported for several materials, like 316L [7,50], Ti64 [52] and tantalum [53].

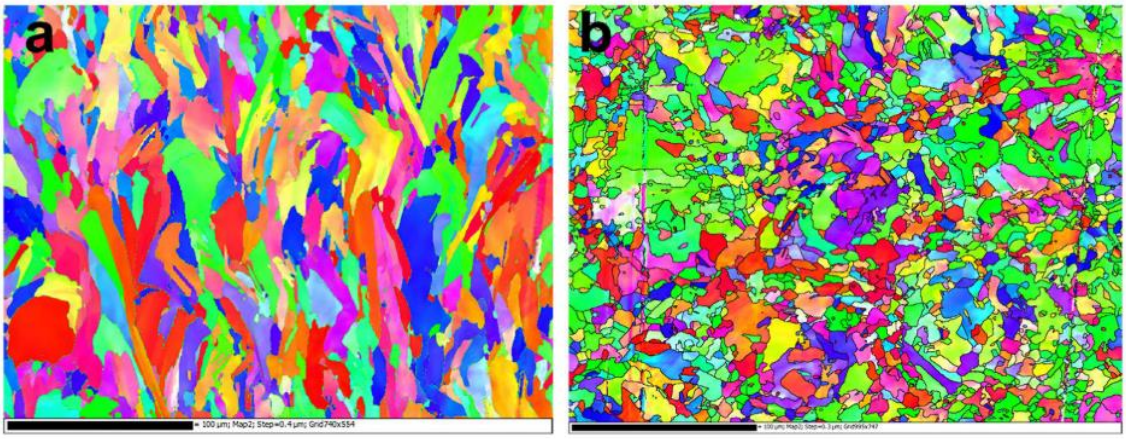

Figure 11: *EBSD maps of AM 316L with build direction a: vertical and b: perpendicular to the image* [7]

The fatigue properties of L-PBF manufactured components are characterized by the inherent defects created during processing. Rough surface finish, lack of fusion and gas porosities and metallurgical properties, like brittle intermetallic compounds can all act as stress concentrators with a detrimental effect on the fatigue life of the components. [3]

The surface quality of L-PBF components is not ideal for applications demanding fatigue resistance. It is caused by the staircase effect [39] discussed earlier and the partial melting and clinging of the feedstock powder to the undersides of overhanging features on components [54]. Spierlings et al [55] studied the effect of machining and polishing on the fatigue performance of 316L stainless steel, and found that machining significantly improved the fatigue performance of the material, with polishing providing further improvement. Similar findings regarding the surface roughness were made by Greitemeier et al [56], who compared the fatigue performance of Ti64 manufactured by L-PBF and

electron beam PBF (EB-PBF). They found, that the L-PBF component had a higher fatigue limit when compared to the EB-PBF, and attributed this improvement to the lower surface roughness of the L-PBF process (Ra=13 µm vs Ra=27 µm). Unfortunately, the source of this difference between surface qualities was not elaborated. They also found, that the fracture toughness of L-PBF samples could be improved by hot isostatic pressing (HIP). Same effect was not observed for the EB-PBF samples, because due to a high process chamber temperature of 630 ºC the microstructure did not contain martensite or forcibly dissolved alloying elements, which could then be mitigated by HIP.

Greitemeier et al [56] also studied the relative significance of surface quality and internal defects on fatigue performance by comparing as fabricated and machined components. They found an overall improvement in fatigue performance of milled samples over the as fabricated ones, as is to be expected, but they also concluded that the defects become the dominating feature only once the surface quality of the components is sufficient.

Internal defects are caused by entrapped gas, lack of fusion of the powder, balling [57] and denudation of the powder around the melt pool [41,43,58]. Pores caused by entrapped gas are considered less detrimental to static and dynamic properties due to their round shape. Other types of internal defects are more jagged, with the sharp corners acting as stress concentrators [3]. Hot isostatic pressing (HIP) has been shown to close internal pores and subsequently improve the fatigue performance [56].

Brandl et al [59] studied the effect of build orientation on the fatigue properties of AlSi10Mg alloy by printing test pieces in three different orientations, at 0, 45 and 90 degrees to the build plate. They found that the fatigue performance was best in the 0-degree direction, i.e. parallel to the build plate, when the build plate was preheated to 30 ºC. Increasing the preheating to 300 ºC improved the fatigue performance and decreased the differences between different build directions. This was attributed to a smaller number of defects due to the build plate heating. The anisotropy in dynamic properties was attributed to the anisotropic nature of the defects, rather than microstructural features.

2.3 State-of-the-art of powder bed fusion

In this chapter, some state-of-the-art techniques and studies into metal powder bed fusion are presented and discussed.

2.3.1 Residual stress control

Residual stresses are inherent to L-PBF manufactured components [60]. They are caused by the localized heating and cooling of the material. First, the laser beam heats the material, causing it to expand against the surrounding material, causing compressive stresses. Then, once the laser beam moves on, the material cools rapidly and contracts now constrained by the material it has bonded to, causing tensile residual stresses [30]. This process is illustrated in figure 12.

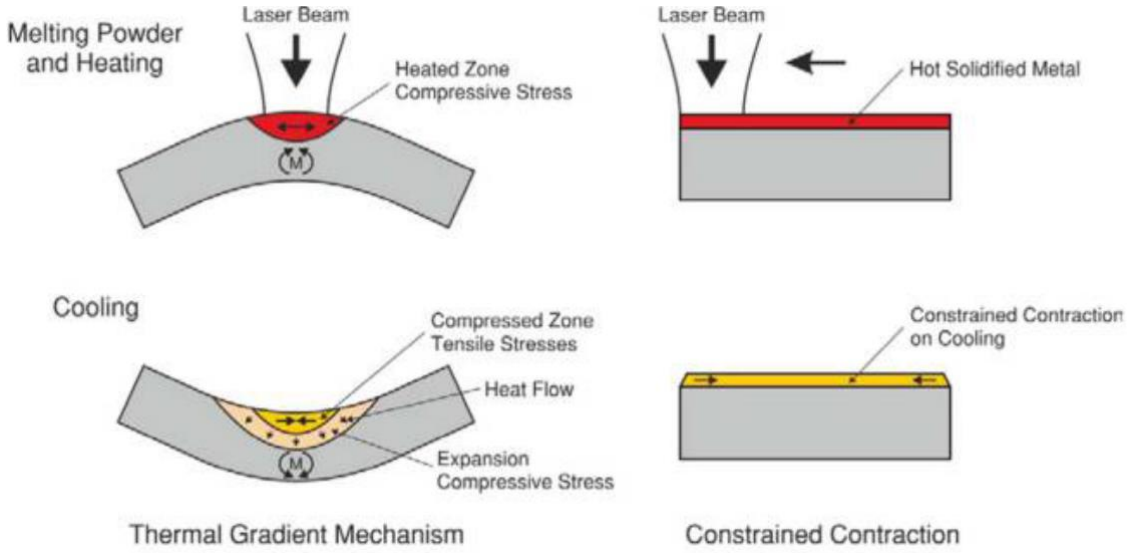

Figure 12: *Schematic of the generation of residual stresses* [30]

Residual stresses during manufacturing can cause the material to crack and delaminate [44] and deform [61], resulting in broken or warped components. It is thus of great interest to control and mitigate the generation and effects of residual stresses both in-situ and after the actual manufacturing process.

Residual stresses can be controlled in-situ by feedback control, thermal gradient control, scanning strategy control and mechanical control. Feedback control consists of monitoring the melt pool and powder bed temperatures and adjusting the laser parameters accordingly, though studies have mostly concentrated on developing techniques to monitor and correct defects like porosity [39]. Thermal gradient control includes minimizing the magnitude of thermal gradients by heating the substrate or the powder bed. Scanning strategy can be utilized to minimize the effects of residual stresses, and re-scanning can be used to reduce the magnitude of the stresses. Mechanical control attempts to replace the generated tensile residual stresses with compressive ones by using in-situ laser shock peening (LSP) [60].

Shiomi et al [32] studied the effects of re-scanning and powder bed heating on residual stresses, and found that re-scanning decreased the residual stresses by 55%, while powder bed heating decreased them by 40%. Robinson et al [30,36] studied the effects of different scan strategies on residual stresses and concluded, that the primary residual stresses are generated parallel to the scan vectors. Parry et al [17] studied the effect of scan vector length and concluded that longitudinal stresses increase linearly with scan vector length up to 3 mm after which they plateau. Transverse stresses on the other hand were found to be higher for scan vectors less than 2.5 mm long. These findings indicate, that the effects of scanning strategy on residual stresses are complex. Scanning strategy can be used to control the residual stresses, but it requires a high amount of designing and planning.

LSP could be used in-situ to introduce compressive residual stresses to the surface of the component, as proposed by Kalentics et al [62]. They studied the effect of LSP on L-PBF manufactured PH1 and 316L steel components after the building process and found that even a single LSP scan of the component was enough to chance the surface residual stresses from tension to compression. Compressive residual stresses on the surface are known to stop SCC from initiating [13].

Post-processing methods to control and mitigate residual stresses include heat treatments, shot and laser shock peening and machining [60]. Shiomi et al [32] found that a heat treatment at 600 and 700 ºC was enough to reduce tensile residual stresses by 70% in a mixture of chrome molybdenum steel (JIS SCM440) (69.6 w-%), copper phosphate (8.7 w-%) and nickel (21.7 w-%). Tong et al [63], who studied the effect of heat treatment on the residual stresses of an FeCrCoMnNi high-entropy alloy produced by directed energy deposition (DED) found that heat treating for four hours at 700 and 1100 ºC decreased the residual stresses by up to 90% (from 450 MPa to 50 MPa).

2.3.2 Residual stress measurement techniques

Residual stress measurement techniques used to characterize additively manufactured components include X-ray diffraction (XRD) [64], neutron diffraction [8,61] and the contour method [36]. Of these methods, XRD and neutron diffraction are non-destructive [65], while the contour method requires the sample to be cut [66].

XRD and neutron diffraction are both based on the phenomena of diffraction, where the selected radiation interacts with the sample's lattice structure and produces a diffraction

pattern. The residual or applied stresses lead to strains in the lattice, and these strains cause the diffraction pattern to change, making it possible to calculate the stresses in the sample by observing the changes in the diffraction pattern. The practical difference between XRD and neutron diffraction is, that XRD only penetrates a few microns of the sample surface, while neutron diffraction can penetrate several millimeters. This means, that XRD can only measure the residual stresses in two dimensions at the sample surface, while neutron diffraction can measure the stresses at depth in three dimensions. Another difference is the fact that neutron sources are massive installations where a peer-review process precedes access. XRD measurement devices on the other hand are quite small and well available. [65]

The contour method makes it possible to study the residual stress profile in a chosen cross-section of a sample. The sample is cut along the section of interest using electric discharge machining, so as not to generate any unwanted residual stresses to the sample. The cross-section will deform as it is cut, and this deformation can be measured using a co-ordinate measuring machine (CMM). Once the surface is measured it can computationally, using a finite element model of the sample, be forced back to its original shape, and the residual stress state can be calculated. [66] The principle of the contour method is illustrated in figure 13.

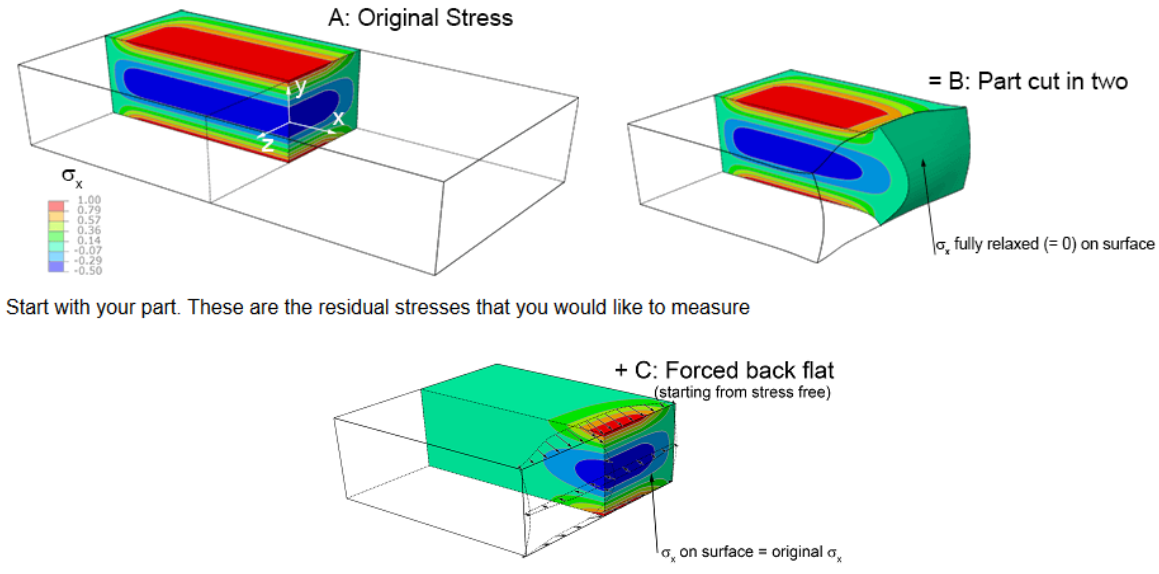

Figure 13: *The principle of the contour method* [66]

Coordinate measuring machines can also be used to non-destructively quantify the strain in a component, and thus indirectly measure the stress in the component by comparing the CMM data to the original shape of the component. [61] Similarly, 3D-scanning can

be used to determine the actual shape of the printed component. The scan data can then be compared to the 3D-model of the component, to determine possible strains and dimensional accuracy. [67]

2.3.3 Tailored microstructures

The ability to change the morphology of the materials microstructure during processing would allow designers to tailor site-specific properties to their components. Several studies in to tailoring microstructures have been performed, with techniques including changing the scan strategy [33,68,69], beam power [70–72] and beam profile [29].

Thijs et al performed two studies [33,69] in to the effect of scan strategy on the microstructure. They found, that the microstructure grows parallel to the local thermal gradient, and that by changing the hatch angle between layers the texture generated by this preferential growth could be mitigated.

Parimi et al [72] and Xiang et al [71] studied the effect of laser beam power on the microstructure of IN718 and CrMnFeCoNi high entropy alloy respectively during directed energy deposition (DED). Xiang et al [71] found, that a higher laser power of 1400 W resulted in a more anisotropic microstructure, where as a power of 1000 W resulted in a highly isotropic microstructure. Parimi et al [72] on the other hand found, that a power of 910 W generated an isotropic microstructure, whereas a lower power of 390 W resulted in only a weak texture. Parimi et al postulate, that the heat input of the 1000 W beam was enough to trigger epitaxial growth with the heat flux being almost vertical. The lower beam power on the other hand would create a smaller melt pool, which would cool faster and cause equiaxed growth. Xiang et al [71] had similar results of epitaxial growth at a similar laser power of 1000 W (versus 910 W). Increasing the power further to 1400 W they achieved again equiaxed growth, postulating, that at this high heat input the heat flux becomes isotropic, resulting in only weak texture. Is must be noted though, that the materials studied in these two studies were different.

Niendorf et al [70] studied the effects of laser beam power on the microstructure of 316L during L-PBF and achieved similar results as Parimi et al [72] with DED. Niendorf et al found, that at 1000 W the microstructure of 316L was highly anisotropic and oriented towards the build direction. The gains had grown epitaxially parallel to the thermal gradient. At a lower power of 400 W, the grains showed a slight preferred orientation in the structure, but it was significantly less than with the 1000 W beam. The grain size of the

400 W processed material was also smaller. The microstructures obtained in their study are presented in figure 14. They also performed tensile tests on the differently processed materials and found the 400 W processed material to be stronger, in line with the Hall-Petch relation.

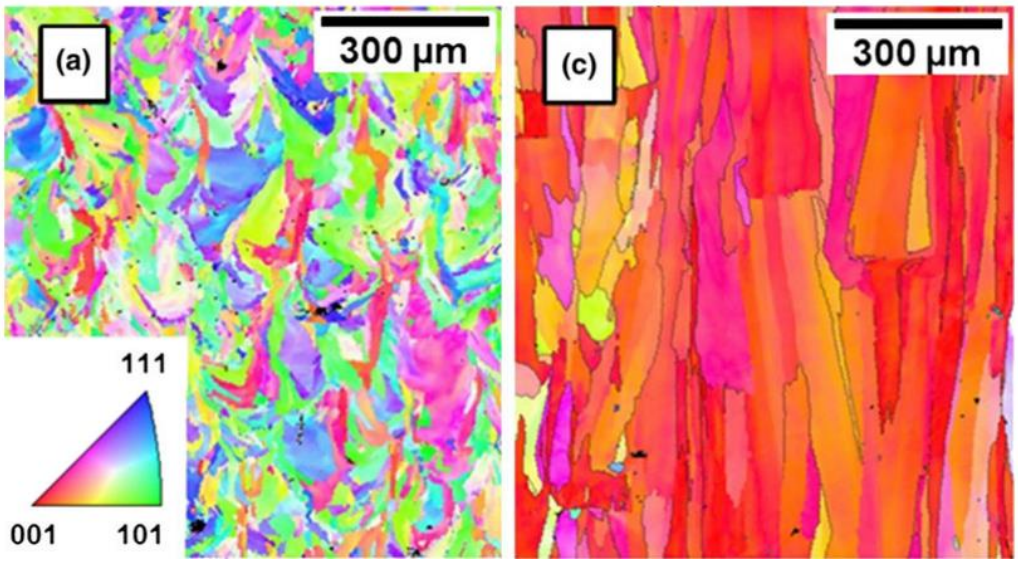

Figure 14: *EBSD images of AM 316L processed with a beam power of a: 400W and b: 1000W* [70]

Roehling et al studied [29] the effect of different beam profiles, namely circular and elliptical, to the microstructure of 316L stainless steel. They found, that by changing the beam profile from circular to elliptic and keeping all other parameters unchanged, they could achieve an equiaxed microstructure, instead of a columnar one. This could, in theory be used to control the microstructure-induced anisotropy of components.

Dehoff et al [68] demonstrated the ability to tailor microstructures in practice by effectively writing the letters D, O and E in to the microstructure of a piece of IN718 manufactured by EB-PBF. This was achieved by modulating the electron beam current and beam scanning velocity, which allowed the authors to change the solidification mode of the material between columnar and equiaxed in-situ. The achieved microstructural text can be seen in the EBSD map presented in figure 15.

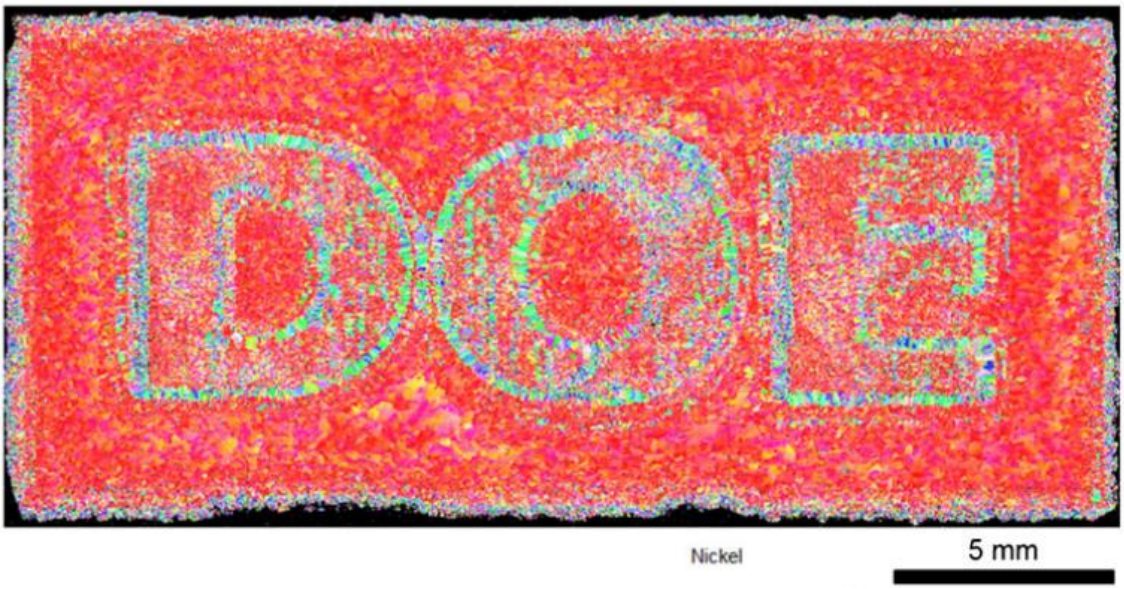

Figure 15: *EBSD map of in IN718 piece with tailored microstructure* [68]

2.3.4 Compositionally graded alloys

Welding dissimilar metals and changing the local chemical composition of materials by for example nitriding or carburizing have been used for years, but a new method for creating materials with site specific properties using AM is just emerging. The nature of adding material layer by layer during AM makes it possible to change the composition and even the entire material during processing, giving unprecedented control over where in the component to apply different chemical compositions and properties. These functionally graded materials (FGMs) allow designers to use more expensive high performance materials in just the areas they are needed. [73]

The interface between compositions or materials can be abrupt or graded, as shown in figure 16 [73].

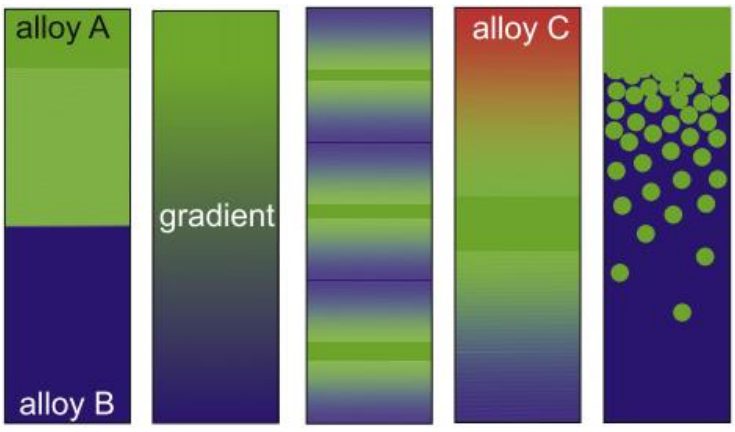

Figure 16: *Examples of different interfaces in FGMs* [73]

A gradual change in material composition may be more beneficial, as it also provides a gradual change in properties like coefficient of thermal expansion and hardness [3]. Mukherjee et al [28] showed in their simulations, that a graded joint between Ti64 and 800H iron-nickel alloy, two very different materials mechanically, contained more gradual changes in residual stresses. An intermediate material can also be used to allow transitions between two otherwise incompatible materials, as was attempted by Reichardt et al [74] with an attempted transition from Ti64 to 304L stainless steel via vanadium.

A third interface option besides abrupt and graded is a graded metal matrix composite structure, where a reinforcing constituent is introduced into a metal matrix by gradually increasing its percentage [75,76].

The constant material feed of DED makes changing the composition of the deposited material quite flexible and easy, making DED the primary method for manufacturing FGMs [3]. Using L-PBF to manufacture FGMs has inherent limitations, as the grading can only be done layer by layer, unless the unsolidified powder is removed before another powder is deposited [77], but this adds another step to the process. Despite this limitation, some studies have been performed into FGMs manufactured using L-PBF [75–77].

Shishkovsky et al [75] and Mumtaz and Hopkinson [76] both studied the L-PBF of metal matrix composites, with the first studying TiC in NiCrSiB matrix and the latter studying zirconia powder in Waspalloy nickel alloy. Both teams reported successfully depositing graded composites. Shishkovsky et al [75] found that the microhardness of the material increased with increasing TiC content. Mumtaz and Hopkinson [76] reported that the layers were better mixed when a cross-hatching scanning strategy was used.

Anstaett et al [77] studied the combined (i.e. both materials in the same part in discrete areas) and mixed (i.e. mixed powder) L-PBF processes of 1.2709 tool steel and CuCr1Zr alloy. They found, that during combined AM, the manufacturing order had an impact on the interface between the metals. If the tool steel was deposited on top of the copper alloy, mixing of the two materials was more substantial, as both materials were in liquid state at the same time.

3. EXPERIMENTAL

For the experimental part of this study, two sets of samples were studied. First, samples with simple strip geometry were studied, followed by more complex rapid mixing nozzles. The strip samples consisted of both additively manufactured as well as cold rolled sheet materials. The sample strips were made of EN 1.4432 (316L) stainless steel. The rapid mixing nozzles were made of unspecified grade of 316L stainless steel.

3.1 Methods and materials of the strip sample studies

The co-ordinate system and nomenclature used to refer to different parts of the sample are presented in figure 17.

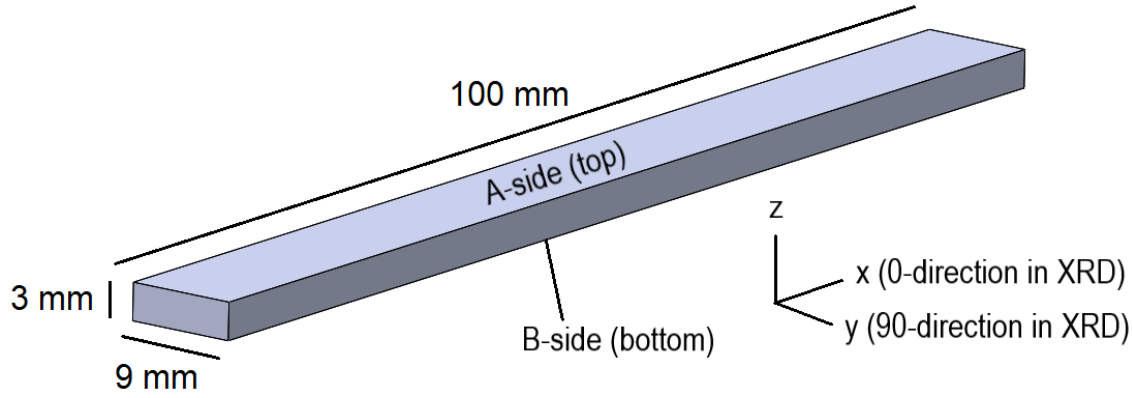

Figure 17: *Co-ordinate system and nomenclature used to refer to the samples*

The samples to be studied were designed to match B-type U-bend samples according to ASTM G30 [78] giving them dimensions of 100 by 9 by 3 mm. U-bed testing geometry was chosen, as U-bend testing was envisioned as one experimental method. Twelve of these strips were to be produced with four different post process treatments applied. Three of the samples were to be in the as built condition, three were to be shot peened, three stress relief annealed and three both shot peened and annealed.

In the following chapters the process of producing the sample strips and reference samples and the experimental methods used are presented.

3.1.1 3D printing

The strip samples were manufactured by 3D Formtech on an EOS M290 L-PBF machine. Initially the printing was attempted on a tooth-like support structure, but the residual stresses generated in the strips were so strong, that it tore the heads of the strips loose from the support structure, as presented in figure 18, forcing the printing to be stopped.

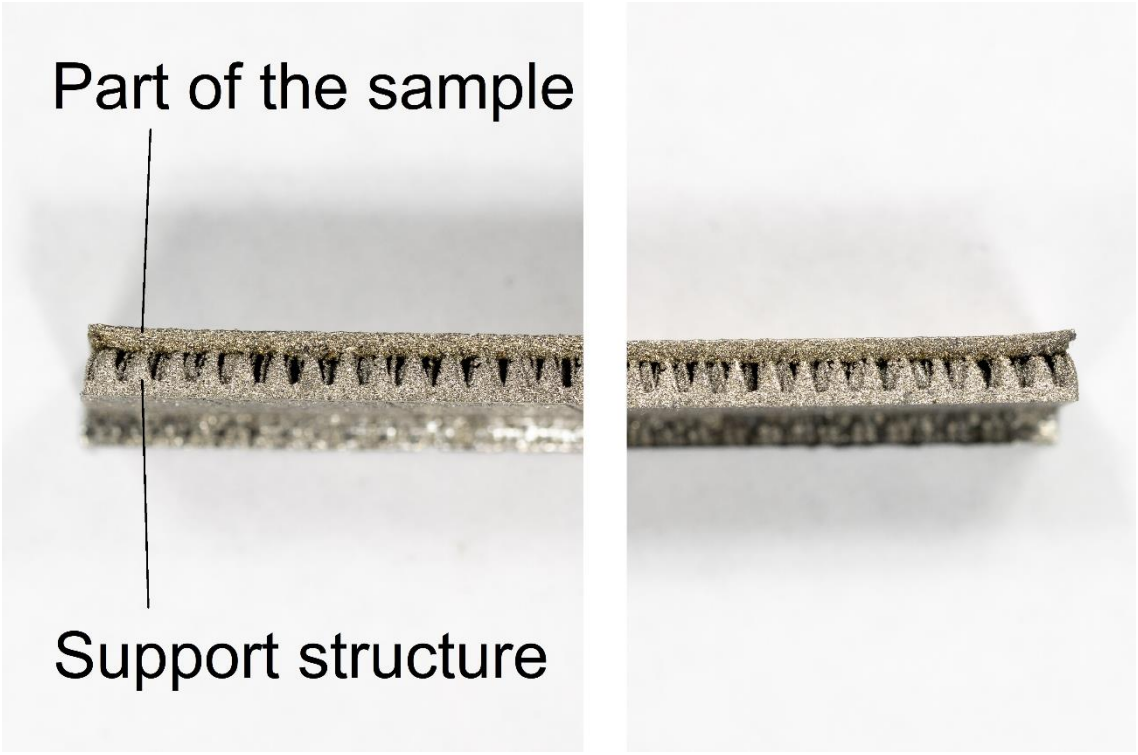

Figure 18: *Two images illustrating the tear at the ends of the samples*

Next, printing on a solid support structure was attempted. This means that fully consolidated material was printed right from the start, with the idea that a thick enough section would be printed so that once removed by band saw the samples would be 3 mm thick. Unfortunately, the recoater blade of the printer caught one of the samples and bent it, forcing the printing to be stopped. It was decided, that the remaining 11 intact samples of 2.5 mm thickness would do.

After the as built samples were removed from the build plate, they were visibly bent upwards, as shown in figure 19.

Figure 19: *As built sample (below) against a reference (above) showing visible bending upwards after removal from build plate*

This bending was to be expected, as the stress state of the as built samples was expected to be similar to one achieved in a previous study by Ghasri-Khouzani et al [61].

The samples were printed all at the same time with the 100 by 9 mm surface parallel to the build plate. The printing parameters used were the recommended settings given by EOS-printing software, and were as follows. Hatch angle rotation of 47 degrees and layer height of 40 µm. Edges of samples were printed with 100 W laser power and 900 mm/s scanning speed, while the infill was done at 214.2 W, 928,1 mm/s and with 100 µm hatch spacing. The top surfaces of the samples were printed with 150.2 W, 514.9 mm/s and with 100 µm hatch spacing. The bottoms of the samples were printed with the infill parameters, as the samples were cut from solid material.

After printing, five of the 11 samples were cut loose from the build plate. The remaining six were sent for heat treating.

3.1.2 Heat treatment

The six samples remaining on the build plate were stress relief annealed at 1030 ºC for 60 minutes under a vacuum. After annealing they were cooled using flowing nitrogen gas. After heat treating the samples were cut from the build plate using a band saw.

3.1.3 Shot peening

Three samples cut from reference material (EN 1.4404, the low molybdenum variant of 316L) provided in 3 mm thick sheets, as well as two of the as built samples and three of the heat-treated samples were shot peened with Silicon carbide shot. The Vicker's hardness of silicon carbide is reported to be in the 2000 HV range [79,80], making it much harder when compared to the steel samples. As the shot is harder than the material being peened, variations in the shot's hardness will not affect the peening intensity [13]. The pressure in the shot peening system was 7 bar and the flow rate of the shot was calculated to be 11.4 grams per second. The peening was performed from roughly 20 cm away for about one second per surface. Of each type of sample (reference, as built, heat treated) one was peened once, one twice and one three times (except with the as built samples which we only had two of).

3.1.4 316L sheet

For reference, samples with similar dimensions (100 by 9 by 3 mm) were cut from 316L sheet. Reference material is cold rolled sheets of both the high (EN 1.4432) and low molybdenum (EN 1.4404) variants of 316L with chemical compositions presented in table 4.

Table 4: *Chemical compositions of the reference materials* [10]

	C	Cr	Ni	Mo
EN 1.4404	0.02	17.20	10.10	2.10
EN 1.4432	0.02	16.90	10.70	2.60

The reference material was cold rolled, heat treated, pickled and skin passed.

The low molybdenum variant was provided in three mm thick sheets, while the high molybdenum variant was only available in 1.95 mm thick sheets.

For referencing the effect of shot peening, three samples were cut from the low molybdenum three mm sheet, and residual stresses were measured in the 100 mm long direction using XRD. The measurements were performed from the middle of the 100 by 9 mm surface, from both sides of the samples. The measurements were performed only in one direction due to schedule limitations. Next, the three samples were shot peened as described earlier (one once, one twice and one three times) and after shot peening the

residual stresses were measured again. The reference samples before and after shot peening are presented in figure 20.

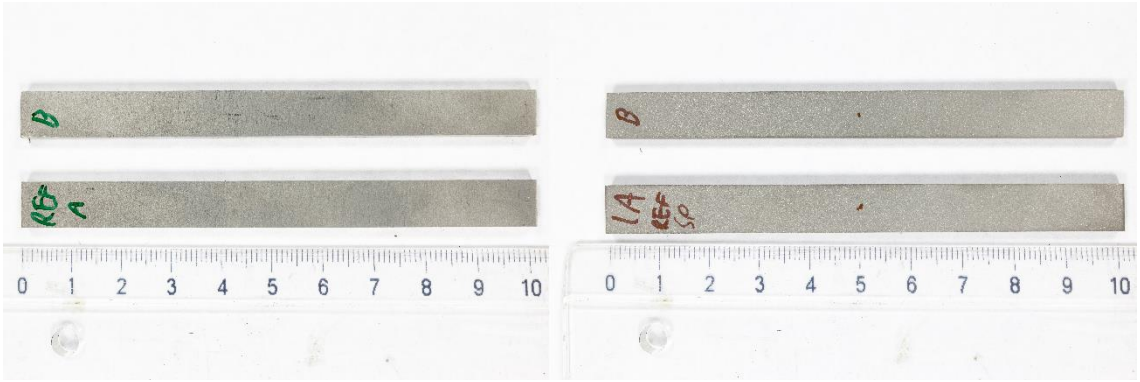

Figure 20: *Reference samples before (left) and after shot peening*

In addition to the shot peened reference samples, references for the corrosion tests were cut from both high and low molybdenum 316L sheets.

High molybdenum strips of the same dimensions (100 by 9 by 3 mm) were cut in half, and consequently welded back together to obtain a microstructure and stress state of a welded structure. The welds were performed by stick welding with sticks cut from the same sheet as the samples, to ensure the chemistry of the material remain nominal. Welded material was chosen as one reference sample, as AM components would most likely be used in some form to replace a structure made by welding.

3.1.5 AM316L

The material studied in this work was the high molybdenum variant of the austenitic stainless steel 316L (EN 1.4432) [81], with a chemical composition presented in table 5.

Table 5: *Nominal chemical composition of the studied 316L variant* [9]

Element	Fe	Cr	Ni	Mo	C	Mn	Cu	P	S	Si	N
w-%	balance	17-19	13-15	2.25-3	0.03	2.00	0.50	0.025	0.01	0.75	0.10

The material was initially in powder form, from where it was then processed by L-PBF to create the samples.

Generally speaking, 316L is a low carbon austenitic stainless steel with good weldability [81], a trait required for additive manufacturing as well.

For stress corrosion cracking (SCC) to take place, two conditions must be fulfilled. First, the material must be metallurgically susceptible, and second, it must be under a residual or applied tensile stress state. [78] 316L is known to be susceptible to chloride induced SCC, but the added molybdenum is designed to counter this [81]. This SCC susceptibility has been studied with laser engraved material [12] and in a failure analysis case [82], though in both cases the material was of the low molybdenum quality. In the study by Krawczyk et al [12], 316L with laser engraving induced tensile residual stress was studied and compared to U-bend test specimens. Both samples displayed similar SCC properties and crack formation in a chloride containing test environment. Mayuzumi et al [11] studied chloride induced SCC in 304L and 316L, and concluded that a threshold stress, a stress below which no SCC takes place, for 316L is at least 25% of the material yield stress, assuming some pitting of the surface causing suitable defects to form and act as initiation sites. If not pitting would have occurred, the authors calculated that the threshold stress required to initiate SCC from a smooth surface could be as high as 56% of the yield stress [11].

Plastic deformation has been shown to transform some of the austenitic microstructure in conventionally processed 316L into martensite [83,84] at low temperatures (77K and 103K respectively). The martensite transformation was more limited at room temperature. But a study in to L-PBF manufactured 316L found that the high density of low-angle grain boundaries and a fine cellular microstructure, typical of L-PBF [47], supressed the generation of strain-induced martensite even at low temperatures (80 K) [51].

The additively manufactured samples with different post process treatments are presented in figure 21.

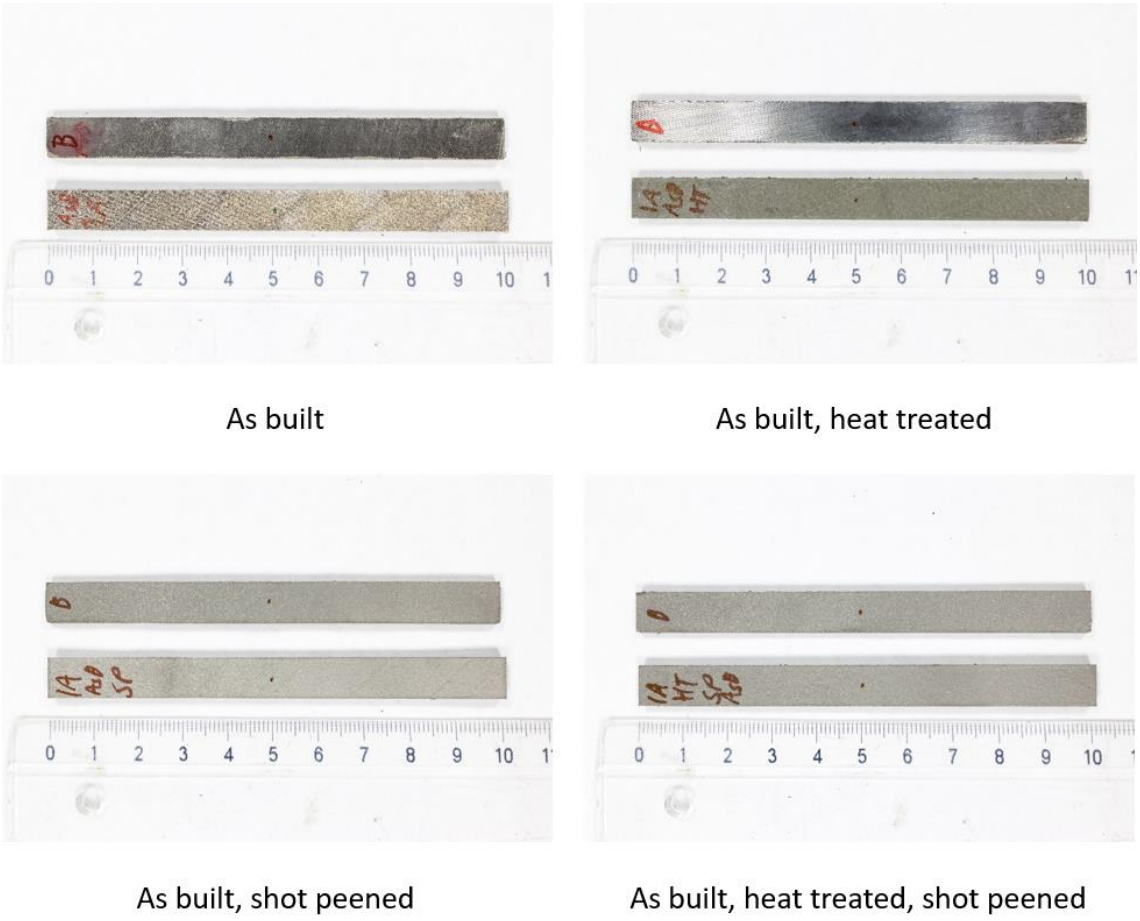

Figure 21: *Additively manufactured 316L samples with different post process treatments*

3.1.6 Metallography

Metallographic observations were performed by mounting the samples in phenolic resin, grinding the cross sections down to 2000 grit using wet sanding paper. Next, the samples were polished using 3 and 1 µm diamond suspensions to a mirror finish. Etching, where necessary, was done using a Struers MoviPol-5 electrolytic polisher with 10% oxalic acid as the electrolyte using 10 second etching time, 20 V as the voltage an a flow rate of 10.

Optical observations were performed using conventional and stereo microscopes at magnifications ranging from 5x to 100x. Scanning electron microscopy (SEM) was performed at Tampere Microscopy Center's Zeiss UltraPlus field emission SEM.

3.1.7 Corrosion testing

In order to evaluate the chlorine induced stress corrosion cracking behavior of the AM 316L and reference material, 4-point bending (4PB) test rigs were manufactured from aluminium. Aluminium was chosen, despite a known susceptibility of some aluminium

alloys to SCC [85,86], because it was available. The 4PB rigs were painted using an epoxy paint to protect the aluminium from SCC in the first place, and secondly the rigs were designed to be large compared to the samples so that the stress state in the rigs would not be significant. The rollers in contact with the samples were made from 3 mm plastic, to insulate the samples from the rigs electrically. A stainless steel bolt was chosen as the fastener and the threads were impregnated with Vaseline, to prevent the solution from corroding them. A 3D-model and an image of a painted 4PB rig with a sample in it are presented in figure 22.

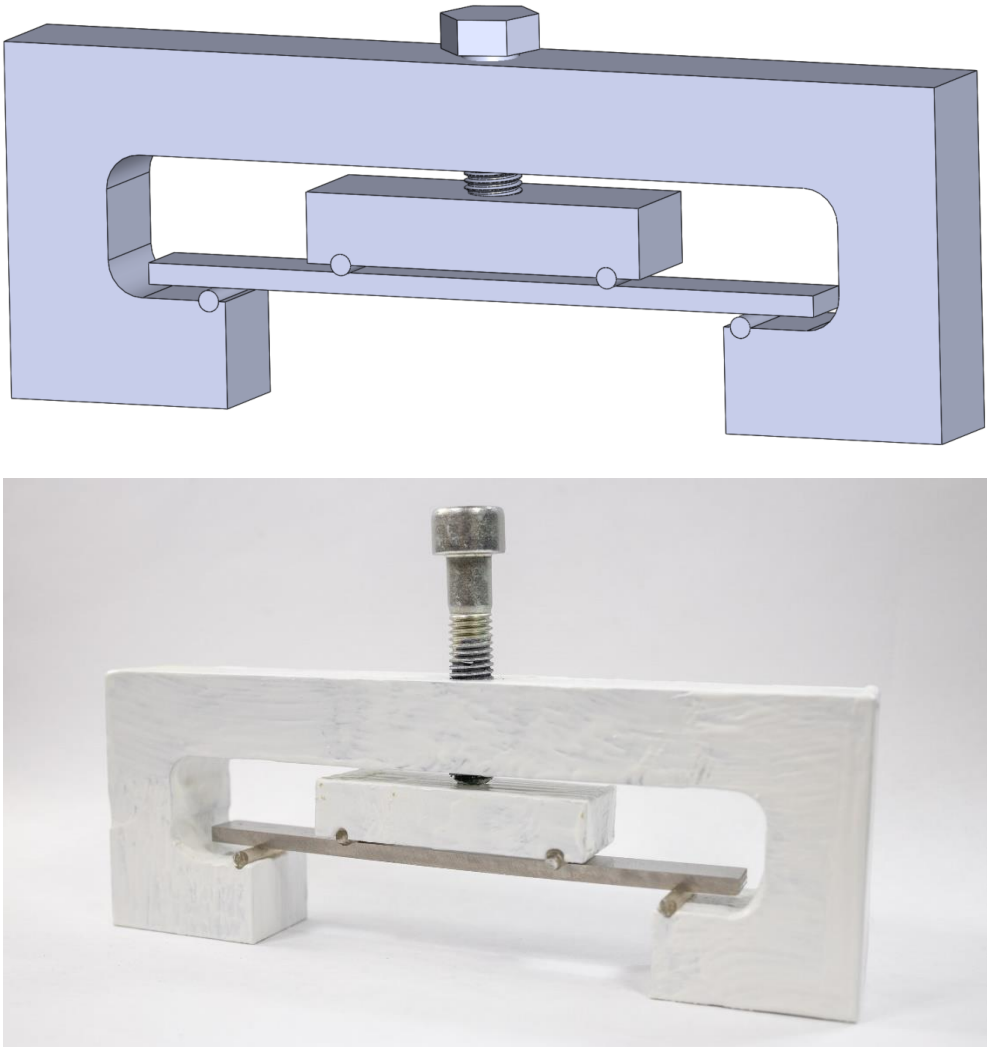

Figure 22: *3D model and an image of the 4-point bending rigs*

During 4-point bending, the area of maximum tensile stress is between the inner supports on the underside of the sample. The stress in this area is also constant, making the 4PB a very useful method for evaluating SCC. [78]

A general rule of thumb has been, that non-sensitized austenitic stainless steels do not experience chlorine induced SCC under 60 ºC [87]. There have been cases though, where this rule has been shown to be false, like for instance in a failure analysis case by Sjong and Eiselstein [88], where they determined, that a 316L rock climbing anchor had undergone chlorine induced and acidic soil water assisted trans granular SCC. Despite this rule having been proven obsolete, it was still decided that the testing environment in the current study would be above the 60 ºC limit, namely at 80 ºC, to make sure SCC would eventually happen.

Due to equipment limitations, the standardized ASTM G36 boiling magnesium chloride test was not possible, but is was still decided, that the testing solution would be magnesium chloride, as it is widely available and it has been shown to be more corrosive than sodium chloride [89]. A 50 w-% solution was decided on. As no pure $MgCl_2$ was not available, an amount of commercial $MgCl_2$ used for ice removal and dust control was bought, with a rough chemical composition presented in table 6.

Table 6: *Rough chemical composition of the used magnesium chloride, as provided by the producer*

Substance	w-%
Magnesium chloride (anhydrous)	47.2
Magnesium sulfate	0.2
Potassium sulfate	< 0.2
Potassium chloride	0.4
Sodium chloride	0.7
Iron	5.0 ppm

In order to achieve a 50% $MgCl_2$ solution by weight, 1060 grams of the compound was measured and dissolved in 1000 milliliters of water for each batch.

For the initial test series, four samples with different microstructure were chosen: as built, heat treated AM, reference strip of EN 1.4432 and a reference strip with a weld in the middle of it. To simply test whether SCC would occur at all, a stress magnitude of 75% of the material yield strength was chosen. The required stresses were then calculated from the yield strengths given in each materials datasheet: 470-590 MPa for the EOS 316L and 240 MPa for the EN 1.4432. For the EOS 316L 350 MPa was chosen as the desired stress, while for the EN 1.4432 it was 180 MPa. To achieve these stresses the required clamping force F was calculated according to ASTM C1161 [90], which states

that for a 4PB test rig with an inner span half of that of the outer span L, the maximum stress at the sample σ_f is

$$\boldsymbol{\sigma_f = \frac{3}{4}\frac{FL}{bd^2}}, \quad (2)$$

where F is the clamping force, b is the width of the sample and d is the height of the sample. The geometry of the rig is presented in figure 23.

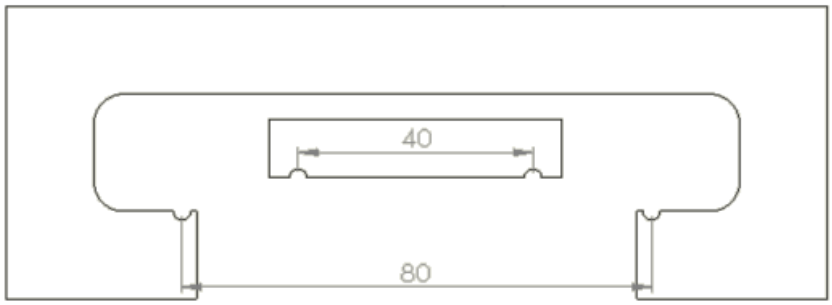

Figure 23: *The geometry of the 4PB rig*

By rearranging equation (2), the required forces of 328.1 N for the EOS 316L and 102.7 N for the EN 1.4432 were calculated. Then, using the empirical formula relating bolt clamping force to its torque T,

$$\boldsymbol{T = KDF}, \quad (3)$$

where D is the diameter of the bolt, 8 mm in this case, and K is the coefficient of friction, estimated to be 0.15, the required torque was estimated. These values were 394 Nmm for the EOS 316L and 123 Nmm for the EN 1.4432. These estimations were admittedly extremely rough, but it gave a starting point. Eventually, after initially tightening the bolts (roughly, as no accurate enough torque wrench was available) to the specified torques, the actual stress states in the samples were measured using XRD, adjusted accordingly and measured again to reach the desired stress states.

The as built, reference and welded reference samples were painstakingly iterated to their correct torques, but the heat treated AM sample was more problematic, seemingly loosening a bit after every other tightening or so. It was eventually realized, that the 350 MPa stress would be enough to yield the sample, as the sample was in a stress relief annealed condition, ostensibly giving it the same mechanical properties as the reference material has. In hindsight, the material obviously yielded, relaxing the stresses after tightening. It was decided that the achieved stress of just over 200 MPa would do.

A 50 percent solution of $MgCl_2$ was prepared, the samples submersed and the containers put in a thermal cabinet set at 80 ºC. The next morning, after about 13 hours of exposure, the samples were checked on. At this point it became obvious, that the plastic dowels between the sample and the testing rig softened significantly at 80 ºC, causing the samples to embed themselves to the dowels, relaxing the stress state. The initial test was terminated. After removing the samples from the rigs, the previously reckoned yield in the heat treated AM sample was confirmed, and is presented in figure 24.

Figure 24: *AM heat treated sample after initial 4PB test showing significant yielding*

For the second attempt the plastic dowels were swapped to painted aluminium ones. The attempts at tensioning the specimens using the XRD were abandoned, and the tensioning was done using strain gages to measure the strain, and by using Hooke's law and the materials' Young's moduli, to calculate the achieved stresses. Two millimeter strain gages manufactured by Kyowa, and with a gage resistance of 120.4 Ohms and a gage factor of 2.11 were used, and the gages were glued to the middle of the samples, except with the welded reference, where it was offset from the middle to avoid the weld bead. The strain gages attached to the samples are shown in figure 25.

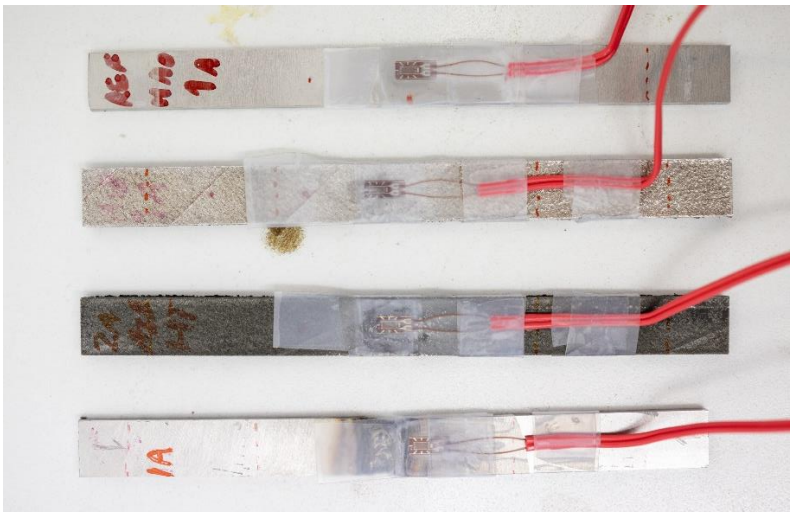

Figure 25: *4PB test samples with 2 mm strain gages attached*

The heat treated AM sample that had yielded was swapped to a new sample, while the three other samples, despite having already been subjected to an unknown time of possible SCC conditions, were not swapped. The reason for this was partly time limitations, as the residual stresses had to be measured from each sample before being subjected to corrosion, and partly because the purpose of this particular test is to investigate the effect of different microstructures on SCC behavior. The three "reused" samples were observed under an optical stereo microscope and the surfaces seemed pristine.

The strain values were measured using a National Instruments cDAQ-9171 with an NI-9219 analog input module. The strain values from this hardware was read using LabVIEW software. The required strain values were calculated from the required stress values of 350 MPa for the as built sample, and 180 MPa for the rest of the samples, and the Young's moduli given in the materials' datasheets, 185 GPa for the EOS 316L and 200 GPa for the EN 1.4432. The heat treated AM sample was assumed to have a similar yield strength of 240 MPa, as the reference material. These calculations gave the required strain values as given in table 7.

Table 7: *Required micro strain values to reach 75% of the material yield strength*

Sample	As built	AM heat treated	Reference	Reference welded
Micro strain	1890	970	900	900

The samples were strained in the 4PB rigs to the required strain values, and while the strain gages were still attached and measuring, the stress state from each sample was measured three times using XRD. The results are presented later in this report, but at

this point it is worth mentioning, that the XRD results varied greatly from point to point, and differed from the expected values significantly. Despite this difference in results between the methods, this time it was decided that the strain gage values were more reliable. The strain gages were removed, and the samples in their rigs placed again in 50% $MgCl_2$ solution and into the thermal cabinet set to 80 ºC.

After being exposed for 237 hours the samples were removed and thoroughly washed. Next, the samples were cut so that the 40 mm section in the middle of the sample could be mounted in to phenolic resin. The samples were mounted to that the now 40 by 2.7 or 1.95 mm side was exposed. The samples mounted in the resin are presented in figure 26.

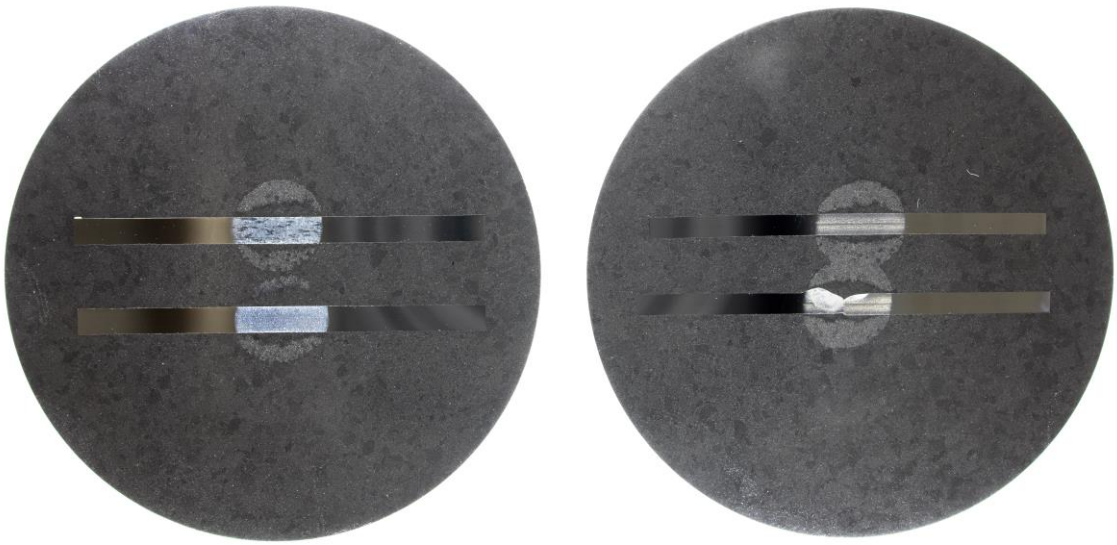

Figure 26: *Cross sections of the first corrosion test samples*

Next, the samples were ground down to 2000 grit using silicon carbide papers with water lubrication. After grinding, the samples were polished using 3 µm and 1 µm diamond suspensions. The cross sections were observed using traditional and stereo optical microscopes, manufactured by Leica, with magnifications ranging from 10x to 100x. No cracks were detected. Next, the samples were ground and polished again, so that 0.5 mm of material was removed to reveal material closer to the middle of the samples. The

cross sections were again observed using optical microscopes, but no cracks were detected.

It was decided that another corrosion test, this time with longer exposure time would be conducted. Strain gages were attached to a fresh set of samples (AsB, AsB HT, Ref and Ref welded). They were installed to the 4PB rigs and tensioned to the strain values specified in table 7. The strain gages were removed and the samples placed in fresh 50% $MgCl_2$ solution and into a thermal cabinet set to 80 ºC. After being exposed for 674 hours the samples were again removed, washed, cut, mounted, ground so that 1 mm of material was removed, polished and etched. This time 1 mm was removed, to study the sample closer to the middle. After etching, the cross sections were observed with both simple optical and stereo microscope at various magnifications. The cross sections seemed identical to the previous tests and no cracks were observed. Further two millimeters of material was removed to observe the samples closer to the middle of them. The cross-sections were again polished, etched and observed using both traditional optical and stereo microscopes, but no cracks were observed.

3.1.8 X-ray diffraction

X-ray diffraction (XRD) is a non-destructive measurement technique that can be used to measure the strain in a crystalline material's lattice, and by using the elastic constants of the material, the residual or applied stress in the material can be calculated. The technique is based on Bragg's law, which states that

$$\boldsymbol{n\lambda = 2dsin(\theta)}, \tag{4}$$

where n is an integer, λ is the wavelength of the x-rays used, d is the lattice spacing and θ is the diffraction angle. A stress in the material, applied or residual, causes the lattice spacing d to change, which in turn changes the position, or the angle of the diffraction peak. This change can be detected and the true lattice spacing calculated. [91]

X-rays penetrate crystalline material by only a few micrometers, making X-ray diffraction suitable only for near-surface characterization. Techniques have been developed to characterize the residual stress profile a few millimeters under the surface by removing material layer-by-layer using electro polishing for instance, but these techniques are not strictly non-destructive anymore, as material is being removed. [91]

The width of the XRD peak is known to correlate to microstrains, dislocation density and hardness of the material [92,93] with an increase in any of these broadening the peak. This makes not only the measured stress, but also the full width at half maximum (FWHM) value a useful tool for characterizing metallic materials.

In this study, the residual stresses from an austenitic steel at lattice plane (311) with a diffraction angle of 148.9 degrees were measured using chromium K beta peak as the x-ray source. A Stresstech Xstress 3000 G2 x-ray diffractometer with a chromium x-ray tube at 30 kV and 6.7 mA was used. Collimator size was 3 mm and the measurements were made using five tilt angles in each direction with maximum tilt being 40 degrees in each direction. Five degree tilt oscillation was used. Exposure times were mostly 25 seconds, though sometimes, especially with shot peened samples, 40 seconds was required to achieve acceptable minimum intensity. Software used for data acquisition and processing was Stresstech XTronic. For the stress calculations, software defaults were used for the Young's modulus and Poisson's ratio, 196 GPa and 0.28 respectively. For some of the samples, peak limits were used for the calculation.

The residual stresses of the sample strips were measured from six different points, three on each 100 by 9 mm surface of the sample, as shown in figure 27. One of the three points one was in the middle of the surface and two were equidistant at 15 mm from the middle one. Additionally, two more points were measured another 15 mm from the previous ones on the top surfaces of the as built samples. With the welded reference samples, the measurements were made in the middle (0 mm) and at 5 and 9 mm from the center, to characterize the stress state at the weld. Some of the points are presented in figure 27.

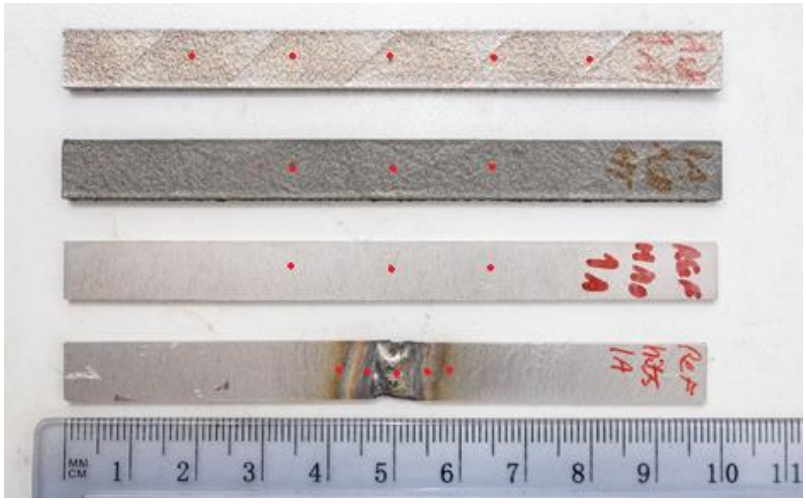

Figure 27: *XRD measurement points on the samples' top sufaces*

Additionally, several residual stress depth profiles were measured by first measuring the stress state at the surface of the material. Next, some material was removed by electrolytic polishing using a Struers MoviPol-5 system with A2 electrolyte. The amount of removed material was measured using a dial gage, and the residual stresses measured again. This process was repeated a number of times for each profile.

3.1.9 Hardness measurements

Hardness measurements were made using a Matsuzawa MMT-X7 microhardness measurement device with a test load of 50 gram force. The hardness depth profiles from the edges of samples were made at five different distances from the edge, with three points averaged at each distance. The bulk material hardness measurements were made by averaging six randomly placed indents. The measurements were made on either polished surfaces or surfaces ground to a minimum of 2000 grit wet grinding paper.

3.2 Results

In the following chapter the result obtained using the experimental methods described previously are presented. The acronyms used for different samples are presented in table 8.

Table 8: *Acronyms used for different samples*

AsB	**AsB SP**	**AsB HT**	**AsB HT SP**	**Ref SP**
Additively manufactured sample in as built condition	Additively manufactured sample shot peened after removal from build plate	Additively manufactured sample heat treated before removal from build plate	Additively manufactured sample heat treated before and shot peened after removal from build plate	Reference sample cut from sheet and shot peened

3.2.1 Surface XRD results

The initial XRD-results from the surfaces of the samples are presented in figure 28 through 32. In the figures, A-side with the AM samples means the top surface, i.e. the surface that was printed the last, and B-side the bottom surface, i.e. the surface that was attached to the support structure. With other samples, the naming is arbitrary, as both sides are identical. In the figures the results are named so that first the measurement

direction is given (0 or 90), followed by the sample number (1, 2 or 3). Note that there were only two AsB SP samples, and that, due to time limitations, only two Ref SP samples were measured. In addition, of the low-molybdenum reference samples only the center points were measured.

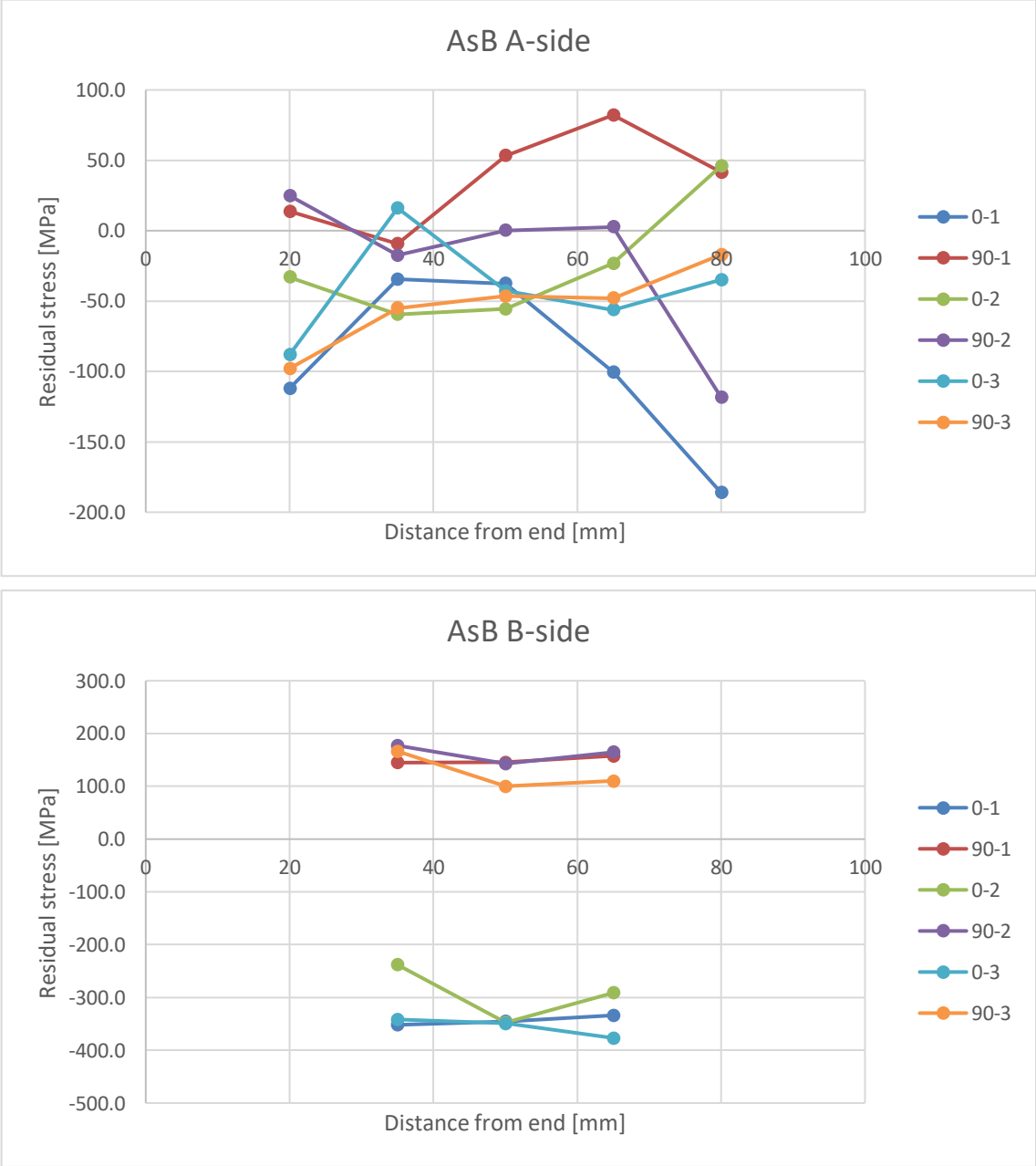

Figure 28 a) & b): *Residual stresses on the surfaces of the as built samples*

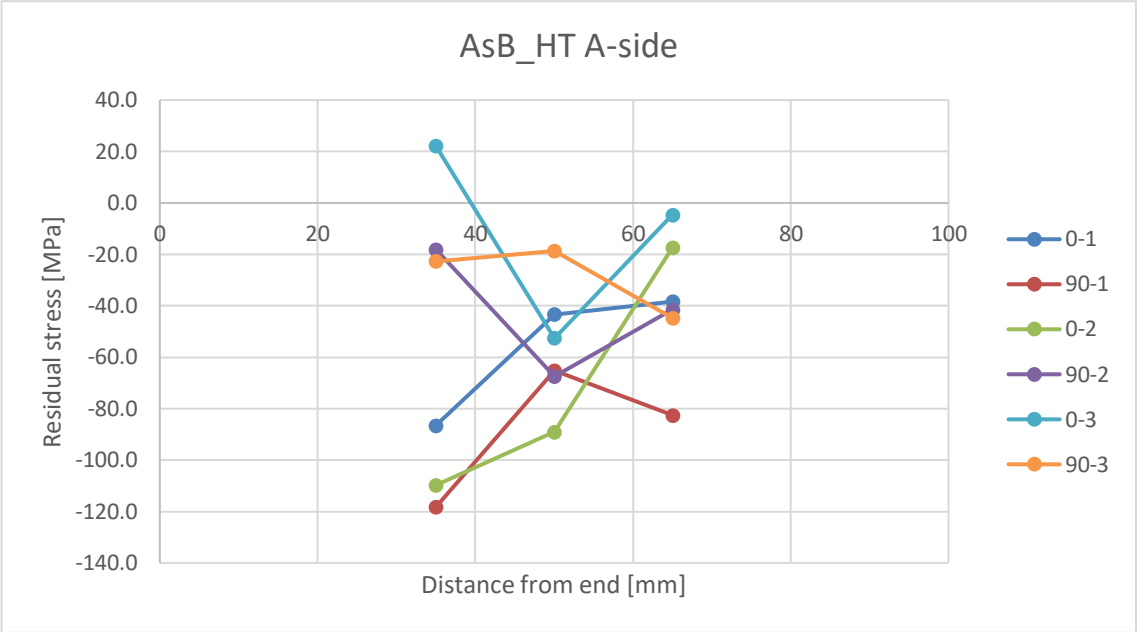

Figure 29 a) & b): *Residual stresses on the surfaces of the as built and heat treated samples*

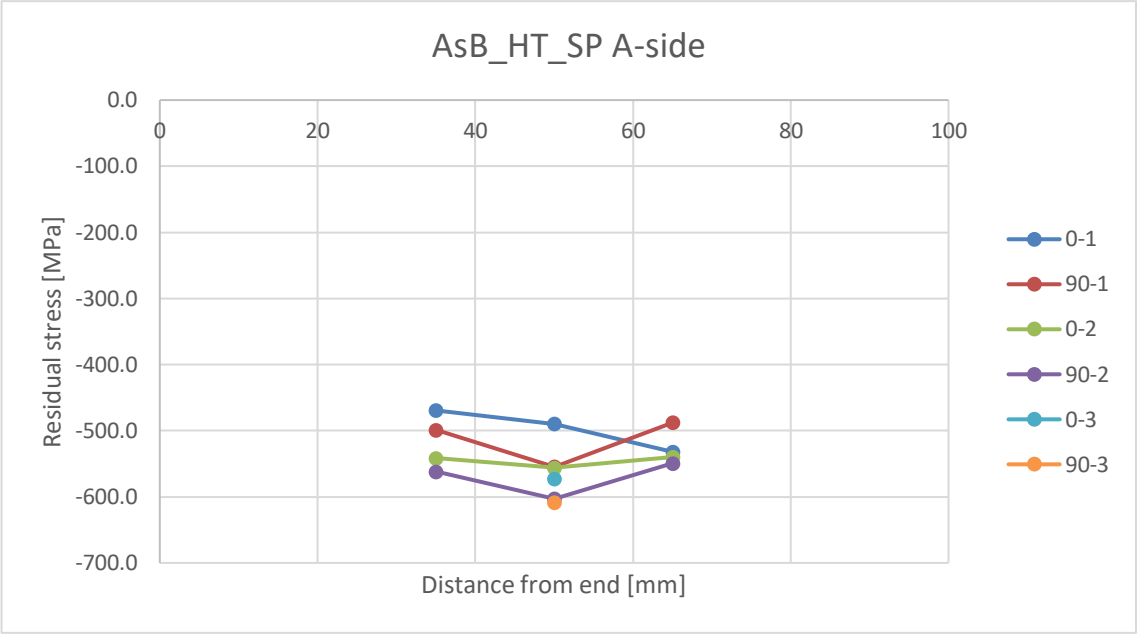

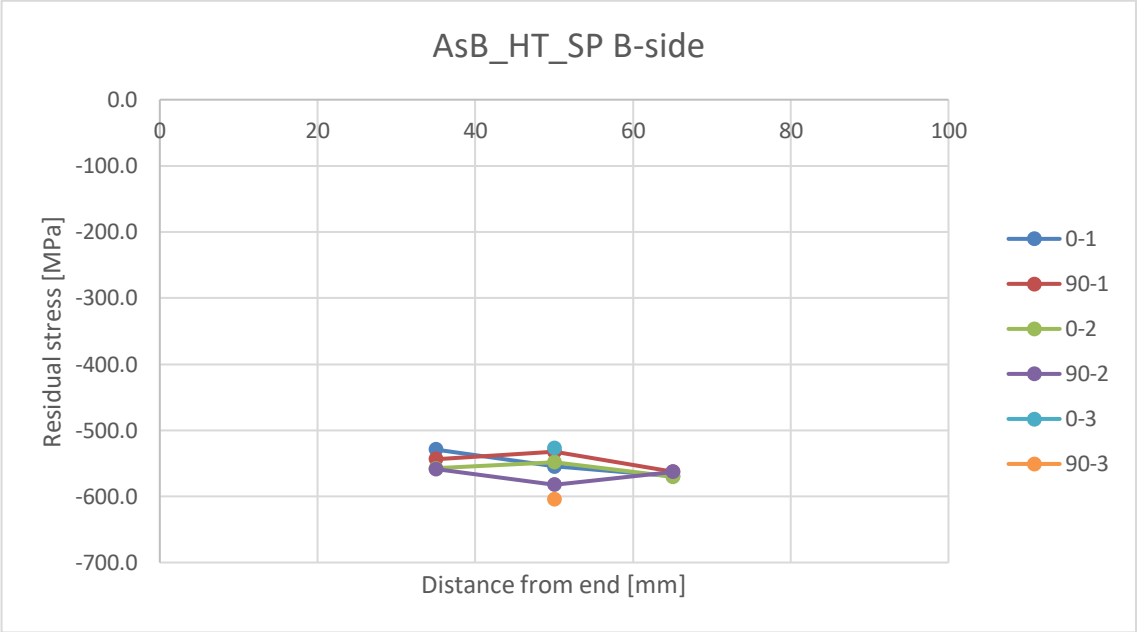

Figure 30 a) & b): *Residual stresses on the surfaces of the as built, heat treated and shot peened samples*

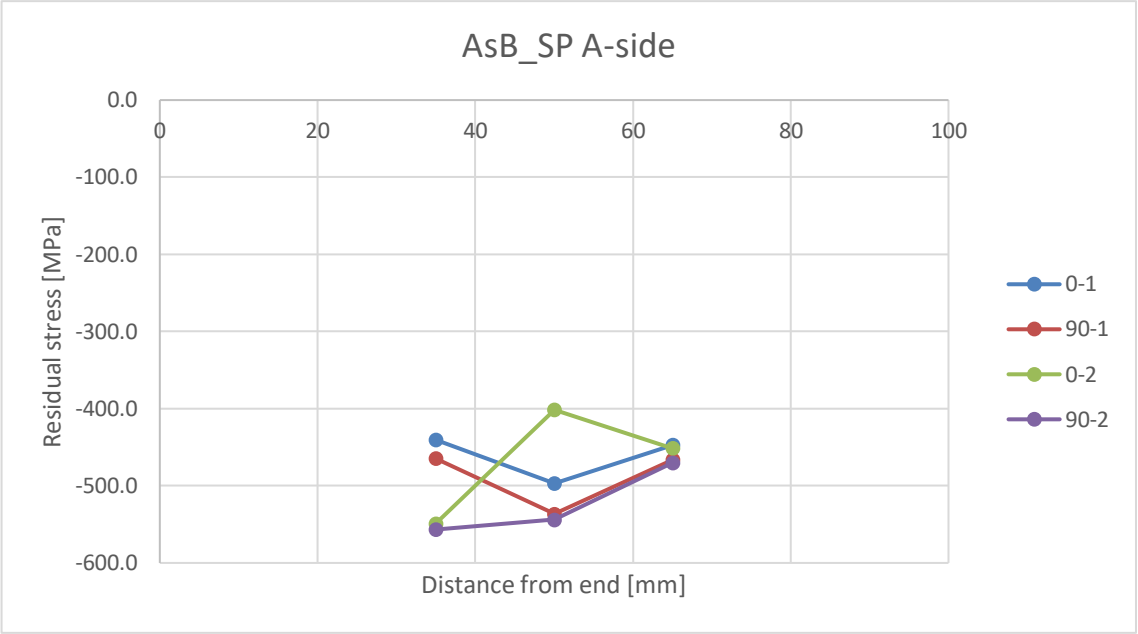

Figure 31 a) & b): *Residual stresses on the surfaces of the as built and shot peened samples*

Figure 32 a) & b): *Residual stresses on the surfaces of the shot peened reference samples*

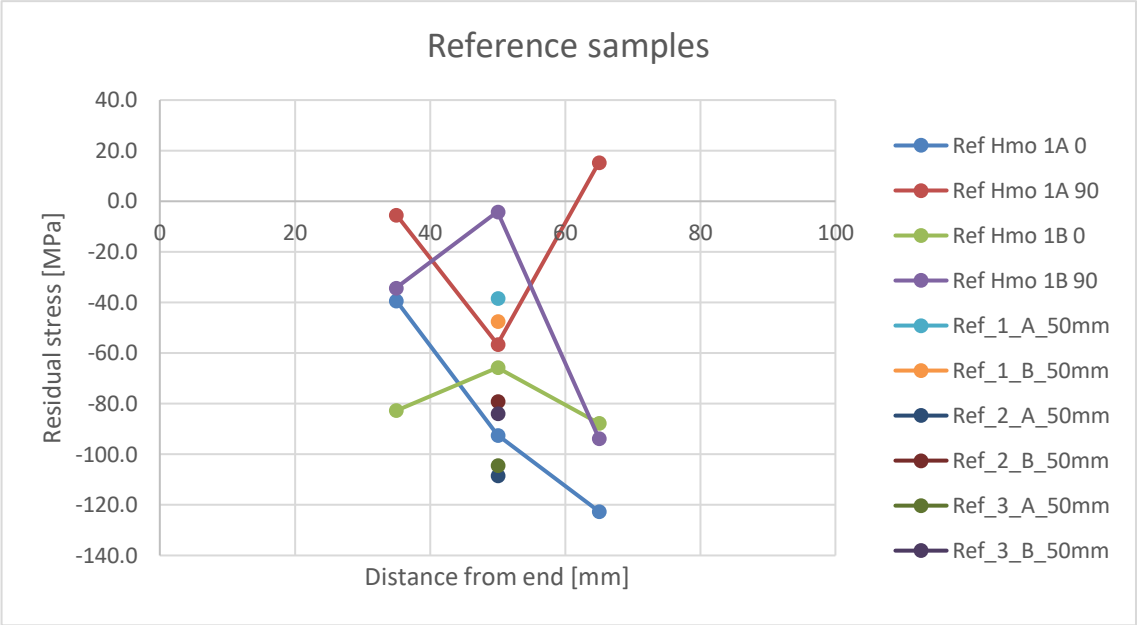

Figure 33: *Residual stresses on the surfaces of the reference samples*

Examples of diffraction peaks obtained from different samples are presented in figure 34.

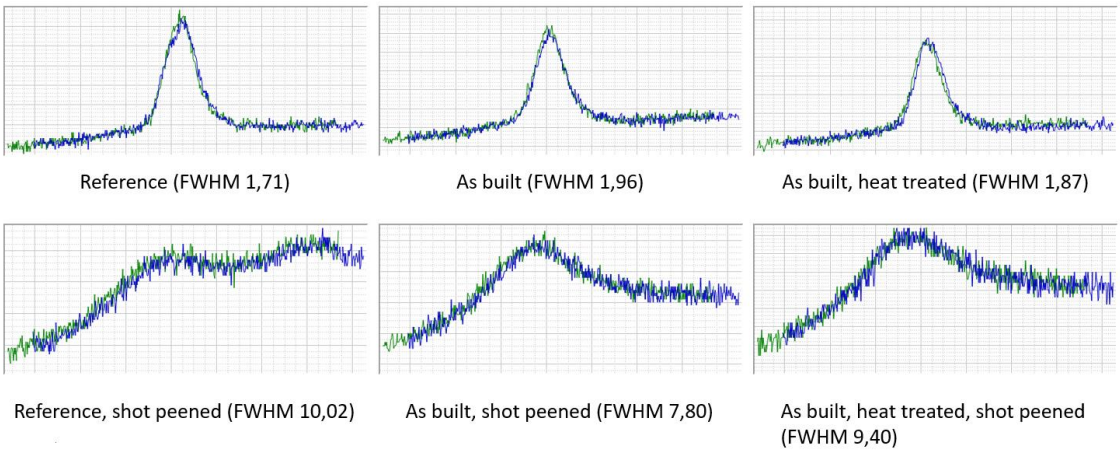

Figure 34: *Diffraction peaks obtained from different samples*

XRD-results from the surface of a welded reference sample are presented in figure 35.

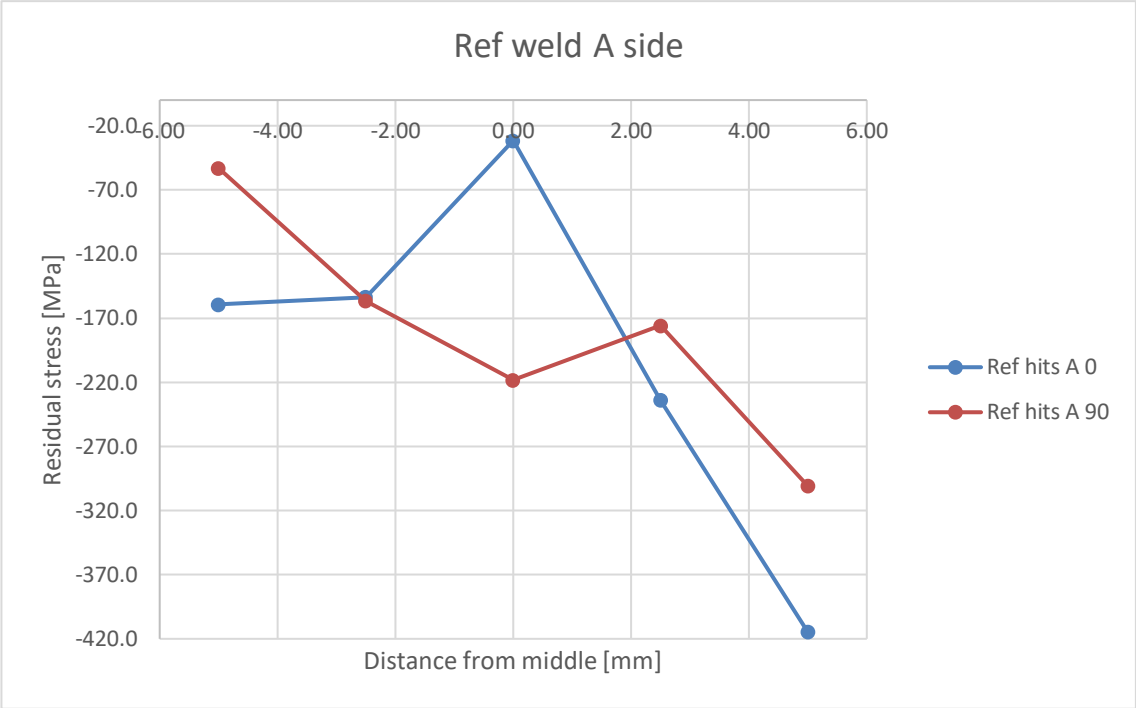

Figure 35: *RS profile measured from the surface of Ref weld 1A*

The deviations in the RS results given by the software for the surface XRD results are between less than ten and 40 MPa with the average being 22.7 MPa. There are two exceptions though. The deviations at the centre (0 mm) point of the Ref welded sample are 63.2 for the 0-direction and 123.1 for the 90-direction. If these two outliers are left out from the calculation, the average deviation drops to 21.9 MPa.

3.2.2 Residual stress depth profiles

The residual stress depth profiles from the B, or the bottom side of two as built samples and one heat treated sample are presented in figure 36. The 0-direction is along the longest dimension of the sample, and 90-direction is perpendicular to the longest dimension.

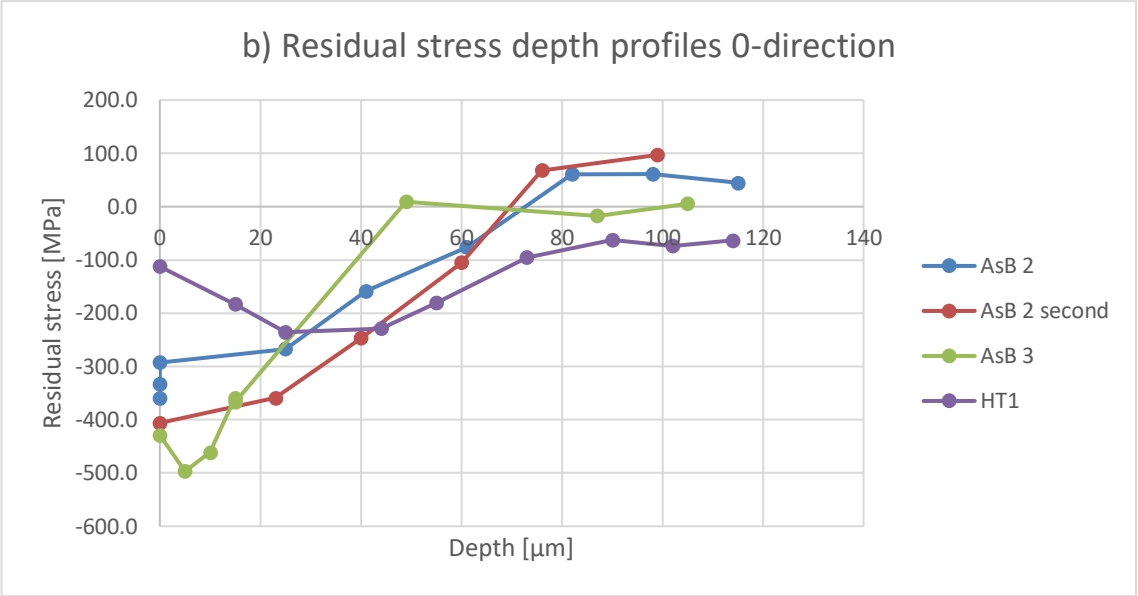

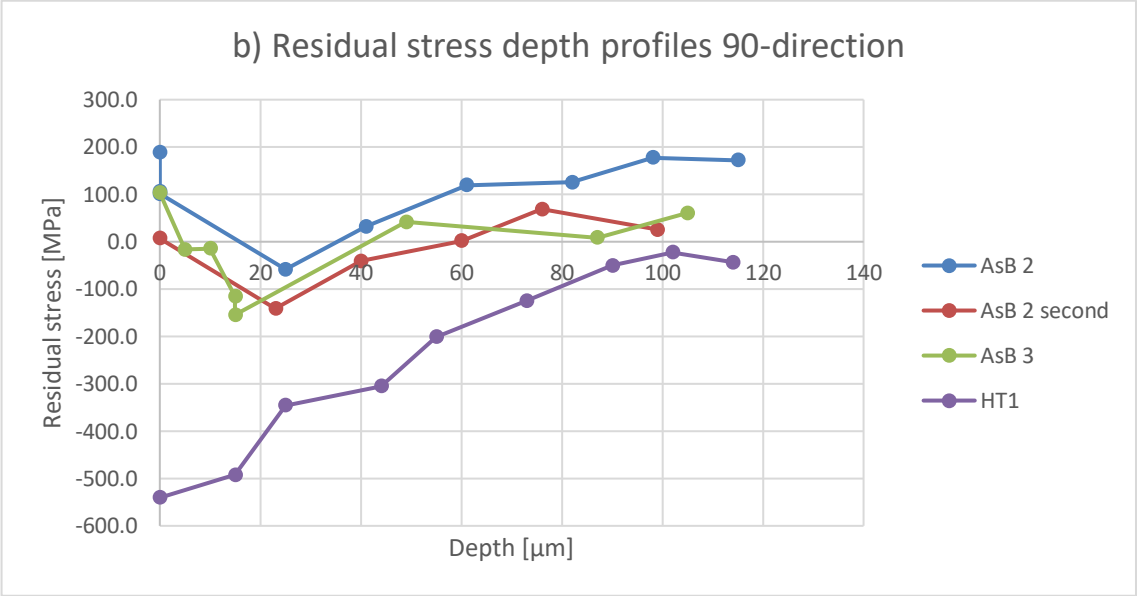

Figure 36 a) & b): *Residual stress depth profiles of the B-sides of two as built samples and one heat treated sample in 0 and 90 degree directions respectively*

The residual stress depth profile from the A or the top surface of one as built condition sample is presented in figure 37. 0-direction is along the longest dimension of the sample. A second profile is also presented, but measuring it was cut short, as the results indicated that the stress state had been relieved due to processing done to the sample between the two measurements.

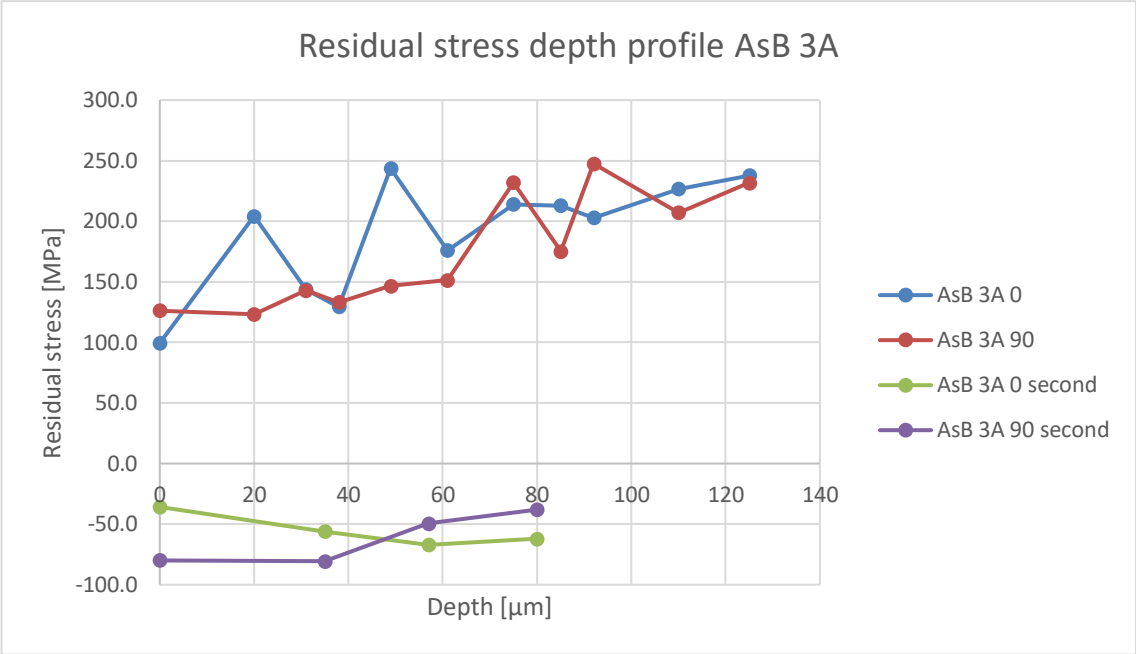

Figure 37: *Residual stress depth profiles of the top surface of an as built condition sample*

Residual stress depth profiles from two reference samples and one AM sample are presented in figure 38. 0-direction is along the longest dimension of the sample.

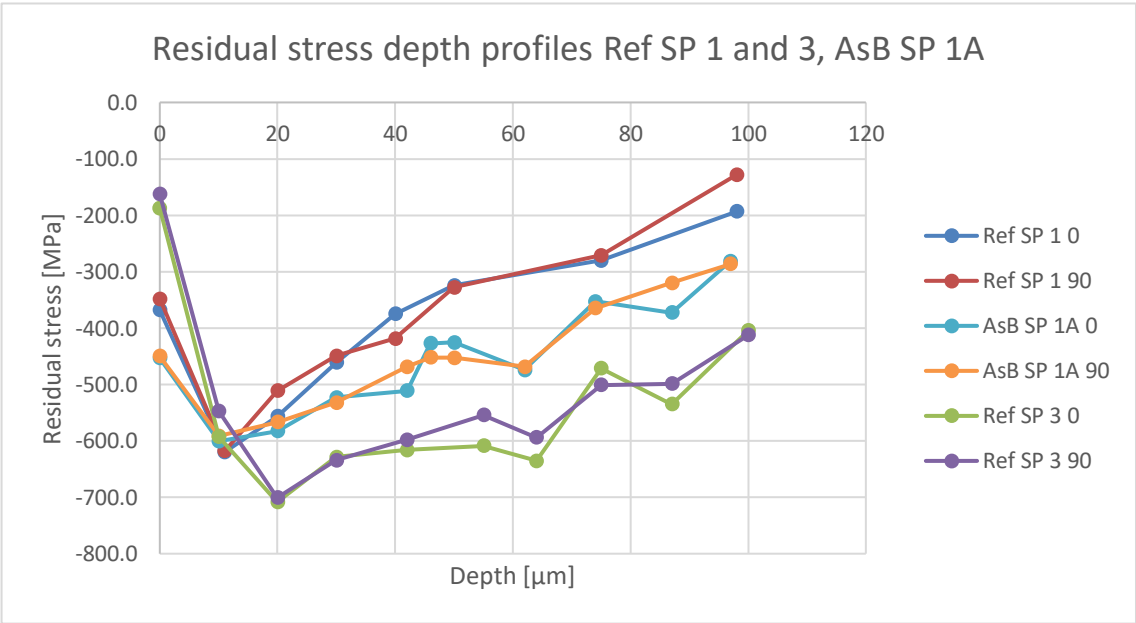

Figure 38: *Residual stress depth profiles of two shot peened reference samples and one shot peened AM sample*

The deviations given by the software for the RS depth profile results are between less than ten and 45 MPa with one exception being a point measured from Ref SP 1 at 75 µm below the surface in the 90-direction, which has a deviation of 64.8 MPa. Average

deviation from all of the RS depth results is 23.7 MPa. No trend could be observed from the deviations.

3.2.3 Corrosion tests

The XRD results measured from the samples tensioned with the strain gages are presented in table 9. The measured stress values are averages of three different points measured along the area of uniform tension between the two inner rollers. The stress values were measured in the 0-direction or parallel to the longest dimension of the sample. The values for the welded sample were measured from base material, not from the weld.

Table 9: *Residual stresses measured from the corrosion test samples after being tensioned using strain gages*

Sample	**Ref 1A**	**Ref weld 1A**	**AsB 1A**	**AsB HT 2A**
Required stress [MPa]	180	180	350	180
Measured stress (XRD) [MPa]	115	-119	151	52

Selected images of the cross sections after the first corrosion test are presented in figures 39 through 42.

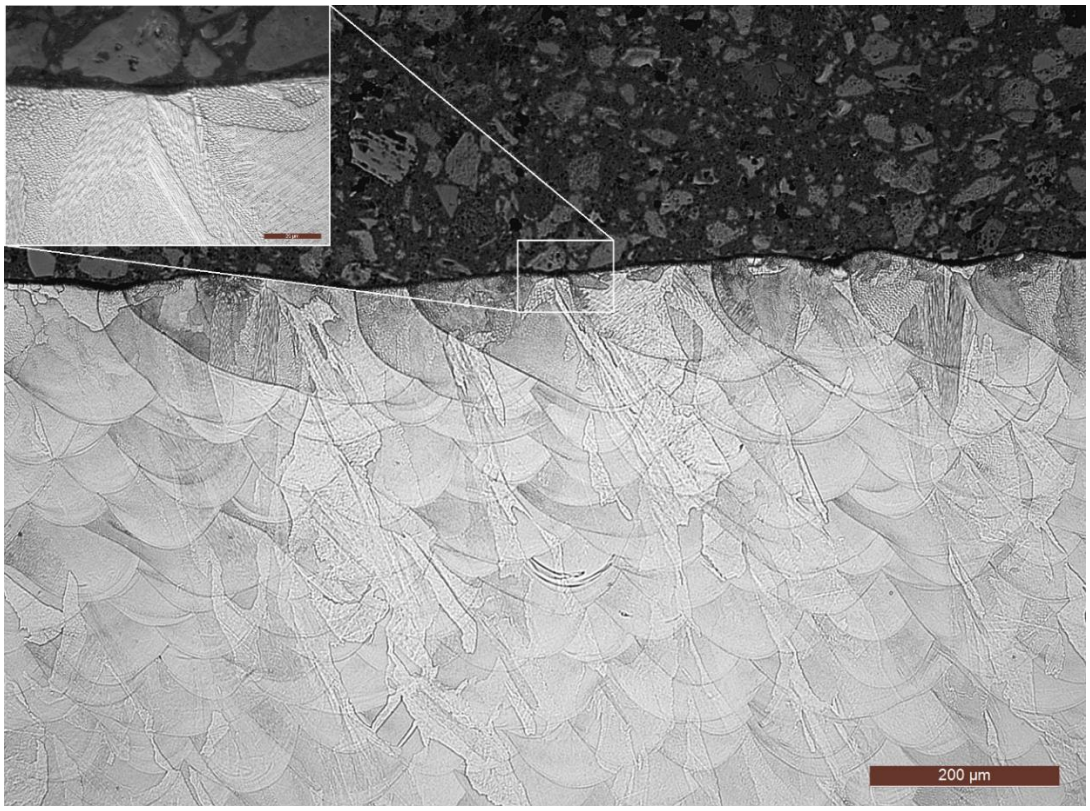

Figure 39: *10x magnified optical micrograph of the as built material after the first corrosion test; the inset is at 100x magnification*

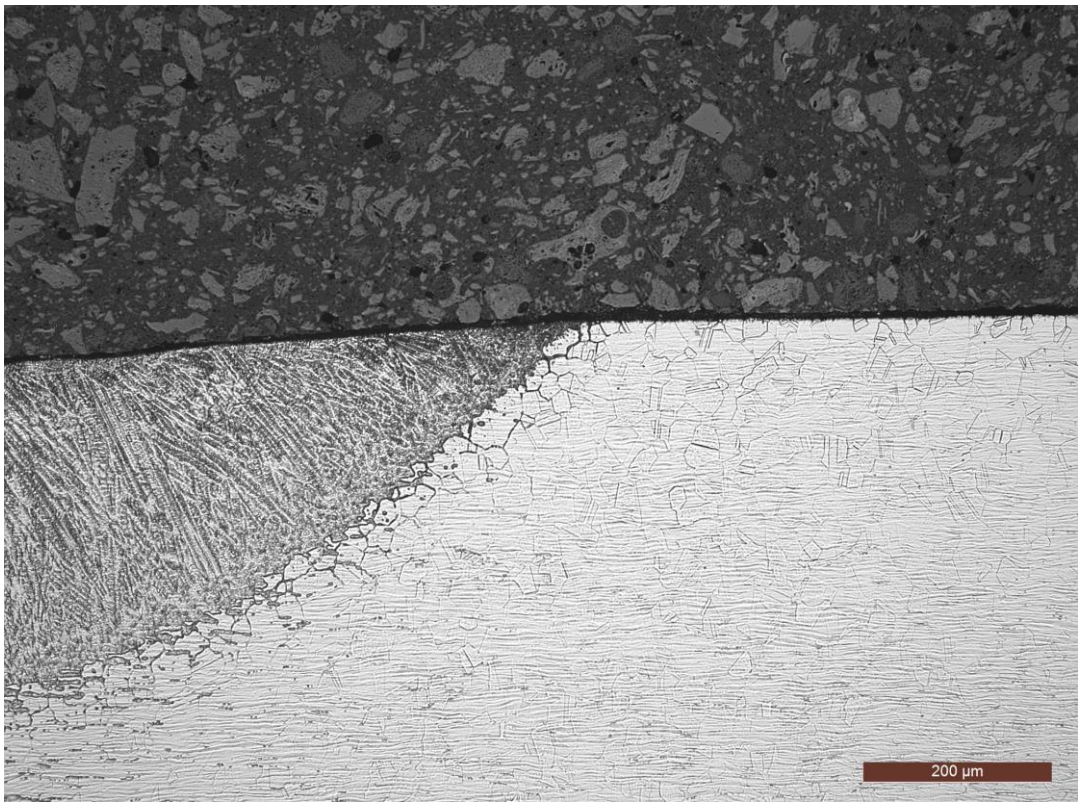

Figure 40: *10x magnified optical micrograph of the welded sample, showing the edge of the weldment after the first corrosion test*

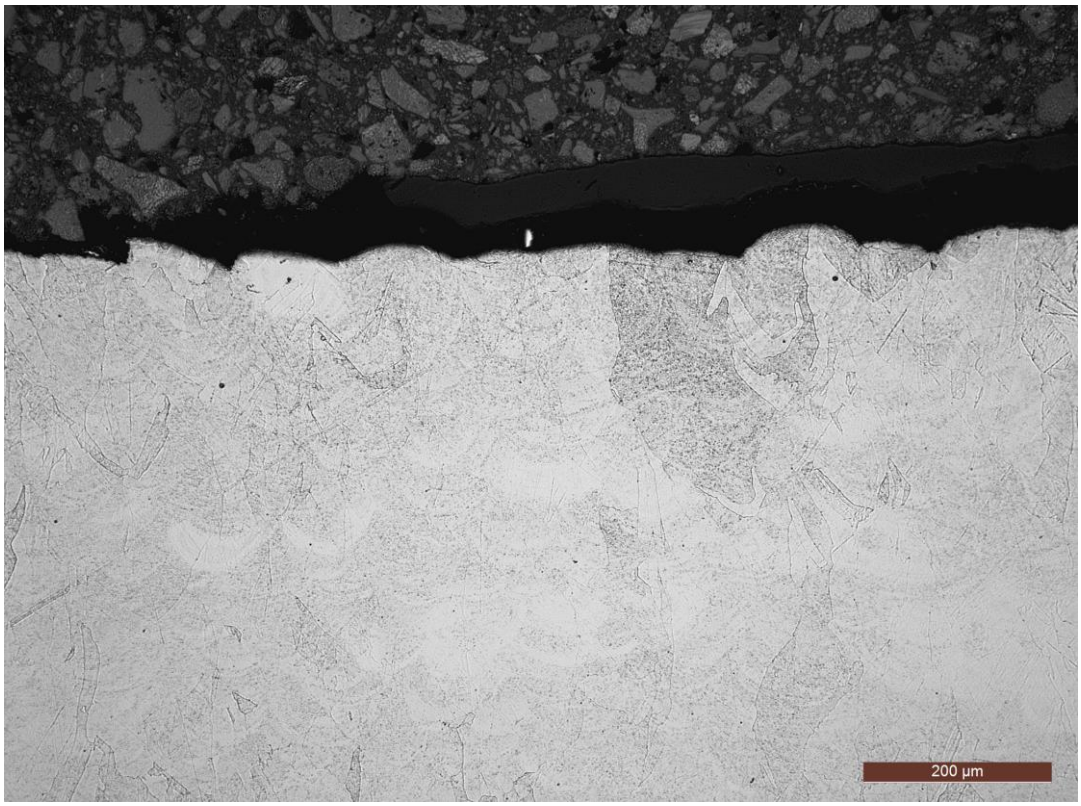

Figure 41: *10x magnified optical micrograph of the as built and heat treated material after the first corrosion test*

Figure 42: *10x magnified optical micrograph of the reference material after the first corrosion test; the inset is at 100x magnification*

The images from the second set of samples are omitted, as the samples were identical to the ones from the first test.

3.2.4 Metallography

Optical micrographs of as built and as built heat-treated samples are presented in figures 43 through 45.

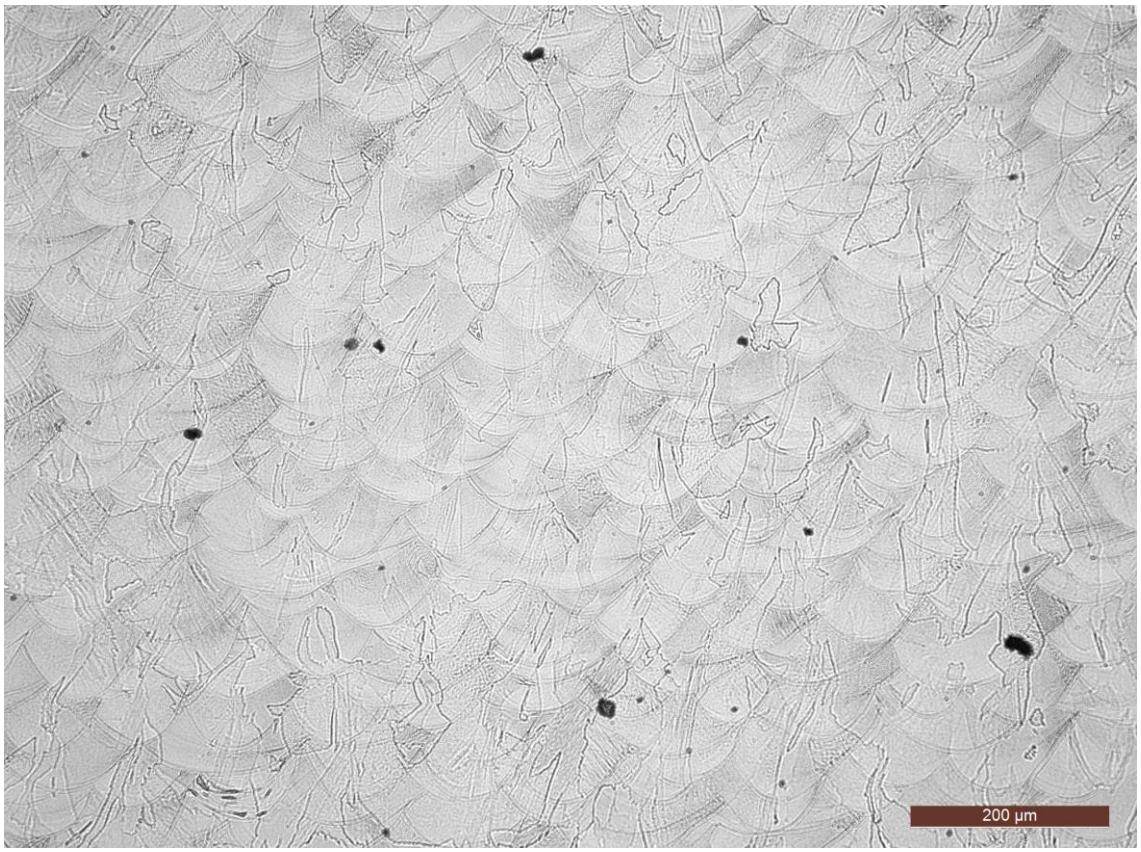

Figure 43: *Optical micrograph of the as built sample in y-direction at 10x magnification, build direction is toward the top of the image*

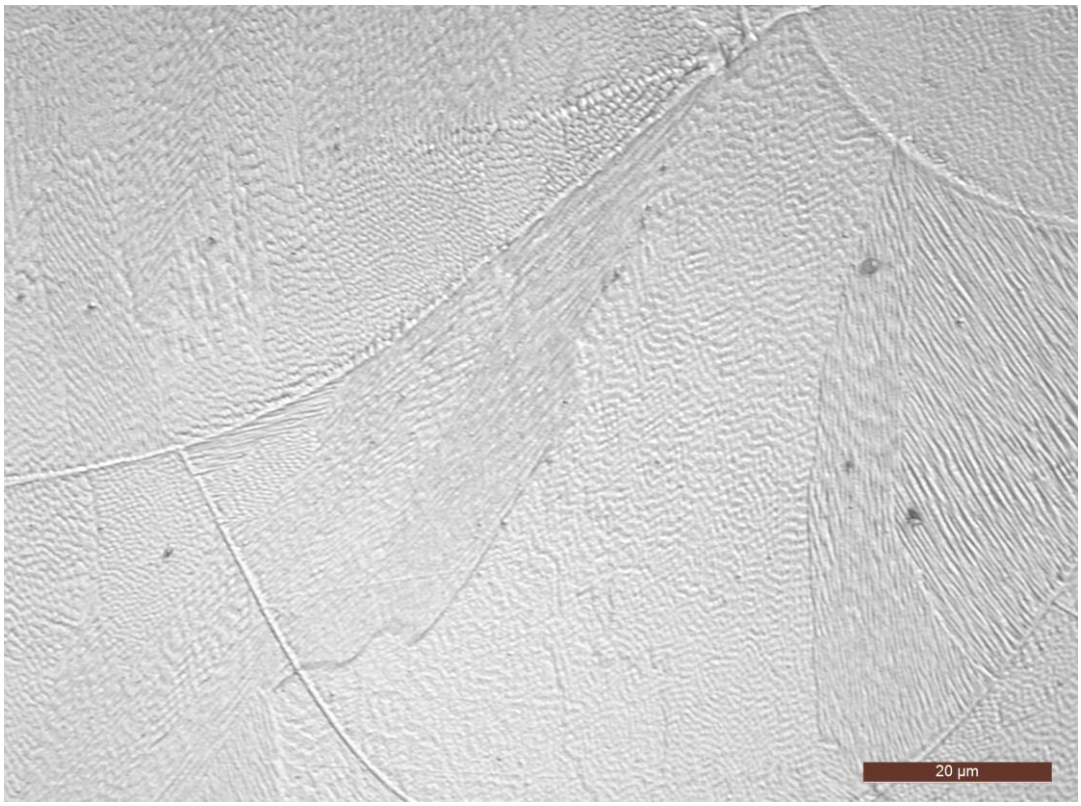

Figure 44: *Optical micrograph of the as built sample in y-direction at 100x magnification, build direction is toward the top of the image*

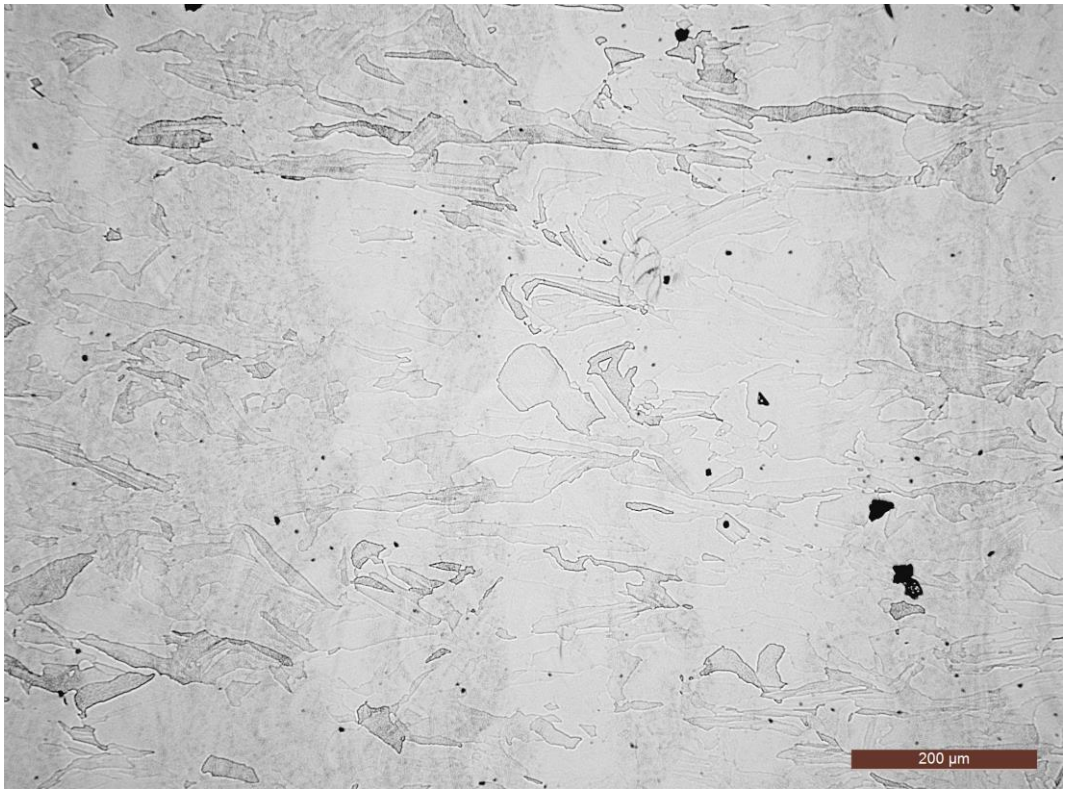

Figure 45: *Optical micrograph of the heat-treated sample in x-direction at 10x magnification*

A scanning electron microscope (SEM) secondary electron (SE) image of the as built sample is presented in figure 46.

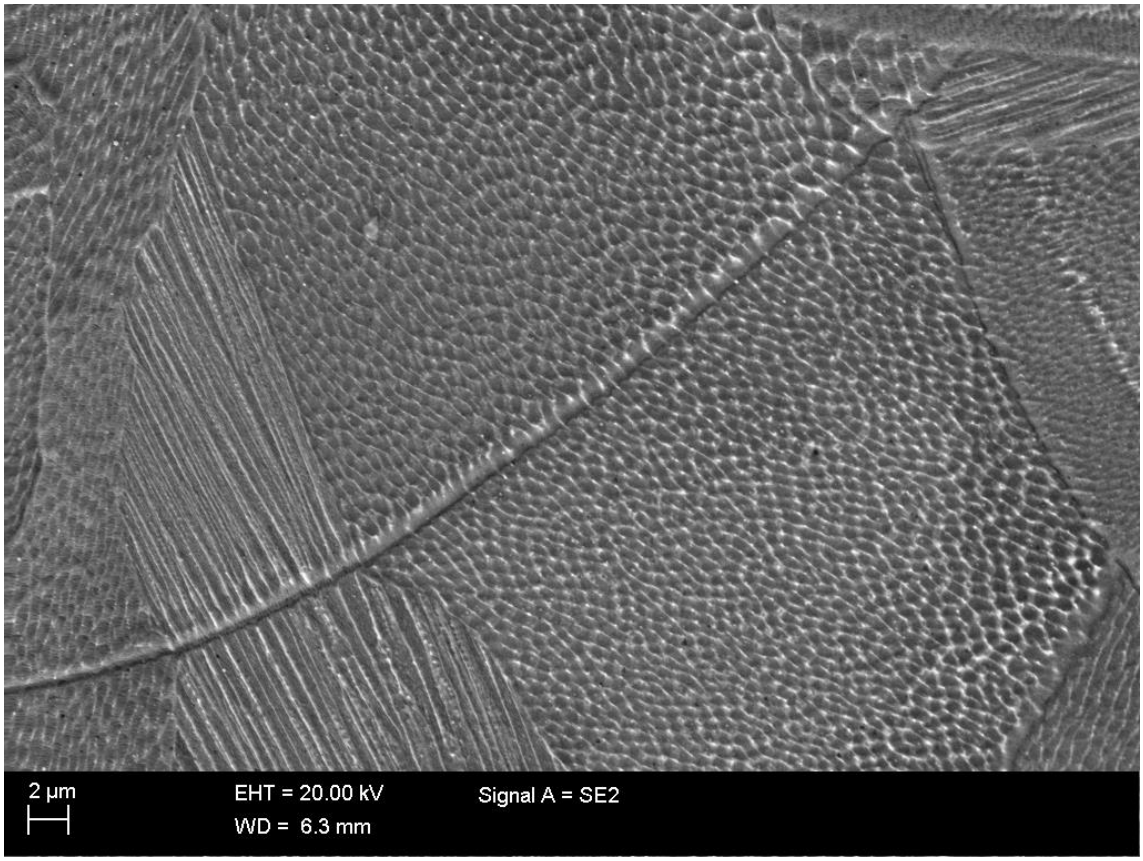

Figure 46: *Secondary electron image of the as built sample*

Optical micrographs of the edges of different samples after shot peening are presented in figures 47 through 49.

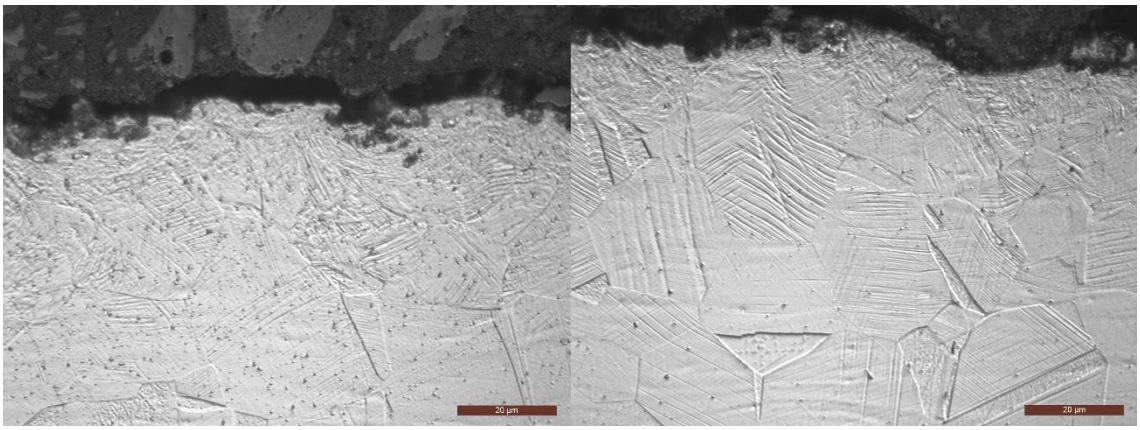

Figure 47: *Optical micrographs of reference material after being shot peened three times*

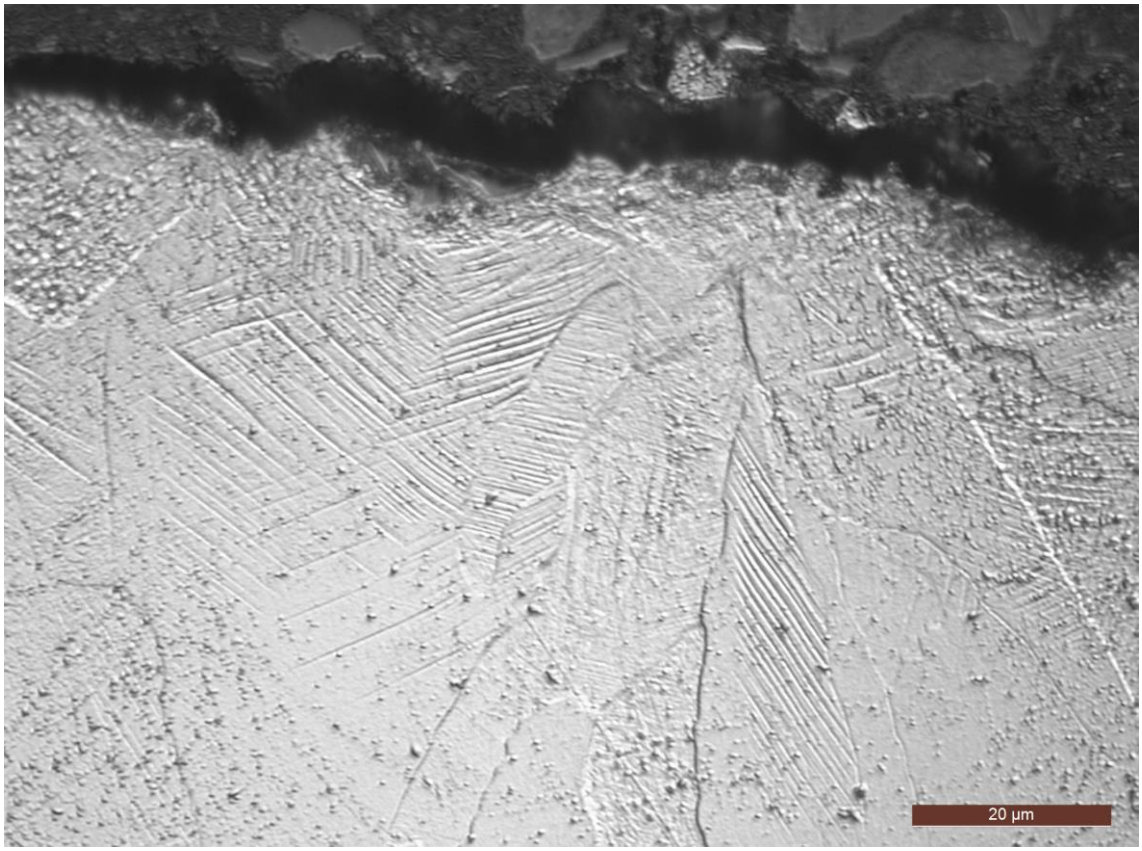

Figure 48: *Edge of a heat treated AM sample after being shot peened three times*

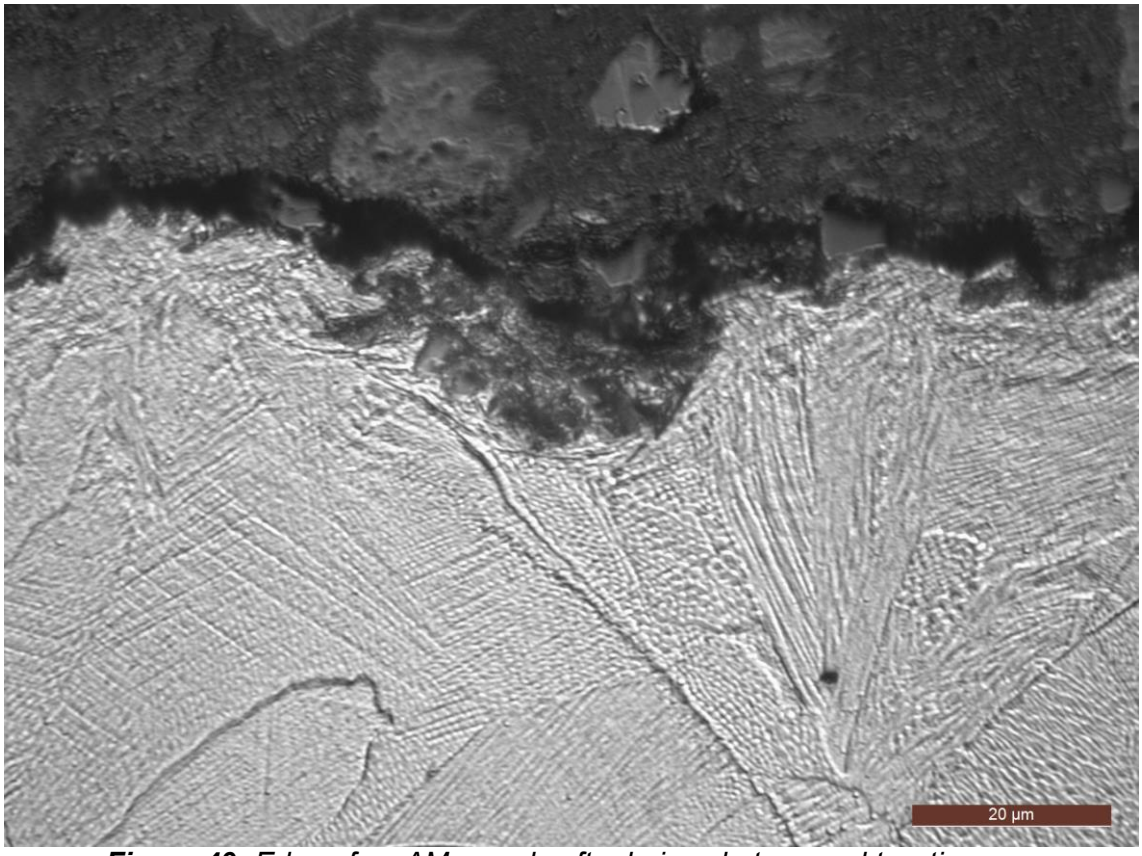

Figure 49: *Edge of an AM sample after being shot peened two times*

SE images of the edge of reference material after being shot peened once are presented in figure 50. The two images are from the same edge of the sample, taken a few millimeters apart.

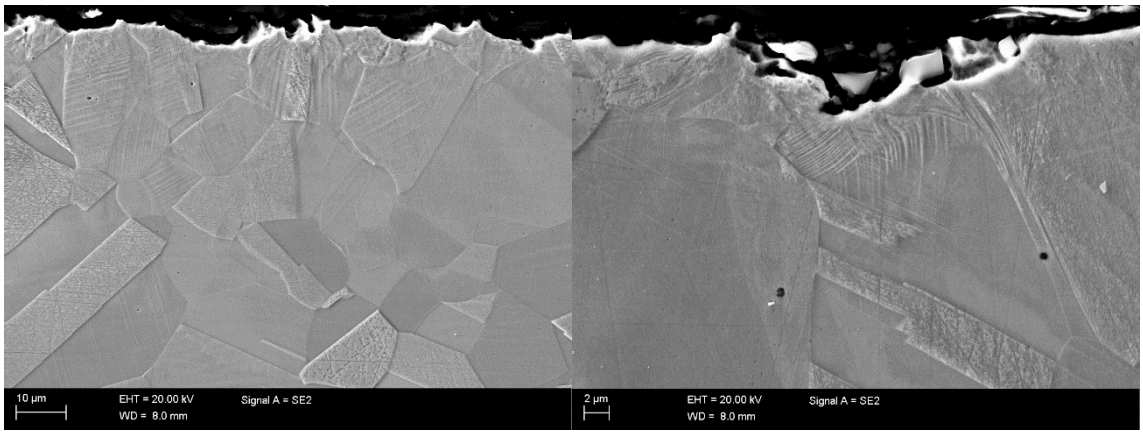

Figure 50: *SE images of the edge of reference material after being shot peened once*

3.2.5 Hardness measurements

An example of the hardness measurement points is presented in figure 51.

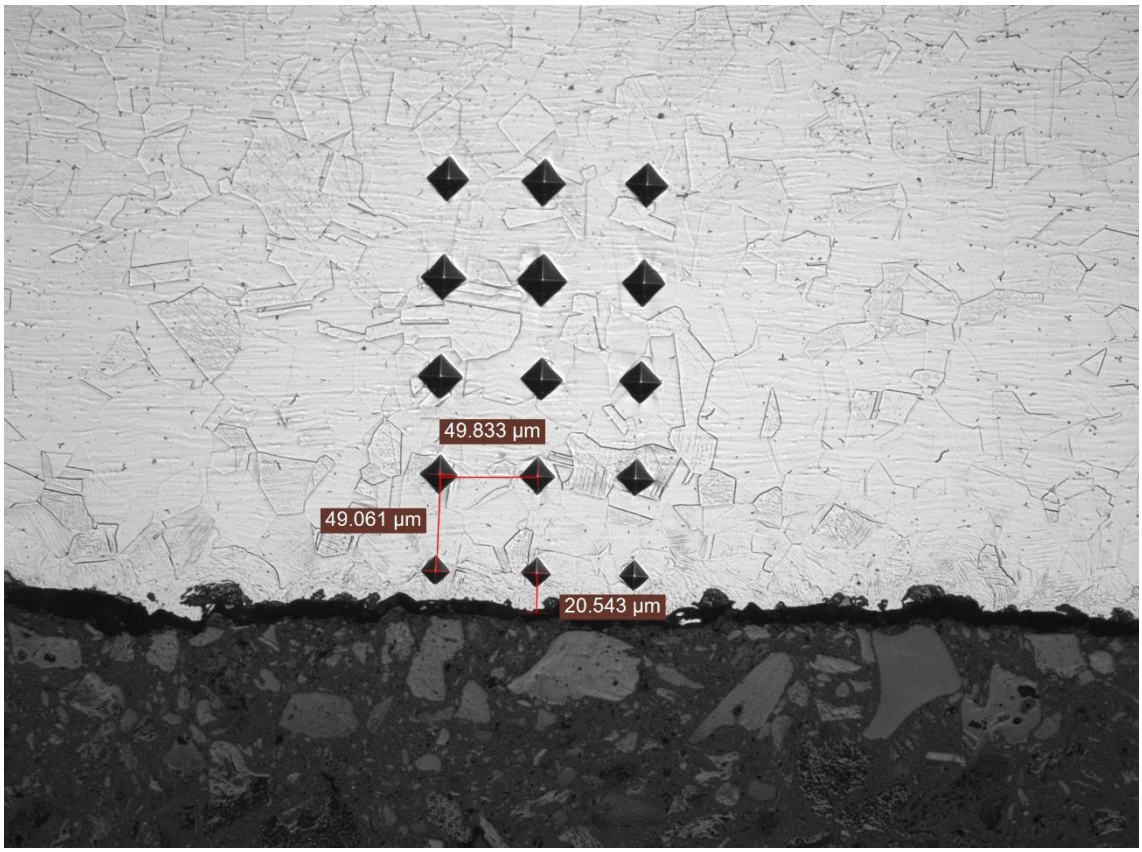

Figure 51: *An example of the hardness measurement points on Ref SP 3 sample*

The hardness depth profiles made from the shot peened samples are presented in figure 52.

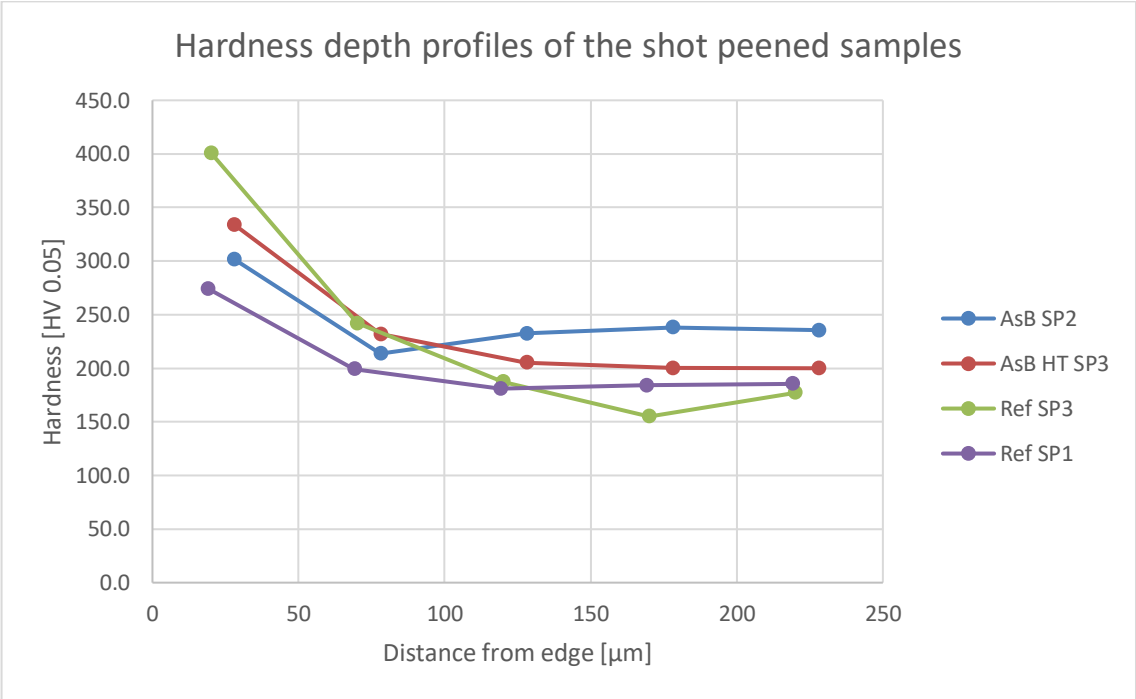

Figure 52: *Hardness depth profiles of the shot peened samples*

Hardness depth profiles comparing two AM samples is presented in figure 53. AsB SP 2 is and AM sample shot peened twice and AsB 3A is the top surface of an AM sample in as-built condition.

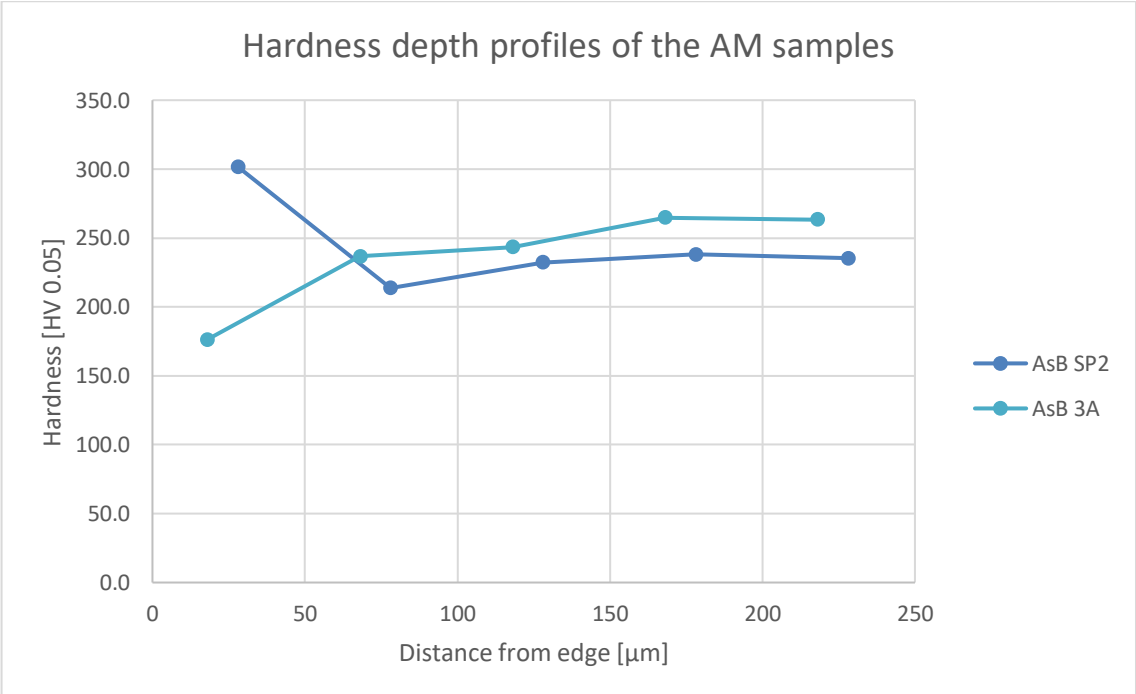

Figure 53: *Hardness depth profiles of two AM samples*

Average hardness values of the bulk materials of selected samples are presented in table 10.

Table 10: *Average hardness values of the bulk material of selected samples*

	Ref low Mo	Ref high Mo	AsB	AsB HT
Average hardness [HV0.05]	168	179	227	195

3.3 Rapid mixing nozzles

In this chapter, the experiments performed on and the results obtained from the rapid mixing nozzle will be presented.

3.3.1 Methods and materials of the rapid mixing nozzle studies

Three additively manufactured rapid mixing nozzles were delivered by Outotec. They are made from 316L stainless steel. The exact quality of the steel, whether it is low or high molybdenum, is not known, though it may be assumed the manufacturer, SLM Solutions Group AG, would use their own steel powder. The material data sheet provided by SLM on their website states, that the material is EN 1.4404, i.e. the low molybdenum variant. Yet the datasheet also claims that the molybdenum content varies from 2 % to 3 %. [94] One of the nozzles with the printing direction annotated is presented in figure 54.

Figure 54: *One of the rapid mixing nozzles with the print direction annotated*

The processing history of the components is not exactly known. They were manufactured by SLM Solutions Group AG using L-PBF technique, after which two of them were most likely ball milled, judging by the ceramic particle that fell out of one of them. The remaining one was most likely shot peened, as its surface quality closely represents that of the shot peened strips studied earlier. A series of images of one of the nozzles is presented in figure 55.

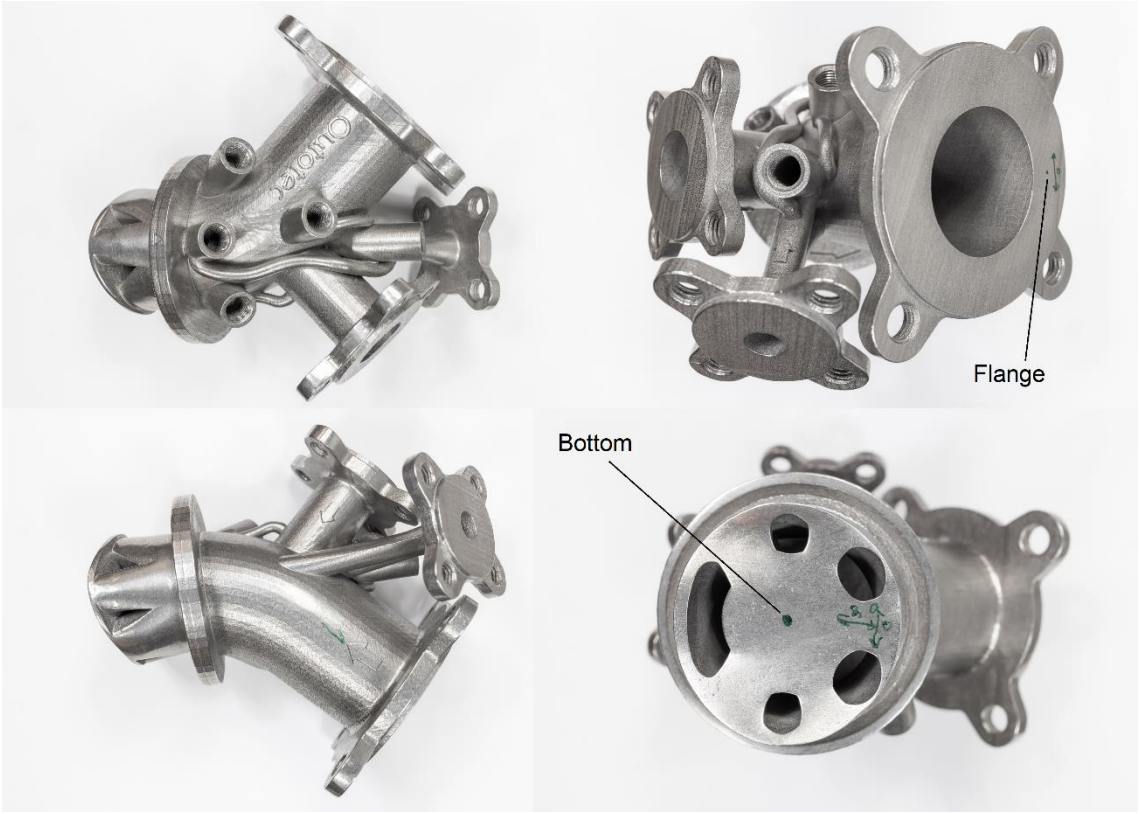

Figure 55: *One of the rapid mixing nozzles showing the two XRD-measurement points at the bottom and at the largest flange*

Initially, residual stress measurements were made from two points on each nozzle. Based on these results it was decided that nozzle 2, one of the ball milled ones, would be subjected to more characterization. Only one of the nozzles could be damaged, as per Outotec's instructions, so only one could be studied further.

Two residual stress profiles were measured from one of the flanges on the nozzle. First profile was made with the nozzle still intact. For the second profile the flange was cut from the nozzle, 20 mm below the flange. After the second profile was measured the flange and 20 mm piece of tube was cut so that RS depth profiles could be measured from the inside surfaces of the tube. Two profiles were measured, one from the top surface of the tube and one from the bottom, with respect to the printing orientation of the nozzle. The measurement points can be seen in figure 56.

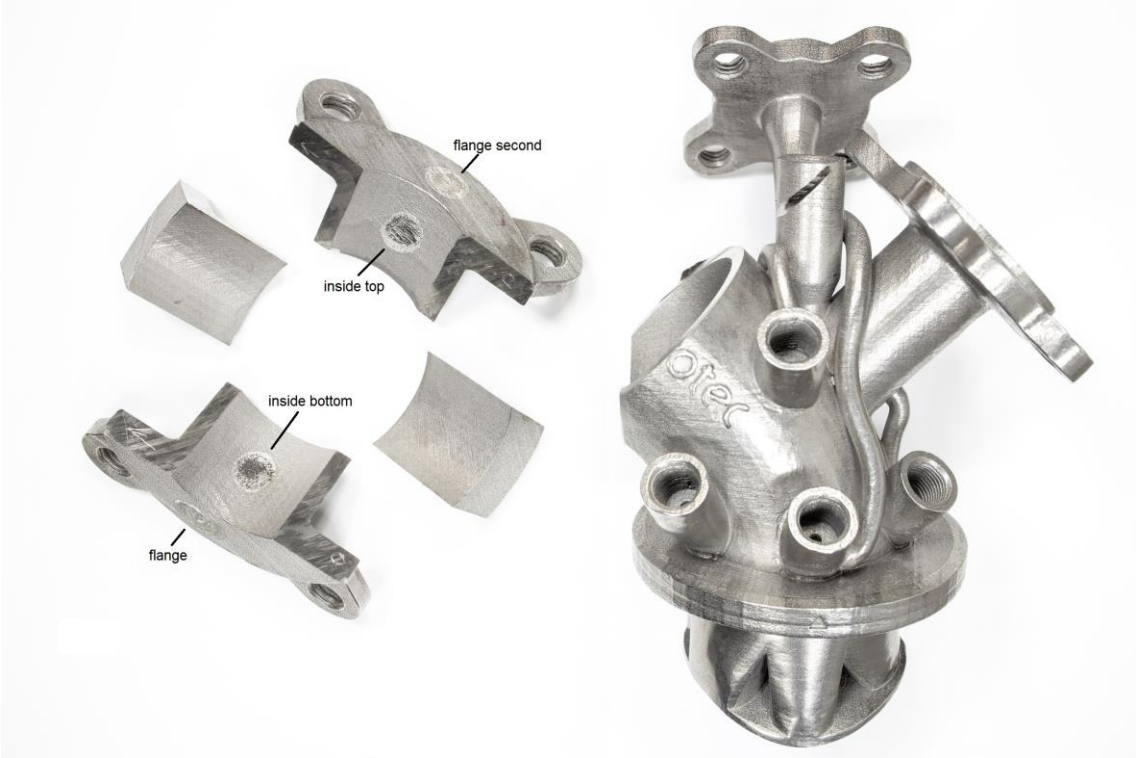

Figure 56: *Residual stress depth profile measurement points on nozzle 2*

To characterize the microstructure of the nozzle material, a piece was cut from the previously cut tube's wall. This piece was further sectioned to two pieces, which were then mounted in phenolic resin, ground, polished and etched using the same parameters that were used to etch the previous samples.

3.3.2 Results

The residual stresses from the initial XRD measurements are presented in table 11.

Table 11: *Residual stress values from the initial XRD measurements from the rapid mixing nozzles*

	Nozzle 1	Nozzle 2	Nozzle 3
Bottom [MPa]	-425	-407	-580
Flange [MPa]	-350	-330	-548

The values are calculated as the averages of the 0 and 90 directions.

Examples of the diffraction peaks obtained from the flanges of the nozzles are presented in figure 57.

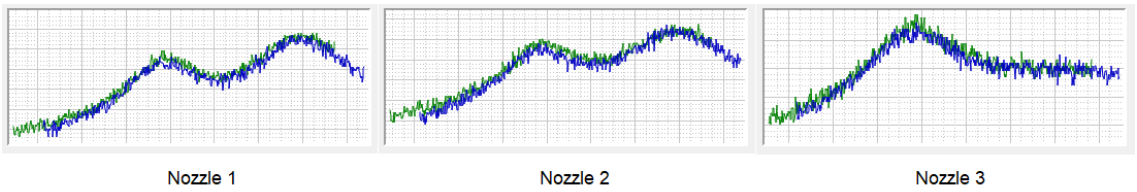

Figure 57: *Examples of the diffraction peaks from different nozzles*

The FWHM values of the samples were quite similar, between 8.5 and 9.5 degrees. The values from nozzle 3 were at the low end, though its error bars, given by the software were the highest at 1.7 degrees, while other samples' bars were around 0.7 degrees.

Two residual stress depth profiles measured from one of the flanges of a rapid mixing nozzle are presented in figure 58.

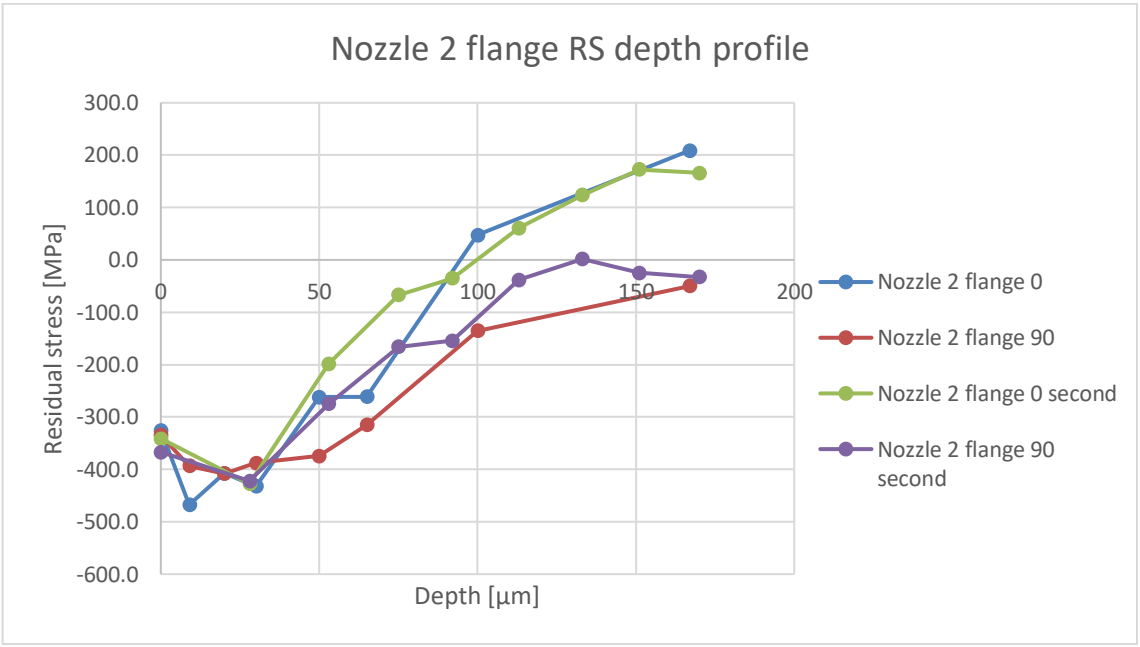

Figure 58: *Residual stress depth profiles from a flange of nozzle 2*

Two residual stress depth profiles measured from inside surfaces of a rapid mixing nozzle are presented in figure 59.

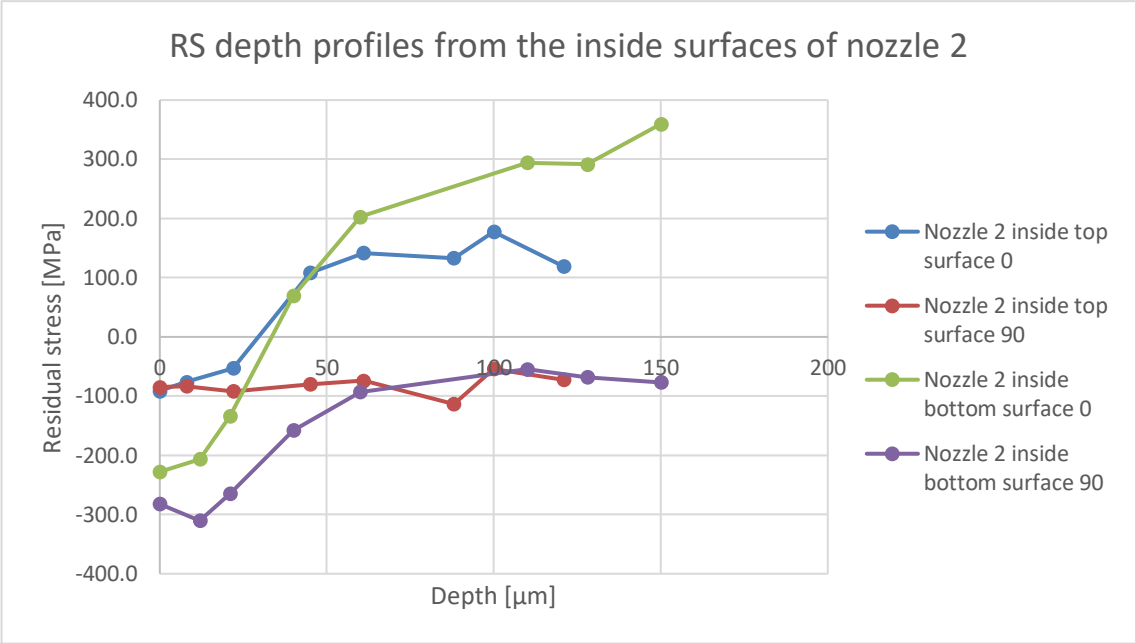

Figure 59: *Residual stress depth profiles from inside surfaces of nozzle 2*

The deviations from the surface and RS depth profile results are between less than ten and 35 MPa with the averages being 16.5 MPa and 19.1 MPa respectively. No trend is visible in the RS depth profile deviations.

The micrographs of one of the pieces are presented in figures 60 and 61.

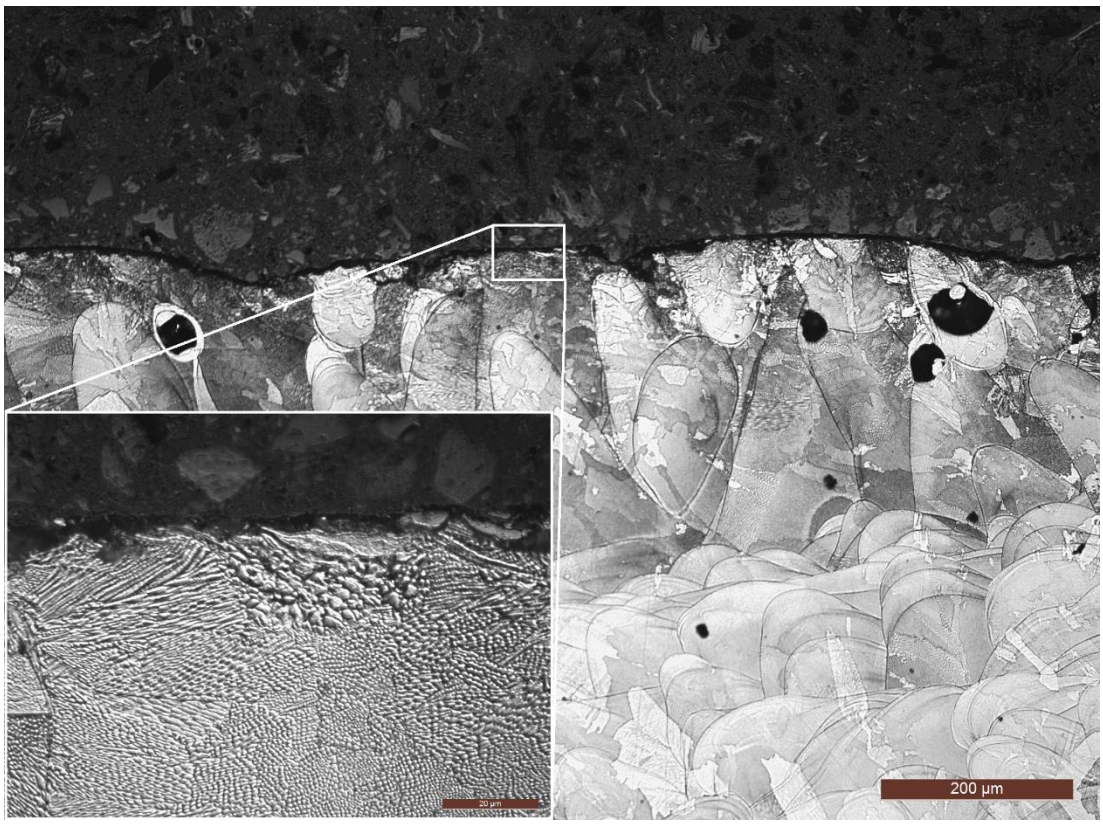

Figure 60: *Micrograph of the cross section of the tube wall, showing the outside surface; main image at 10x, inset at 100x*

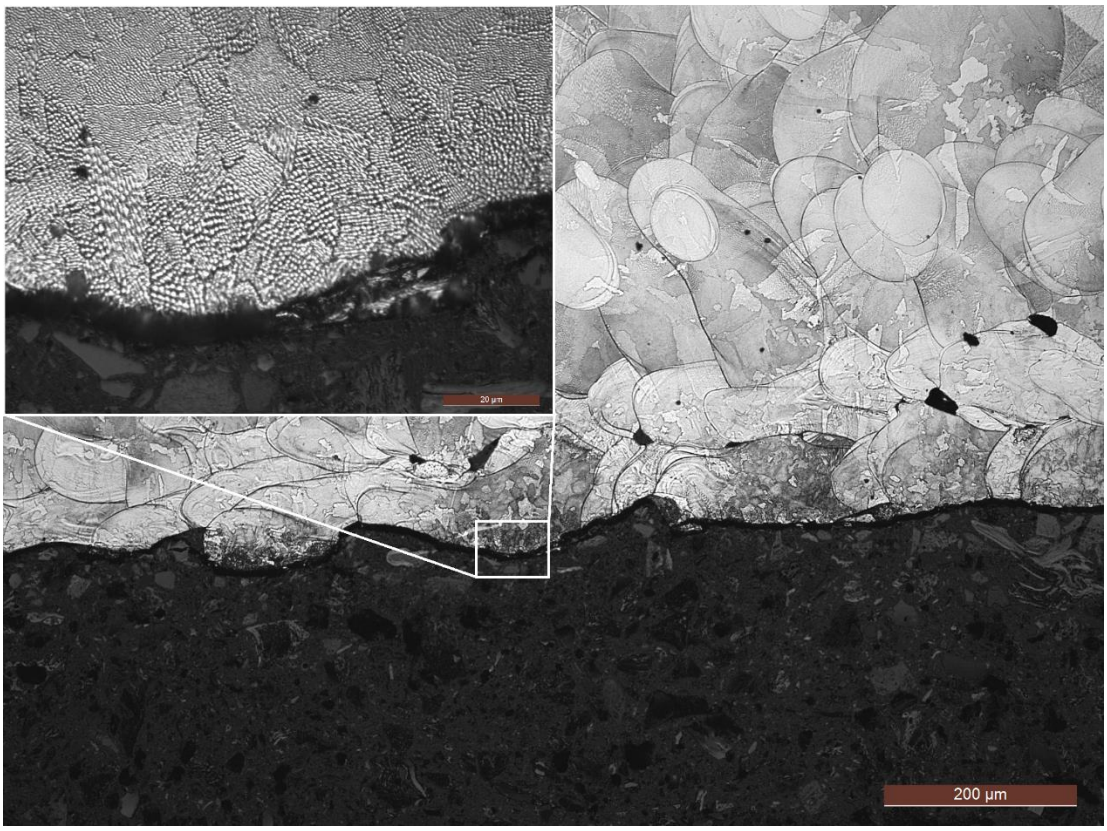

Figure 61: *Micrograph of the cross section of the tube wall, showing the inside surface; main image at 10x, inset at 100x*

4. DISCUSSION

In the next chapters, the results of the experimental studies will be discussed.

4.1 Surface XRD results

The initial XRD results from the top surfaces of the AsB samples are quite similar to what Ghasri-Khouzani et al. [61] reported with 5 mm thick disks after being removed from the build plate. Their results seem to centre around 0 MPa (no averages were given for their results), while the ones obtained here have an overall average value of -33 MPa with a standard deviation averaged between the samples of 39 MPa.

Comparing the results from the AsB samples to the ones from AsB HT samples, the stress state is, somewhat unexpectedly, slightly more compressive. The overall average stress on the top surfaces of the AsB HT samples is -50 MPa with a standard deviation averaged between the samples of 24 MPa. The stress state here was expected to be lower, as the samples were heat-treated, and should therefore be stress free.

The stress states on the top surfaces of the AsB and AsB HT could be offset to a more compressive value by a systematic error, as their stress states are in an expected relation to each other, with the heat-treated samples having a more compressive stress state than the AsB ones. A systematic error seems unlikely though, as these results were obtained over several days, with other users and several calibrations performed on the XRD in between measurements. Measuring over several days, with other users in between can lead to random errors, of course. These errors could arise from measurement device setup, like the placing of the detectors, and from an acceptable but still slightly different calibration between measurement sessions.

With the AsB and AsB HT samples the stresses on the B-side or the side facing the build plate, the stresses are clearly directed along the 0-direction in the AsB samples and along the 90-direction in the AsB HT samples. This was deduced to be due to the band sawing used to remove the samples from the build plate. The difference in the direction of stresses between the samples can be explained by either different orientation on the build plate, or different orientation during sawing. The AsB samples were sawed off first. Then the plate with the rest of the samples was sent to be heat treated, and the AsB HT samples were sawed off only after heat treatment. It is possible that the build plate was

installed in the band saw in a different orientation or that the samples were printed in a different orientation. Either way, the AsB HT samples were cut in a different orientation than the AsB samples, leading to a differing stress state on the bottom surface of the samples. This fact is further illustrated in figure 62, where the different directions of the cutting marks can be seen.

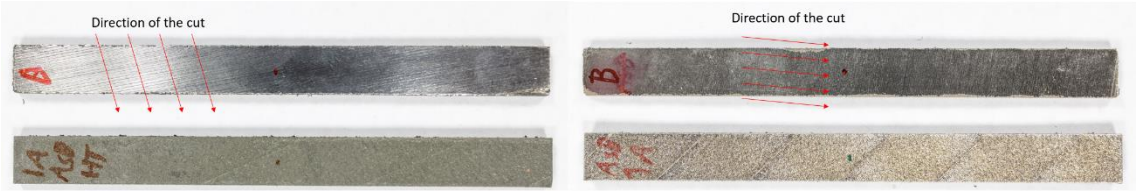

Figure 62: *AsB HT and AsB samples showing the different cutting directions on their B-sides*

All of the shot peened samples (AsB SP, AsB HT SP and Ref SP) show compressive residual stresses on all surfaces as expected. The AsB SP and AsB HT SP samples have higher compressive residual stresses, when compared to the Ref SP sample (-555 MPa on AsB HT SP and -502 MPa on AsB SP versus -186 MPa on Ref SP), but this is most likely related to the software used to calculate the stresses. As can be seen in figure 34, the measurement data from the Ref SP samples contains an extra peak, obscuring the diffraction peak used by the software to calculate the residual stresses. Limiting the calculation to just the peak of interest yielded different results, but even small changes in the placing of the limits results in changes in the calculation results. The peak limits are set as pixel values, with the scale being from 0 to 500 pixels. To quantify how big an effect different peak limits have, the results from two calculations with different limits and one without limits were compared. The results are compiled in table 12.

Table 12: *Calculation results with different peak limits compared*

	Ref SP 1			Ref SP 2			Ref SP 3		
	No limits	Peak limit 120-500	Peak limit 150-500	No limits	Peak limit 120-500	Peak limit 150-500	No limits	Peak limit 120-500	Peak limit 150-500
Average surface stress [MPa]	-232	-258	-251	-210	-216	-250	-183	-83	-164
Difference [MPa]	0	-26	-17	0	-6	-40	0	100	19

As can be seen from table 12 above, the results vary by up to 100 MPa between limits used within a sample.

The values of the limits were decided by looking at the pixel values of the diffraction patterns obtained, and by placing the limits so that the extra peak would be limited from the calculation. Two of the diffraction patterns are presented in figure 63.

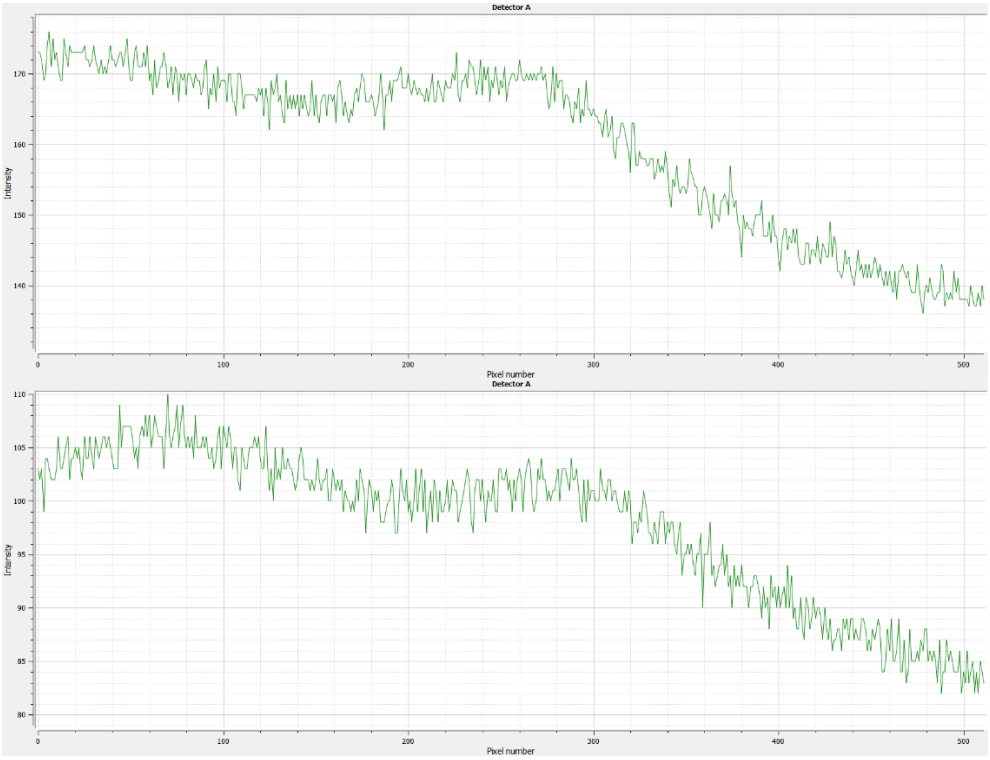

Figure 63: *Two different diffraction patterns presented as pixel values; top from Ref SP 1, bottom from Ref SP 3*

As can be seen from figure 63, the pixel value at which the extra peak, the peak on the left in the images, begins is different. This entails that by choosing the limits based on, for instance a diffraction pattern from Ref SP 1, the limits may not be correct for Ref SP 3, as is the case here. Thus, if using peak limits, it is important to choose the limits individually for each sample. Nevertheless, the results from the initial XRD measurement will be left as is, as the absolute stress values on the shot peened samples are not of interest.

This extra peak seen in the Ref SP diffraction pattern in figure 34 is around 156º, which corresponds to ferrite and more importantly martensite. Shot peening is known to cause martensite transformation in conventional 316L steel [83,84], which would explain the extra peak in the shot peened reference sample. AM 316L on the other hand has been shown not to transform to martensite during plastic deformation. Hong et al [51] concluded in their work, that the cellular microstructure and high amount of low-angle grain boundaries (LAGB) restrict dislocation slip and the formation of deformation twins, reducing nucleation sites for strain-induced martensite [51]. Suppression of strain-induced martensite would explain the absence of the extra peak on the AsB SP sample. However, the AsB HT SP sample does not show an extra peak either, even though the stress relief annealing performed on it should have changed its microstructure, and this new microstructure was the one that was shot peened.

Other possibilities for the extra peak were also investigated, including equipment related anomalies and possible other elements in the material diffracting the x-rays. However, both of these possibilities were determined not to be cause of the extra peak.

4.2 Residual stress depth profiles

After the initial surface XRD tests, several RS depth profiles were measured. The results obtained from those are discussed next.

The residual stress states on the bottoms of the AsB and AsB HT samples were confirmed to have been caused by the band saw. Residual stress depth profiles measured from four different locations on three different samples show the stress state losing its anisotropy when moving further into the sample. The stress state returned to isotropic around 90 microns into the sample, as can be seen in figure 36 a) & b).

A residual stress depth profile was measured from the top side of one of the AsB samples, to characterize the stress state in the sample further. The measured profile presented in figure 37 shows that there is a slight increase in tension as a function of depth from the top surface of the sample. It must be noted that deviation within the results is quite high and that this is the only successful RS depth profile measured from an AsB top surface. Another profile was attempted on the same sample, but as can be seen from figure 37, the stress state in the sample had been relieved, possibly due to a piece cut from the other end of the sample for metallographic purposes.

This single result is nevertheless in line with previous studies [8,61] and other observations regarding the residual stress state generated during AM. When metal is initially added to the surface of the build plate, the molten metal cools rapidly, causing it to shrink. As the shrinking material is constrained by the build plate, tensile residual stresses develop in the material and compressive residual stresses develop in the build plate. These residual stresses are relieved when new material is added on top of the first layer, remelting and effectively annealing it. Then the cooling process is repeated with now the previously deposited layers constraining the newly deposited one, creating compressive residual stresses at the bottom layers and tensile stresses at the newly deposited ones. This continuous process generates a residual stress state such that the bottom of the component is in compression while the top is in tension with a neutral axis somewhere in between.

Besides the one RS depth profile confirming tensile residual stress in the top surface of the sample, another observation suggesting the previously described stress state is the fact that all the samples removed from the build plate before heat treatment (AsB and AsB SP) are bent upwards, as is illustrated in figure 19. A second indication is the tearing of the tips of samples from the support structure during the first unsuccessful print run. This tearing is presented in figure 18.

Residual stress depth profiles from the bottom sides of two AsB samples presented in figure 36 show, that once the stress state induced by the band saw is passed the residual stresses tend towards zero and even tension. Based on what was discussed earlier on the type of stress state that is generated in the samples on the build plate, it could be expected that a near zero or a compressive RS state would be found. There are two obvious reasons why this is not the case. First, the band saw may have altered the stress state in the entire, relatively small sample by inducing isotropic compressive residual stresses to the sample. Second, the samples were printed on a solid support structure,

i.e. it is ambiguous where the support ends and the sample begins. This means that the stresses would be distributed along the entire piece of printed material and the samples were cut from somewhere in between this distribution.

From the tearing of the samples from the initial support structure it is obvious that a stress state with compression at the bottom and tension at the top is present in the samples. It can also be concluded that the bending of the samples after removal from the build plate is not due to stresses induced by band sawing, by looking at the samples removed from the build plate after heat treatment. Those samples are straight, as they should be despite being removed with a band saw, given that the stress relief annealing specifically reliefs any residual stresses in the samples. However, based on these results the residual stress state above the band saw marks and on the top surface of the sample could either be due to stresses generated during printing or induced by the band sawing.

Residual stress depth profiles measured from the shot peened samples show a typical profile of compressive residual stress reaching a maximum value below the surface of the component and then tapering off. Comparing the two reference samples, one of which was shot peened once and the other three times, it can be seen that the one shot peened three times has more intense compressive stresses under its surface ranging from a maximum of -700 MPa to -400 MPa at 100 microns under the surface. In comparison, the Ref SP sample shot peened once has a maximum of -620 MPa and a minimum of just -130 MPa at 100 microns under the surface. The AM sample shot peened once sits between the two Ref SP samples, at -600 MPa to -280 MPa at 100 microns. The RS depth profiles are presented in figure 38.

The shot peened AM sample having a higher intensity compressive stress under the surface than Ref SP 1 is counterintuitive. RS depth profile from an AsB sample showed that at the top surface, from where the profile of the AsB SP sample was measured as well, there is a tensile residual stress, which would have to be overcome, before compressing the material. Secondly, is has been shown [3] that additively manufactured steel components have a higher yield strength when compared to their annealed counterparts, meaning that the AsB sample should be able to better resist plastic deformation and generation of compressive RS. A possible explanation for this discrepancy is the fact that the shot peening was performed by hand. Perhaps the operator held the AsB sample closer to the nozzle, thus increasing the intensity of the peening.

The extra peak in the XRD results of the Ref SP samples discussed earlier vanishes and the diffraction peak comes more pronounced, improving calculation accuracy as the surface of the material is removed. This disappearing of the extra peak would further indicate that it is caused by some of the austenitic microstructure transforming to martensite at the surface of the material, due to the plastic deformation caused by shot peening.

4.3 Corrosion tests

In the next chapter, the corrosion tests will be discussed. First the discrepancies between the XRD results and the strain gage values will be discussed.

As can be seen from table 9, the stress values measured with the XRD differ significantly from the ones calculated from the strain gage values with the stress state in the welded sample showing, according to the XRD, as being in compression and not tension. The XRD results from the AM samples, AsB and AsB HT, are in line with each other. Both are in tension and the one under more intense stress (AsB) has a higher XRD result as well. The reason both results are significantly lower than expected could be due to the uneven surface of the AM samples. As mentioned previously, XRD only measures a few microns under the surface of the material [91]. This means that the XRD results are from the rough details of the sample, not from the uniform material under it. The details on the surface of the material may not be at the same stress state if they are for instance oriented perpendicular to the bending direction.

The XRD result obtained from the relatively flat Ref 1A sample also follow the previously presented hypothesis, being just 65 MPa under the expected value of 180 MPa. However, the results from the welded sample are completely off, showing 118.5 MPa of compression instead of 180 MPa tension on the surface. The deviation between the three measurements from the surface of the welded sample is the highest of all four samples, at 48 MPa, but all three measurements were still consistently negative, i.e. in compression.

During welding the hot weld bead cools and shrinks, constrained by the surrounding material, leaving the bead under tension and the material around the bead under compression. The measured RS profile from the surface of the weld in Ref weld 1A does not show an expected RS profile, as can be seen in figure 35, but it does show that the material around the weld is under significant compression. The point measured from the middle of the sample (0 mm) was measured from the round weld bead, which may affect

the result obtained for the middle point, and does in fact show abnormally high deviation, when compared to all the other surface XRD results. This is not critical regarding the evaluation of the stress state before and after the corrosion tests however, as those measurements were made from a flat section of the sample.

As the material around the weld in 0-direction is under compression, it can be deduced that adding 180 MPa of tension to the surface of the material may still not be able to bring the surface into tension, thus resulting in negative stress values from the XRD.

After the initial corrosion test of 237 hours, the samples, while still in the 4PB rigs and under tension, were measured using XRD to see, if the stress state had changed during exposure. The obtained results are presented in table 13.

Table 13: *Surface stresses of the first corrosion test samples while under tension before and after testing*

Sample	**Ref 1A**	**Ref weld 1A**	**AsB 1A**	**AsB HT 2A**
Before exposure	114.9 MPa	-118.5 MPa	151.2 MPa	51.7 MPa
After exposure	-167.2 MPa	-241.5 MPa	-83.4 MPa	24.5 MPa

The results are unexpected. The welded sample is still under compression, as expected, and the HT sample's stress state did not change much. However, the Ref and the AsB samples going from tension to compression is simply baffling. All of the results are averages of two, three in the case of the welded one, measurements. The deviations of the Ref and AsB samples are 22 MPa and 5 MPa respectively, so, even though it is just two measurements per sample, it is most likely not an erroneous result. What makes this result even more confusing is the fact that after the XRD measurements the samples were removed from the 4PB rigs and all of them were visibly relieved from tension, as they all bowed back when released. No clear explanation to this changing of stress state can be given with the current information. Perhaps the samples were not cleaned properly before measuring, or perhaps something happened to the surface of the material during exposure. However, the latter explanation seems unlikely, as the stress state changed in the Ref sample and the AsB sample, two very different microstructures, but

not in the other two samples. The surface quality of the Ref and AsB samples is very different as well. Another explanation might be an equipment malfunction. More research would need to be done, to find out what caused this apparent change in stress state.

As already mentioned in the experimental part, the corrosion tests failed to induce any SCC on any of the samples. The cross-sections of the samples from both the 237-hour and the 674-hour corrosion tests were observed at two different depths, but no signs of corrosion nor cracking were detected. SCC is not the cause for the cracks visible in the cross-section of the reference sample presented in figure 42, as similar cracks can be seen on the other edge, one that would have been under compression during testing, of the cross-section as well. The etching of the sample most likely causes these cracks, as the cracks are only visible in the etched areas.

Some results of austenitic stainless steels' SCC behaviour in chloride solutions have been reported before. Crack growth rates between 10^{-11} and 10^{-8} m/s have been reported for 304 and 304L type stainless steels with both sensitization and annealing heat treatments in 22% NaCl solution under a constant load [87]. The same study reported a crack growth rate of over 10^{-8} m/s for an annealed 304L steel at 42% $MgCl_2$ solution, though this result was obtained at 130 ºC [87]. Elsariti and Haftirman [95] studied SCC of 316 stainless steel at 3.5 wt-% and 9.35 wt-% NaCl solutions at room temperature under a constant load. They reported that at 404 hours no cracks were detected in any of the samples. At 838 hours the samples in the 9.35 wt-% NaCl solution had cracked and at 1244 hours the samples in the 3.5 wt-% NaCl solution had cracked as well. [95]

The current tests were performed on 316L steel in 50 wt-% $MgCl_2$ solution at 80 ºC for up to 674 hours. The conditions and materials in this and the two studies mentioned are quite different, making comparisons difficult, but not impossible. 316L is generally considered to be more corrosion resistant owing to its added molybdenum content [81]. The better corrosion resistance of 316L when compared to 304L has also been shown in studies [11,96]. Another thing to compare is the stress intensity factor, which in the first study is given as 40 to 50 MPa($m^{1/2}$). The stress intensity factor in this study can be estimated by assuming an edge crack on an infinite plate and calculating using the equation

$$\boldsymbol{K_I = 1.1215\sigma\sqrt{\pi a}}, \tag{5}$$

where σ is the stress pulling the crack open, i.e. the stress on the surface of the bent sample in this case, and a is the crack length [97]. By substituting 350 MPa as the stress,

as this is the stress used for the AsB sample, and by estimating from figure 39 that $20*10^{-6}$ m would be the maximum initial depth of a crack on the surface, we get only 3.11 MPa($m^{1/2}$) as the stress intensity factor. This calculation along with the improved corrosion resistance of 316L puts the current results well in line with the study performed on 304 and 304L stainless steels.

Elsariti and Haftirman [95] observed SCC in 316 steel in 9.35 wt-% NaCl solution at 838 hours and in 3.5 wt-% NaCl solution at 1244 hours, indicating at a relation between chloride concentration and SCC incubation time. Thus it is surprizing that no SCC was observed in the current study on 316L at much higher chloride concentration at an exposure time between the two observation times of 404 hours and 838 hours of Elsariti and Haftirman [95]. Their results were also obtained in room temperature, while the current study was performed at 80 ºC. The authors do not state what intensity of loading was used in their study, stating only that a constant load setup was used. Perhaps their loading was much more intense than in the current study. The studied materials are also slightly different, 316 versus 316L, though 316L is generally considered more corrosion resistant only after welding, where the low carbon content of 316L inhibits the precipitation of chromium carbides [10].

There are also many factors in the current study that may have affected the results. Firstly, the 4PB rigs used were not inert in the test environment. Even though the rigs were painted, to protect them, the paint peeled off from several locations, exposing the aluminium underneath. The less noble aluminium could have provided anodic protection to the steel, especially if there was electrical contact between the two. Care was taken to isolate the steel from the aluminium, but it was not actually tested at any point whether the isolation worked before and after testing. In hindsight, this would have been easy to do with a simple multimeter. Another reason could be the actual stress state present at the material surface. As discussed earlier, the tensioning of the samples in the 4PB rigs may not have been able to bring the samples to the desired stress states, and instead left them under the threshold stress required to initiate SCC [11] or even under compression. Also, as postulated by Elsariti and Haftirman [95], there could be an incubation period required to initiate SCC. Perhaps these relatively short tests of just 674 hours were too short to induce SCC under the given circumstances.

4.4 Metallography and hardness measurements

Optical micrographs of the AsB sample presented in figures 43 and 44 show a microstructure typical of a L-PBF processed metal. Individual laser tracks and melt pool boundaries are visible, allowing for instance, the 100 µm hatch spacing to be measured. Epitaxial grain growth can also be seen, indicating that the heat input from the laser beam was large enough to create a melt pool that cooled sufficiently slowly. From the 100x magnified optical image and the secondary electron (SE) image in figure 46 the micrometre scale cellular microstructure can be seen. The cell size was measured to be on average 0.7 µm in diameter, which is in line with previous studies [47–51]. The precipitation of alloy elements in to the cell walls could not be studied, as the resolution of the energy dispersive spectrometer (EDS) of the SEM was not high enough. Figure 45 presents the microstructure of a heat-treated AM sample. The microstructure has recrystallized, and the melt pool boundaries are no longer visible.

L-PBF is capable of producing parts with very high relative density, with over 99% density reported in studies [37,44]. In the current study, the cross-sections studied also demonstrated high relative density.

In order to confirm the presence of martensite on the surface layers of the shot peened samples, optical micrographs were taken. At the surface layer of a shot peened reference material in figure 47, clear striations can be seen. These striations seem very similar to the ones detected by Hong et al [51] in both annealed and L-PBF processed 316L strained by 10% at 80K. A micrograph from their work is presented in figure 64.

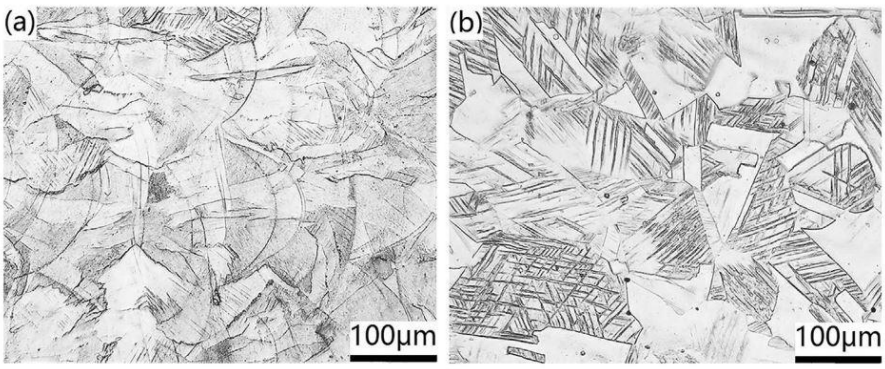

Figure 64: *Deformation twins in (a): L-PBF processed and strained 316L (b): annealed and strained 316L* [51]

Zhang and Zheng et al [51] interpreted the striations as deformation twins and concluded that the deformation twins act as nucleation sites for strain induced martensite. They were also able to confirm the presence of martensite in their samples by electron backscatter diffraction (EBSD) imaging.

Twinning is a mechanism, by which plastic deformation can occur in a crystalline structure, and it can be considered a competitive mechanism with dislocation slip. Typically, dislocation slip dominates in FCC metals, such as austenitic steel, but there are exceptions. During twinning, the coordinated movement of atoms takes up the plastic deformation in a lattice, and a mirror image, or a twin, of the original lattice is created. [98] Several factors influence the twinning of materials, including temperature, strain rate and pre-strain in the material. Lower temperatures encourage twinning in a material, as do high strain rates. Pre-straining on the other hand has been shown to supress twinning. [99] For the sake of the current study, suppression of twinning by pre-strain and encouragement of twinning by high strain rates are of importance, as the AM samples contain pre-strains in the form of residual stresses, and on the other hand, the shot peened samples have experienced high strain rates during peening.

In figure 48, a micrograph of heat-treated AM sample can be seen. The diffraction pattern of heat-treated AM samples did not contain an extra peak, yet in the micrograph, similar striations as on the reference material can be seen. The heat-treated AM material is expected to behave similarly as the reference material, as it has recrystallized during annealing, as discussed earlier. Thus, it was surprising that the diffraction pattern did not contain an extra peak.

If, going by the work of Hong et al [51], the striation in the current study are also interpreted as deformation twins and not martensite, as was initially thought, the differences in the diffraction peaks could be explained. In the reference material, the strain induced by the shot peening was enough to create both deformation twins and martensite. In the heat treated AM sample, for some reason, the deformation was enough to create deformation twins, but not enough to create martensite. Perhaps despite having seemingly completely recrystallized it still somehow restricts the formation of martensite. In the AM sample, the deformation was not enough to create neither deformation twins nor martensite. Some striations can be seen on the left of figure 49, but they are obscured by the cellular microstructure. Either way, if these striations are deformation twins, there are significantly fewer of them, when compared to the other two samples. EBSD measurements would be needed to confirm this hypothesis about the formation of martensite.

To further characterize the effects of shot peening on the samples, micro hardness measurements were performed. Micro hardness depth profiles measured from different shot peened samples in figure 52 show a typical hardness profile, with a region of deformation-hardened material at and near the surface. A difference in hardness between the Ref SP1 and Ref SP 3 samples can also be seen. The sample shot peened three times, instead of one time, is harder at the surface, due to a higher level of plastic deformation. AsB sample shot peened twice and a heat treated sample shot peened three times sit logically between the two reference samples. Moving further into the material, the hardness of the as built sample overtakes the others. The higher hardness of the AsB samples' bulk material can also be seen in table 10. The higher hardness of the AsB samples' bulk material is due to the high amount of dislocations [7] and the fine microstructure of the material [47–51], created by the high cooling rates.

Figure 52 and table 10 both also show, that the hardness of the bulk of the heat treated sample is below that of the AsB sample, as expected, but it is also slightly higher than that of the reference samples. This further indicates, that the heat treatment did not completely recrystallize the microstructure, but instead some degree of hardening factors, like dislocations or LAGBs, have been retained.

Figure 53 shows the hardness depth profiles of two different AM samples, one shot peened twice and one in as built condition. The AsB sample's profile is measured starting from the top surface, and seems to be softer at the top. This is unexpected, as the surface layer of the component does not experience re-melting and effective annealing due to the heat input from subsequent layers. Intuitively it would therefore contain more dislocations and be therefore harder. The lower hardness of the top layer is probably due to different printing parameters used to print the last layer. The top layer of 40 µm was printed using laser power of 150 W and a scan speed of 515 m/s, instead of the 214 W and 928 m/s used for the infill.

The FWHM values of the diffraction patterns are known to correlate with microstrains and hardness of the material [92,93]. FWHM value depth profiles of selected shot peened samples are presented in figure 65.

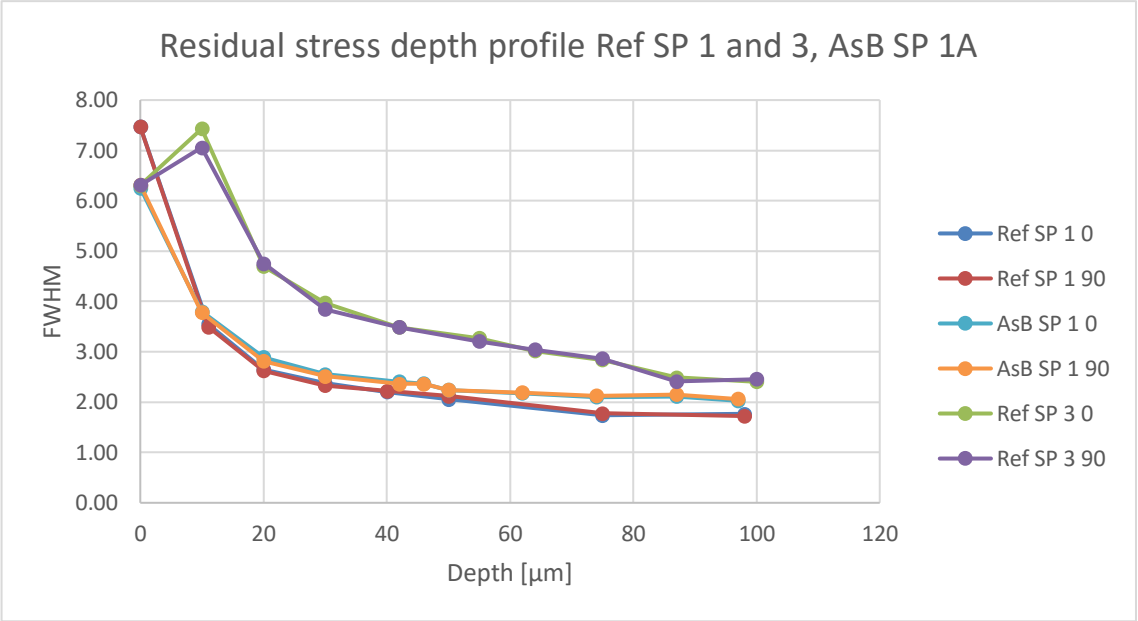

Figure 65: *FWMH value depth profiles of selected shot peened samples*

The values correlate well with the hardness depth profiles presented in figure 52, though some differences can be seen as well. Firstly, the FWHM values of the Ref SP 3 sample show a maximum at around 10 µm below the surface. Unfortunately, the micro hardness-measuring device is not accurate enough to measure the hardness at 10 µm increments. Secondly, the FWHM values of the AsB SP 1 sample below the surface are higher than those of the Ref SP 1 sample, indicating a higher hardness, as expected. The FWHM values of the Ref SP 3 sample are higher still, but this is most likely due to the higher intensity of the shot peening. The crossover point of the hardness values between the AsB SP 2 and Ref SP 3 samples in figure 52 is only at around 80 µm. Had the RS depth profile been continued beyond 100 µm, the FWHM value of AsB SP 1 would most likely have overtaken Ref SP 3.

4.5 Rapid mixing nozzles

The residual stresses measured from the surfaces of the rapid mixing nozzles confirm the assumptions made based on the nozzles surface qualities. There is a large compressive residual stress state at the surface, and the surface has been plastically deformed, based on the high FWHM values. Interestingly, the diffraction patterns from two of the nozzles show an extra peak similar to what was seen on the shot peened reference material, but the third one does not. An extra peak is not expected, based on earlier studies into shot peened AM material, whether heat-treated or not. The surface quality of nozzle 3, the one without the extra peak, visually resembles that of the shot peened samples studied earlier. Based on this and the lack of an extra peak, nozzle 3 was most

likely shot peened. However, the surface quality of nozzles 1 and 2 is much smoother and shinier. A small ceramic particle fell out of one of the two nozzles, which would lead to believe that the parts were either ball milled, or more likely tumbled. The appearance of the extra peak on these two components indicates, that whatever the process they have been subjected to, it has induced more intense plastic deformation on the surface of the components, when compared to the assumed shot peening on the third nozzle. It must be noted though, that nozzles 1, 2 and 3 may all have come from a different batch of components with different printing parameters and, therefore, different properties.

The RS depth profiles measured from two spots on the flange of nozzle 2, presented in figure 58, show an initial compressive residual stress state, which reaches maximum intensity around 20 µm below the surface of the material, further confirming some sort of plastic deformation on the surface. After reaching maximum compression, the stress state transforms to anisotropic tension, with 0-direction being under tension and 90-direction being at near zero stress. One explanation for this anisotropy could be the scanning strategy used. The use of a unidirectional scanning strategy is known to cause an anisotropic stress state [30].

Comparing the RS profiles from the nozzle to the one measured from an AsB sample, presented in figure 37, it can be seen, that with the AsB sample, when hatch angle rotation was used, the tensile residual stress state is isotropic. It must be noted though, that the AsB sample is very simple in its geometry, while the rapid mixing nozzle is not.

The RS profiles measured from the inside walls of the largest tube of the nozzle are presented in figure 59, and tell a similar tale, regarding the anisotropy. After some distance below the surface, the stresses in the 0-direction are in tension and the stresses in 0-direction are near zero. The fact that the stress states are similar in nature regardless of whether it has been measured from the outside or inside surface or from a top or bottom surface would further indicate that it is related to scanning strategy, which, if unidirectional would cause stress anisotropy invariant of where in the sample the stresses are measured.

The intensity of the compressive residual stresses on the inside surfaces of the component is less than on the outside surfaces. The absolute stress values are smaller, and the compressive stresses do not go as far beneath the surface. This is expected, as the inside surfaces would have been protected whatever surface finishing was performed on the nozzle. However, interestingly, the stress states on the inside are different from each

other as well, as can be seen in figure 59. The top surface starts at a lower compressive stress state, than the bottom surface, and at around 50 µm below the surface, the stress states are similar to the ones measured from the outside. Possible explanation for this could be that the top surface of the tube was somehow more protected than the bottom. After all, the post processing steps are not known.

Examples of diffraction patterns obtained from the surface of nozzle 2 are presented in figure 66.

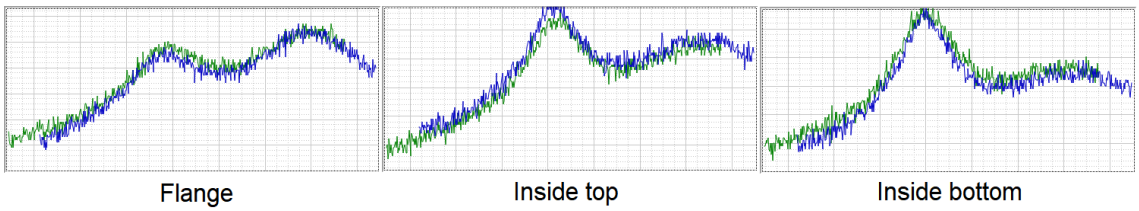

Figure 66: *Examples of diffraction patterns from the surface of nozzle 2*

At the surface the peak located at higher diffraction angles in the diffraction pattern is more pronounced, while the austenite peak is less pronounced and wider, when compared to the patterns from the inside surfaces. Based on the studies done on the shot peened samples, this would further indicate, that the inside surfaces have seen less plastic deformation, i.e. they have been more protected.

It must be noted, that the stress profiles presented in figures 58 and 59 were measured at a 45º angle to the build direction. The stresses in the build direction have been shown to be near zero [8,61], at least in samples with simple geometries. Assuming that the stresses in the build direction are near zero in this case as well, the stresses in the 0-direction, if measured parallel to the build direction, would be even higher.

As stated by Ghasri-Khouzani et al [61], the stress state of a component evolves throughout the deposition of the layers, and in the case of this nozzle and specifically the area investigated, the subsequent layers are not directly on top of each other, but offset by roughly the layer height to get the 45º angle. Overall, the 45º tilt, relatively complex geometry, the fact that the printing parameters are not known and the compressive stresses at the surface make this particular stress state very difficult to interpret.

From the microstructures presented in figures 60 and 61 a several things can be seen. Firstly, it is obvious, that this nozzle has not been heat treated after manufacturing, as the melt pool boundaries are still clearly visible. The micrometre scale cellular structure

is also still visible. Secondly, on the outside wall of the tube in figure 60 a darker layer of roughly 200 µm of visibly finer microstructure can be seen. On the inside surface on the other hand this layer is only about half as thick. This could either be due to the plastic deformation to the surface, where, as discussed earlier, the inside surface would have been more protected. On the other hand it could also be due to different printing parameters used to print the top and bottom surfaces of the component.

What is not present in these micrographs is deformation twinning, which is consistent with earlier results from the shot peened samples. This material is evidently still in as built condition, so no deformation twinning is expected. Despite this, the second peak in the diffraction pattern is present, which can mean two things. Either, in this case, martensite was formed without the formation of deformation twins, or the appearance of the second peak is not related to martensite.

Comparing the AM sample series' and the mixing nozzle's materials, they both show properties typical of AM 316L. The microstructure has the micrometre scale cellular structure and the melt pool boundaries. Both materials demonstrate epitaxial grain growth and their diffraction patterns behave similarly, excluding one exception. While the sample strips' material demonstrates an extra peak in the diffraction pattern that is related to plastic deformation to the surface and seems to be related to deformation twinning, the nozzle's material shows an extra peak without the twinning. Both materials behaved similarly during electrolytic etching and polishing, and demonstrated similar x-ray diffraction characteristics, in terms of exposure time required to gather data. The layer of finer microstructure present on the surfaces of the nozzle is unique, not seen in any of the strip samples. This further confirms that the nozzle has gone through more than just shot peening.

5. CONCLUSION

In this literature review and study, additive manufacturing of metal components was studied. First, an overview of additive manufacturing of metals was given, followed by some state-of-the-art techniques. On the practical side, additively manufactured 316L stainless steel samples were characterized both non-destructively and destructively and compared to traditionally manufactured reference samples. The residual stress states of the samples were characterized using x-ray diffraction, RS depth profiles were measured and the microstructures of the samples were characterized. In addition, corrosion tests were performed to study the stress corrosion cracking behavior of the samples.

Based on the result from the initial XRD measurements it can be concluded that XRD enables the relative residual stresses on the surfaces of components to be compared and it can differentiate between large differences and anisotropies. Small differences on the other hand can easily become obscured by measurement errors, like differences in calibration and the placing of the detectors. When studying plastically deformed surfaces with obscured or weak diffraction patterns, the use of peak limits in stress calculation can help in getting comparable absolute stress values, but care must be taken to choose suitable limits separately for each sample.

Band sawing of the samples from the build plate or support structure was found to induce an anisotropic stress state to the material, reaching to around 90 microns into the material.

A single successful RS depth profile was measured from an as built condition sample, which showed an expected tensile RS state on the top surface of the component. This result was supported by other observations, namely the bend in the samples after removal from the build plate.

During 4-point bending of the corrosion samples, the XRD proved to be quite unreliable at measuring stresses from bent samples. The stress values measured before the tests were counterintuitive, but could be explained by lower stress values on the details of a rough surface and significant compressive stresses near the weld in that sample. The inversion of measured stress values of two of the samples after the corrosion tests however, are still a mystery.

Earlier it was mentioned, that the samples were designed with a U-bend test in mind, but it was eventually decided that a 4-point bending test would be used. U-bending would have indeed been another possibility to produce a stress state in which one surface of the sample would have been under tension and the other under compression. 4PB was chosen over U-bending for a number of reasons. While 4PB requires a more complex, though still relatively simple, tensioning rig, it gives more control over the intensity of the stress state. 4PB is also gentler on the samples, as it does not plastically deform them

The corrosion tests themselves show, that at under a 50% $MgCl_2$ solution at 80 ºC under bending, inducing stresses 75% of material the yield strength, 316L, neither annealed nor AM experience corrosion. This could be due to multiple factors. The environment may not have been aggressive enough, and the material was simply immune to corrosion in said conditions. Another reason regarding the conditions may be that despite being tensioned using strain gages, the 75% of material yield strength was not reached. This could be especially true with the welded sample, where there was significant compression before bending. Secondly, despite best efforts to insulate the two, the aluminium bending rigs may have protected the steel. Thirdly, maybe the 674-hour exposure time was not long enough to induce SCC. A longer test run with inert bending rigs and some other way of assuring correct stress values would be needed to study the immunity and incubation period of AM 316L in these conditions.

RS depth profiles from the shot peened samples showed an expected compressive RS state across all samples. The AsB SP 1 sample had higher compressive stress values than expected, when compared to the reference sample, but this was concluded to be due to inconsistencies during shot peening.

The RS depth profiles from the rapid mixing nozzles showed a similar initial compressive RS state as with the shot peened samples, though in the nozzles the compressive stresses were more intense. In the nozzles, instead of staying isotropic, the stress state changed to anisotropic tension further into the sample. Several factors could lead to this, the prime suspect being the scan strategy used to print the component.

Surface XRD results from the rapid mixing nozzles showed compressive residual stresses on all three nozzles and the diffraction pattern of two of the nozzles had an extra peak in them. One of the nozzles, based on its surface quality, was shot peened and did not show an extra peak in the diffraction pattern. The two others, with and extra peak,

were assumed to have gone through a more severely deforming surface treatment, like ball milling or tumbling.

Similar extra peaks were observed in shot peened reference samples, but not in shot peened nor heat-treated and shot peened AM samples. This extra peak was initially interpreted to be due to martensite, generated by the plastic deformation to non-AM samples, mainly because its diffraction angle matched that of martensite and because it disappeared during RS depth profiling. The missing of the extra peak from the heat-treated and shot peened AM sample was interpreted to be due to incomplete recrystallization during heat-treatment and subsequent suppression of martensite transformation.

Micrographs of the shot peened samples revealed, that a heat treated and shot peened AM sample and a shot peened reference sample had both transformation twins in their microstructure. A shot peened AM sample possibly had a small amount of twinning as well, but it was not nearly as prevalent as with the other samples. The presence of martensite however, could not be confirmed.

Micrographs were also made of one of the rapid mixing nozzles, specifically one with an extra peak, and they showed no twinning nor obvious signs of martensite.

The appearance of the extra peak seems to be unrelated to deformation twinning, but somehow still related to plastic deformation of the surface of the material. Perhaps there is some limit in plastic deformation, beyond which the second peak appears, and this limit is higher for AM steel. Based on the current results this limit seems to be independent of deformation twinning, but could still be related to martensite. EBSD measurements would be required to study whether the deformed face-centered cubic structure of austenite has any body-centered cubic ferrite or martensite in it.

Comparing the microstructures of the samples and the nozzle to each other, they both show characteristics typical of an AM steel. The melt pool boundaries are visible, allowing the hatch spacing to be measured, and both show the typical micrometer scale cellular microstructure. The area of finer microstructure at the surface of the nozzle was interpreted to be due to more severe surface treatment than shot peening, as no such layer can be seen on the shot peened samples.

Some outlooks for studies into AM include developing in-situ stress measurement techniques and finding practical uses for microstructure tailoring and compositional grading.

In-situ stress measurements would further elucidate the evolution of residual stresses in larger and more complex components, allowing simulations to be confirmed and improved upon, which could further translate to better predictions and, more importantly, control methods of residual stresses. Finding practical uses for microstructure tailoring and compositional grading could bring techniques similar to case hardening and coating, and design methods like designing components of varying strength to a car chassis to ensure safer crash behaviour, to AM component designing and manufacturing.

REFERENCES

1. Hague R, Mansour S, Saleh N. Material and design considerations for Rapid Manufacturing. Int J Prod Res. 2004;42(22):4691–708.
2. Kellner T. The Blade Runners: This Factory Is 3D Printing Turbine Parts For The World's Largest Jet Engine [Internet]. GE Reports. 2018 [cited 2019 Feb 14]. p. 1. Available from: https://www.ge.com/reports/future-manufacturing-take-look-inside-factory-3d-printing-jet-engine-parts/
3. DebRoy T, Wei HL, Zuback JS, Mukherjee T, Elmer JW, Milewski JO, et al. Additive manufacturing of metallic components – Process, structure and properties. Prog Mater Sci. 2018;92:112–224.
4. Bourell D, Kruth JP, Leu M, Levy G, Rosen D, Beese AM, et al. Materials for additive manufacturing. CIRP Ann - Manuf Technol [Internet]. 2017;66(2):659–81. Available from: http://dx.doi.org/10.1016/j.cirp.2017.05.009
5. EOS Industrial 3D printing - Process, method and benefits [Internet]. [cited 2019 Aug 19]. Available from: https://www.eos.info/additive_manufacturing/for_technology_interested
6. SLM Solutions Group AG: Aviation and Aeronautics [Internet]. [cited 2019 Aug 19]. Available from: https://www.slm-solutions.com/en/industries/aviation-and-aeronautics/
7. Gorsse S, Hutchinson C, Gouné M, Banerjee R. Additive manufacturing of metals: a brief review of the characteristic microstructures and properties of steels, Ti-6Al-4V and high-entropy alloys. Sci Technol Adv Mater [Internet]. 2017;18(1):584–610. Available from: http://doi.org/10.1080/14686996.2017.1361305
8. Brown DW, Bernardin JD, Carpenter JS, Clausen B, Spernjak D, Thompson JM. Neutron diffraction measurements of residual stress in additively manufactured stainless steel. Mater Sci Eng A [Internet]. 2016;678(September):291–8. Available from: http://dx.doi.org/10.1016/j.msea.2016.09.086
9. EOS GmbH - Electro Optical Systems. Material Data Sheets EOS StainlessSteel 316L. Data Sheet [Internet]. 2014;49(0):1–5. Available from: www.eos.info
10. Supra O. Stainless steels for highly corrosive environments Outokumpu Supra range datasheet. :1–12.
11. Mayuzumi M, Hayashibara H, Tani J, Arai T. Failure Propensity of Austenitic Stainless Steels by Chloride Induced Stress Corrosion Cracking in Air. Zairyo-to-Kankyo. 2007;55(1):20–4.
12. Krawczyk B, Cook P, Hobbs J, Engelberg DL. Atmospheric chloride-induced stress corrosion cracking of laser engraved type 316L stainless steel. Corros Sci. 2018;142(July 2017):93–101.
13. Kirk D. Shot peening. Aircr Eng Aerosp Technol. 1999;71(4):349–61.
14. Totten GE. Steel Heat Treatment: Metallurgy and Technologies [Internet]. 2nd; 2nd ed. Baton Rouge: CRC Press; 2006. Available from: http://tut.summon.serialssolutions.com/2.0.0/link/0/eLvHCXMwjV1LT8JAEJ6AXCQmPtCIaNJ4L4Hd7m57NiIh4STxdWn2eZEQI0X_vrPbFhAOemw62WZnt988MvMNACX9QbyDCW6o0fXQSqHB4KnijgtjvK03TlsdMgXPb2T6wiaT9LUB9WS57zBzQ2OQ7jE9ALcPfTwt7CBNMpomGEc1oTVM0K33l_IhuE6weOcZfZfA-ViKsqx
15. J. P. Kruth, J. Duflou, P. Mercelis, V. Jonas, T. Craeghs, J.Keuster. On-line monitoring and process control in selective laser melting and laser cutting. Proc 5th LANE Conf Laser Assist Net Shape Eng. 2007;1(1):23–37.
16. Hussein A, Hao L, Yan C, Everson R, Young P. Advanced lattice support structures for metal additive manufacturing. J Mater Process Technol [Internet]. 2013;213(7):1019–26. Available from: http://dx.doi.org/10.1016/j.jmatprotec.2013.01.020
17. Parry LA, Ashcroft IA, Wildman RD. Geometrical effects on residual stress in selective laser melting. Addit Manuf [Internet]. 2019;25(June 2018):166–75. Available from: https://doi.org/10.1016/j.addma.2018.09.026
18. Akmal JS. Digital Unique Component Manufacturing through Direct and Indirect Additive Manufacturing. 2017; Available from: http://urn.fi/URN:NBN:fi:aalto-201710307355
19. Dusel K-H. An Intelligent Strategy for Achieving Excellence: MTU Relies on Additive Manufacturing for its Series - Component Production EOS Technology Enables the

Cost-Effective Manufacture of Engine Components for the Airbus A320neo. MTU Aero Engines. 2016;
20. Case C, Aerospace S. Durable up to the Sound Barrier and Beyond Flow measurement probes from Vectoflow — highly robust thanks to additive manufacturing and EOS.
21. EOS M 400 for Additive Manufacturing for the Industrial Production of High-Quality Large Metal Parts. – EOS [Internet]. [cited 2019 Apr 29]. Available from: https://www.eos.info/systems_solutions/metal/systems_equipment/eos_m_400
22. SLM Solutions Group AG: SLM®800 [Internet]. [cited 2019 Apr 29]. Available from: https://www.slm-solutions.com/products/machines/slmr800/
23. Iso EN, Iso EN, Standard E, Iso EN, European T, En S. SFS-EN ISO 17296-2 : 2016 Additive manufacturing . General principles . Part 2 : Overview of process categories and feedstock (ISO 17296-2 : 2015) Tämä standardi sisältää eurooppalaisen standardin. 2016;
24. Murr LE, Gaytan SM, Ramirez DA, Martinez E, Hernandez J, Amato KN, et al. Metal Fabrication by Additive Manufacturing Using Laser and Electron Beam Melting Technologies. J Mater Sci Technol [Internet]. 2012;28(1):1–14. Available from: http://dx.doi.org/10.1016/S1005-0302(12)60016-4
25. Arcam AB - Additive Manufacturing for Implants and Aerospace, EBM [Internet]. [cited 2019 Apr 29]. Available from: http://www.arcam.com/
26. X7 3D Printer for Continuous Carbon Fiber Filament & Kevlar | Markforged [Internet]. [cited 2019 Feb 28]. Available from: https://markforged.com/x7/
27. About-us | Creatz3D Ceramics 3D Printing [Internet]. [cited 2019 Mar 6]. Available from: https://www.c3d-ceramics.com/ceramic-specifications?gclid=CjwKCAiA_P3jBRAqEiwAZyWWaIEvFfjEO9uDCqUFz1VbnUfOIlW-5Z01Ws0WSxIK777WRqf11A7prBoC2Z8QAvD_BwE
28. Mukherjee T, Zuback JS, Zhang W, DebRoy T. Residual stresses and distortion in additively manufactured compositionally graded and dissimilar joints. Comput Mater Sci [Internet]. 2018;143:325–37. Available from: https://doi.org/10.1016/j.commatsci.2017.11.026
29. Roehling TT, Wu SSQ, Khairallah SA, Roehling JD, Soezeri SS, Crumb MF, et al. Modulating laser intensity profile ellipticity for microstructural control during metal additive manufacturing. Acta Mater [Internet]. 2017;128:197–206. Available from: http://dx.doi.org/10.1016/j.actamat.2017.02.025
30. Robinson JH, Ashton IRT, Jones E, Fox P, Sutcliffe C. The effect of hatch angle rotation on parts manufactured using selective laser melting. Rapid Prototyp J. 2018;
31. Mukherjee T, Zhang W, DebRoy T. An improved prediction of residual stresses and distortion in additive manufacturing. Comput Mater Sci [Internet]. 2017;126:360–72. Available from: http://dx.doi.org/10.1016/j.commatsci.2016.10.003
32. Shiomi M, Osakada K, Nakamura K, Yamashita T, Abe F. Residual stress within metallic model made by selective laser melting process. CIRP Ann - Manuf Technol. 2004;53(1):195–8.
33. Thijs L, Verhaeghe F, Craeghs T, Humbeeck J Van, Kruth JP. A study of the microstructural evolution during selective laser melting of Ti-6Al-4V. Acta Mater [Internet]. 2010;58(9):3303–12. Available from: http://dx.doi.org/10.1016/j.actamat.2010.02.004
34. Acharya R, Sharon JA, Staroselsky A. Prediction of microstructure in laser powder bed fusion process. Acta Mater [Internet]. 2017;124:360–71. Available from: http://dx.doi.org/10.1016/j.actamat.2016.11.018
35. Cheng B, Shrestha S, Chou K. Stress and deformation evaluations of scanning strategy effect in selective laser melting. Addit Manuf [Internet]. 2016;12:240–51. Available from: http://dx.doi.org/10.1016/j.addma.2016.05.007
36. Robinson J, Ashton I, Fox P, Jones E, Sutcliffe C. Determination of the effect of scan strategy on residual stress in laser powder bed fusion additive manufacturing. Addit Manuf. 2018;23(June):13–24.
37. Aboulkhair NT, Everitt NM, Ashcroft I, Tuck C. Reducing porosity in AlSi10Mg parts processed by selective laser melting. Addit Manuf. 2014;1:77–86.
38. Powder Bed Fusion | Additive Manufacturing Research Group | Loughborough University [Internet]. [cited 2019 Mar 7]. Available from: https://www.lboro.ac.uk/research/amrg/about/the7categoriesofadditivemanufacturing/powderbedfusion/

39. Kim H, Lin Y, Tseng TLB. A review on quality control in additive manufacturing. Rapid Prototyp J. 2018;24(3):645–69.
40. Herzog D, Seyda V, Wycisk E, Emmelmann C. Additive manufacturing of metals. Acta Mater [Internet]. 2016;117:371–92. Available from: http://dx.doi.org/10.1016/j.actamat.2016.07.019
41. Khairallah SA, Anderson AT, Rubenchik AM, King WE. Laser powder-bed fusion additive manufacturing: Physics of complex melt flow and formation mechanisms of pores, spatter, and denudation zones. Addit Manuf Handb Prod Dev Def Ind [Internet]. 2017;108:613–28. Available from: http://dx.doi.org/10.1016/j.actamat.2016.02.014
42. Ferrar B, Mullen L, Jones E, Stamp R, Sutcliffe CJ. Gas flow effects on selective laser melting (SLM) manufacturing performance. J Mater Process Technol [Internet]. 2012;212(2):355–64. Available from: http://dx.doi.org/10.1016/j.jmatprotec.2011.09.020
43. Matthews MJ, Guss G, Khairallah SA, Rubenchik AM, Depond PJ, King WE. Denudation of metal powder layers in laser powder-bed fusion processes. Addit Manuf Handb Prod Dev Def Ind [Internet]. 2017;114:677–93. Available from: http://dx.doi.org/10.1016/j.actamat.2016.05.017
44. Van Humbeeck J, Buls S, Thijs L, Kempen K, Vrancken B, Kruth J-P. Selective Laser Melting of Crack-Free High Density M2 High Speed Steel Parts by Baseplate Preheating. J Manuf Sci Eng. 2014;136(6):061026.
45. Frazier WE. Metal additive manufacturing: A review. J Mater Eng Perform. 2014;23(6):1917–28.
46. Porter DA, Easterling KE, Sherif MY. Phase transformations in metals and alloys [Internet]. [cited 2019 Mar 13]. 201–220 p. Available from: https://ebookcentral.proquest.com/lib/tampere/reader.action?docID=1449321
47. Wang YM, Voisin T, McKeown JT, Ye J, Calta NP, Li Z, et al. Additively manufactured hierarchical stainless steels with high strength and ductility. Nat Mater. 2018;17(1):63–70.
48. Lou X, Song M, Wang M, Was GS, Rebak RB. Radiation damage and irradiation-assisted stress corrosion cracking of additively manufactured 316L stainless steels. J Nucl Mater [Internet]. 2018;513:33–44. Available from: https://doi.org/10.1016/j.jnucmat.2018.10.044
49. Montero M, Nardone S, Hautfenne C, Van Humbeeck J. Effect of Heat Treatment of 316L Stainless Steel Produced by Selective Laser Melting (SLM). 27th Annu Int Solid Free Fabr Symp - An Addit Manuf Conf. 2016;558–65.
50. Casati R, Lemke J, Vedani M. Microstructure and Fracture Behavior of 316L Austenitic Stainless Steel Produced by Selective Laser Melting. J Mater Sci Technol [Internet]. 2016;32(8):738–44. Available from: http://dx.doi.org/10.1016/j.jmst.2016.06.016
51. Hong Y, Zhou C, Zheng Y, Zhang L, Zheng J, Chen X, et al. Formation of strain-induced martensite in selective laser melting austenitic stainless steel. Mater Sci Eng A [Internet]. 2019;740–741(June 2018):420–6. Available from: https://doi.org/10.1016/j.msea.2018.10.121
52. Vilaro T, Colin C, Bartout JD. As-fabricated and heat-treated microstructures of the Ti-6Al-4V alloy processed by selective laser melting. Metall Mater Trans A Phys Metall Mater Sci. 2011;42(10):3190–9.
53. Montero Sistiaga ML, Wauthle R, Kruth J-P, Van Humbeeck J, Xie Q, Thijs L. Strong morphological and crystallographic texture and resulting yield strength anisotropy in selective laser melted tantalum. Acta Mater [Internet]. 2013;61(12):4657–68. Available from: http://dx.doi.org/10.1016/j.actamat.2013.04.036
54. Li S, Hassanin H, Attallah MM, Adkins NJE, Essa K. Acta Materialia The development of TiNi-based negative Poisson ' s ratio structure using selective laser melting. Acta Mater [Internet]. 2016;105:75–83. Available from: http://dx.doi.org/10.1016/j.actamat.2015.12.017
55. Spierings AB, Starr TL, Wegener K. Fatigue performance of additive manufactured metallic parts. Rapid Prototyp J. 2013;19(2):88–94.
56. Greitemeier D, Palm F, Syassen F, Melz T. Fatigue performance of additive manufactured TiAl6V4 using electron and laser beam melting. Int J Fatigue [Internet]. 2017;94:211–7. Available from: http://dx.doi.org/10.1016/j.ijfatigue.2016.05.001
57. Everton SK, Hirsch M, Stavroulakis PI, Leach RK, Clare AT. Review of in-situ process monitoring and in-situ metrology for metal additive manufacturing. Mater Des [Internet]. 2016;95:431–45. Available from: http://dx.doi.org/10.1016/j.matdes.2016.01.099

58. P. Bidare, I. Bitharas, R.M. Ward, M.M. Attallah AJM. Fluid and particle dynamics in laser powder bed fusion. PLoS One [Internet]. 2010;5(12):107–20. Available from: https://doi.org/10.1016/j.actamat.2017.09.051
59. Brandl E, Heckenberger U, Holzinger V, Buchbinder D. Additive manufactured AlSi10Mg samples using Selective Laser Melting (SLM): Microstructure, high cycle fatigue, and fracture behavior. Mater Des [Internet]. 2012;34:159–69. Available from: http://dx.doi.org/10.1016/j.matdes.2011.07.067
60. Li C, Liu ZY, Fang XY, Guo YB. Residual Stress in Metal Additive Manufacturing. Procedia CIRP. 2018;71:348–53.
61. Ghasri-Khouzani M, Peng H, Rogge R, Attardo R, Ostiguy P, Neidig J, et al. Experimental measurement of residual stress and distortion in additively manufactured stainless steel components with various dimensions. Mater Sci Eng A [Internet]. 2017;707(July):689–700. Available from: https://doi.org/10.1016/j.msea.2017.09.108
62. Peyre P, Logé RE, Boillat E, Kalentics N, Ćirić-Kostić S, Bogojević N. Tailoring residual stress profile of Selective Laser Melted parts by Laser Shock Peening. Addit Manuf. 2017;16:90–7.
63. Tong Z, Ren X, Jiao J, Zhou W, Ren Y, Ye Y, et al. Laser additive manufacturing of FeCrCoMnNi high-entropy alloy: Effect of heat treatment on microstructure, residual stress and mechanical property. J Alloys Compd [Internet]. 2019;785:1144–59. Available from: https://doi.org/10.1016/j.jallcom.2019.01.213
64. Edwards L. Residual Stresses 2013.
65. Schajer GS. Practical Residual Stress Measurement Methods [Internet]. John Wiley & Sons, Incorporated; 2013 [cited 2019 Feb 27]. Available from: https://ebookcentral.proquest.com/lib/tut/reader.action?docID=1380176
66. Contour Method: Principle [Internet]. [cited 2019 Feb 27]. Available from: https://www.lanl.gov/contour/principle.html
67. Smith CJ, Derguti F, Hernandez Nava E, Thomas M, Tammas-Williams S, Gulizia S, et al. Dimensional accuracy of Electron Beam Melting (EBM) additive manufacture with regard to weight optimized truss structures. J Mater Process Technol [Internet]. 2016;229:128–38. Available from: http://dx.doi.org/10.1016/j.jmatprotec.2015.08.028
68. Dehoff RR, Sames WJ, Tremsin AS, Kirka MM, Babu SS, Bilheux H, et al. Site specific control of crystallographic grain orientation through electron beam additive manufacturing. Mater Sci Technol. 2014;31(8):931–8.
69. Thijs L, Kempen K, Kruth JP, Van Humbeeck J. Fine-structured aluminium products with controllable texture by selective laser melting of pre-alloyed AlSi10Mg powder. Acta Mater [Internet]. 2013;61(5):1809–19. Available from: http://dx.doi.org/10.1016/j.actamat.2012.11.052
70. Niendorf T, Leuders S, Riemer A, Richard HA, Tröster T, Schwarze D. Highly anisotropic steel processed by selective laser melting. Metall Mater Trans B Process Metall Mater Process Sci. 2013;44(4):794–6.
71. Liu X, Xiang S, Li Q, Wu J, Yao K-F, Tian Y, et al. Microstructures and mechanical properties of CrMnFeCoNi high entropy alloys fabricated using laser metal deposition technique. J Alloys Compd [Internet]. 2018;773:387–92. Available from: https://doi.org/10.1016/j.jallcom.2018.09.235
72. Parimi LL, Ravi G, Clark D, Attallah MM. Microstructural and texture development in direct laser fabricated IN718. Mater Charact [Internet]. 2014;89:102–11. Available from: http://dx.doi.org/10.1016/j.matchar.2013.12.012
73. Tammas-Williams S, Todd I. Design for additive manufacturing with site-specific properties in metals and alloys. Scr Mater [Internet]. 2017;135:105–10. Available from: http://dx.doi.org/10.1016/j.scriptamat.2016.10.030
74. Reichardt A, Dillon RP, Borgonia JP, Shapiro AA, McEnerney BW, Momose T, et al. Development and characterization of Ti-6Al-4V to 304L stainless steel gradient components fabricated with laser deposition additive manufacturing. Mater Des [Internet]. 2016;104:404–13. Available from: http://dx.doi.org/10.1016/j.matdes.2016.05.016
75. Shishkovsky I, Kakovkina N, Scherbakov V. Fabrication of heat-resisting nickel composite gradient structures with TiC nano additive during powder bed fusion process. Procedia CIRP [Internet]. 2018;74:68–71. Available from: https://doi.org/10.1016/j.procir.2018.08.032
76. Mumtaz KA, Hopkinson N. Laser melting functionally graded composition of

Waspaloy®and Zirconia powders. J Mater Sci. 2007;42(18):7647–56.
77. Anstaett C, Seidel C, Reinhart G. Fabrication of 3D Multi-material Parts Using Laser-based Powder Bed Fusion. Solid Free Fabr Symp. 2017;1548–56.
78. Sprowls DO. Evaluation of Stress-Corrosion Cracking. 2019;
79. Vargas-Gonzalez L, Speyer RF, Campbell J. Flexural strength, fracture toughness, and hardness of silicon carbide and boron carbide armor ceramics. Int J Appl Ceram Technol. 2010;7(5):643–51.
80. Ćurković L, Rede V, Grilec K. Utjecaj opterećenja na izmjerenu tvrdoću silicijeve karbidne keramike. Kem u Ind Chem Chem Eng. 2010;59(10):483–8.
81. Type A. Supra 316L/4432. :1–8.
82. Hamzeh M, Karkehabadi MM, Jalali R. Failure analysis of stress corrosion cracking of 316L structured packing in a distillation tower. Eng Fail Anal [Internet]. 2017;79(May):431–40. Available from: http://dx.doi.org/10.1016/j.engfailanal.2017.05.019
83. Spencer K, Véron M, Yu-Zhang K, Embury JD. The strain induced martensite transformation in austenitic stainless ... 2009;
84. Zhang SY, Compagnon E, Godin B, Korsunsky AM. Investigation of Martensite Transformation in 316L Stainless Steel. Mater Today Proc [Internet]. 2015;2:S251–60. Available from: http://dx.doi.org/10.1016/j.matpr.2015.05.035
85. Ricker RE, Lee EU, Taylor R, Lei C, Pregger B, Lipnickas E. Chloride ion activity and susceptibility of Al alloys 7075-T6 and 5083-H131 to stress corrosion cracking. Metall Mater Trans A Phys Metall Mater Sci. 2013;44(3):1353–64.
86. Licciardello F, Rizzo V, Coriolani C, Volo M, Muratore G. Measures to prevent stress corrosion cracking of aluminum cans for carbonated beverages. Ital J Food Sci. 2018;30(5):142–5.
87. Congleton J. Stress-corrosion Cracking of Stainless Steels. Corros Third Ed. 2013;1:8:52-8:83.
88. Sjong A, Eiselstein L. Marine atmospheric SCC of unsensitized stainless steel rock climbing protection. J Fail Anal Prev. 2008;8(5):410–8.
89. Prosek T, Iversen A, Taxén C, Thierry D. Low-Temperature Stress Corrosion Cracking of Stainless Steels in the ... Corros Sci Sect. 2009;65(2):105–17.
90. ASTM C1161. Standard Test Method for Flexural Strength of Advanced Ceramics at Ambient Temperature. ASTM Int. 2013;1–19.
91. Fitzpatrick ME, Fry AT, Holdway P, Kandil FA, Shackleton J, Suominen L. Determination of Residual Stresses by X-ray Diffraction – Issue 2.
92. Cullity BD, Stock SR. Elements of X-ray diffraction [Internet]. 3rd ed. Upper Saddle River (NJ): Prentice Hall; 2001. Available from: http://tut.summon.serialssolutions.com/2.0.0/link/0/eLvHCXMwY2AwNtIz0EUrE0DHEBoam6SkmKSmJZqDus4W5saJqaaWaYaJFuaJoCHe8Cgj3whTLy-LSOjZ0aCtMSWIJXppmXl5iUAStvcAKAYalDMEzygxM7ACK20LUxYGVkcvP3fwpnMjUDPGAHylE_iAHRgftAWlBLabD1x_uAkysID2FAgxMKXmiTDIukKWbBcr5KcpROg
93. Bouras M, Boumaiza A, Ji V, Rouag N. XRD peak broadening characterization of deformed microstructures and heterogeneous behavior of carbon steel. Theor Appl Fract Mech [Internet]. 2012 Oct;61:51–6. Available from: http://www.sciencedirect.com/science/article/pii/S0167844212000675
94. Tialv F. Materialdatenblatt Material data sheet CL 20ES Edelstahl. 49(0):96215.
95. Elsariti SM, Haftirman. Behaviour of stress corrosion cracking of austenitic stainless steels in sodium chloride solutions. Procedia Eng [Internet]. 2013;53:650–4. Available from: http://dx.doi.org/10.1016/j.proeng.2013.02.084
96. Mayuzumi M, Tani J, Arai T. Chloride induced stress corrosion cracking of candidate canister materials for dry storage of spent fuel. 2008;238:1227–32.
97. Gross D, Thomas Seelig. Fracture Mechanics With an Introduction to Micromechanics [Internet]. Springer. 2011. 336 p. Available from: http://doi.wiley.com/10.1002/9781118097298.weoc096
98. Courtney TH. Mechanical behavior of materials [Internet]. 2nd ed. McGraw Hill; 2000 [cited 2019 Aug 23]. 733 p. Available from: https://tuni.finna.fi/Record/tutcat.145718
99. Christian JW, Mahajan S. Deformation twinning. Prog Mater Sci. 1995;39(1–2):1–157.